L-Università
ta' Malta

Investigation of the Effect of Different Functional MRI Sequences on Local Homogeneity Measures: Implications for Neuroimaging Studies.

Kristian Galea

Supervised by Claude Julien Bajada

Co-Supervised by Nolan Vella

A dissertation presented as part-fulfilment of the requirements for the award of the Masters in Medical Physics of the Faculty of Health Sciences of the University of Malta September 2024

Department of Medical Physics
University of Malta
September 2024

L-Università ta' Malta

FACULTY/INSTITUTE/CENTRE/SCHOOL Faculty of Health Sciences

DECLARATIONS BY POSTGRADUATE STUDENTS

(a) Authenticity of Dissertation

I hereby declare that I am the legitimate author of this Dissertation and that it is my original work.

No portion of this work has been submitted in support of an application for another degree or qualification of this or any other university or institution of higher education.

I hold the University of Malta harmless against any third party claims with regard to copyright violation, breach of confidentiality, defamation and any other third party right infringement.

(b) Research Code of Practice and Ethics Review Procedures

I declare that I have abided by the University's Research Ethics Review Procedures. Research Ethics & Data Protection form code FHS-2023-00578.

As a Master's student, as per Regulation 77 of the General Regulations for University Postgraduate Awards 2021, I accept that should my dissertation be awarded a Grade A, it will be made publicly available on the University of Malta Institutional Repository.

02.2023

Acknowledgements

First and foremost, I would like to express my gratitude to my supervisor Dr. Claude Julien Bajada and co-supervisor Mr. Nolan Vella for their invaluable support throughout the study. In addition to this, I would like to thank all the volunteers who participated during the study. Without their participation, this study would not have been possible. Furthermore, I would like to express my heartfelt appreciation to fellow colleagues at the Boundaries of the Brain (BOB) laboratory of the University of Malta who have contributed indirectly or directly to the study. Finally, I would like to thank the University of Malta's MRI Platform (UMRI) for access to scanning equipment and services, use of its infrastructure, and resources such as documentation and preprocessing scripts.

Abstract

Background: Data analysis in functional magnetic resonance imaging (fMRI) is typically performed using model-based methods such as the general linear model, whose detection power is limited by the models' complexity. The field of fMRI has started adopting data-driven approaches. This includes the Vogt-Bailey index, which has not been tested across pulse sequences.

Objectives: The study aimed to assess functional activation in fMRI across pulse sequences using the Vogt-Bailey index, and benchmark the results against the general linear model.

Methodology: A cohort of 10 research volunteers were scanned in a 3T magnetic resonance imaging (MRI) scanner using 3 separate pulse sequences employing voxels of volumes 1.8^3mm^3, 2^3mm^3, and 2.5^3mm^3 respectively while performing a block-design finger tapping experiment. The data was analysed with the Vogt-Bailey index and the general linear model. The brain activation maps obtained for each sequence were compared using the Dice-Sørensen coefficient, and the results from the two techniques were compared using the Overlap coefficient.

Results: Applying the Vogt-Bailey index on spatially smoothened data enhanced conformance to the general linear model, with moderately-high Overlap coefficients (0.4 to 0.7). Applying the Vogt-Bailey index on unsmoothened data produced more specific results, exhibiting less conformance to the general linear model, with low-moderate Overlap coefficients (0.2 to 0.3). The functional activation detected by the general linear model was only a subset of that detected with the Vogt-Bailey index. Overall, the results of the general linear model were more reproducible across sequences with moderately-high Dice coefficients (0.6 to 0.7).

Conclusions and Recommendations: Spatial smoothing of the 2.5^3mm^3 data may be applied prior to the Vogt-Bailey analysis for higher conformance to the general linear model. Alternatively, for somatotopic evaluations, the Vogt-Bailey analysis may be applied on unsmoothened higher resolution data. The results require further validation across a larger cohort of subjects.

***Keywords*—** Medical Imaging, Functional MRI, pulse sequences, Data Analysis, Vogt-Bailey index, general linear model

Table of Contents

List of Figures

List of Tables

List of Definitions

Blood oxygenation level dependent effect Blood Oxygenation Level Dependent (BOLD) effect is the most frequently used process for detecting neuronal activity in fMRI. The BOLD effect is defined as the neurophysiological process caused by an increase in neural activity, and consists of a number of sub-processes. The BOLD effect is initiated via a stimulus which induces an increase in neuronal activity in a related brain area. This causes an increase in the blood flow to the related brain area (haemodynamic response), increasing the local level of oxyhaemoglobin relative to the level of deoxyhaemoglobin. The increase in oxyhaemoglobin which is diamagnetic causes a local incremental increase in $T2^*$ signal (EMITEL Consortium, 2016a). 9

Echo Planar Imaging EPI is a class of pulse sequences that allows the acquisition of all phase encoding lines needed to construct the volumetric image within a single repetition time period. The fast image acquisition characteristics of EPI has made it widely adopted in fMRI (EMITEL Consortium, 2016b). 10

fMRI Functional magnetic resonance imaging (fMRI), is a medical imaging modality used to study the brain function (EMITEL Consortium, 2016c). iv

HRF The haemodynamic response function (HRF) represents the ideal noiseless response of an activated voxel's time-series signal to an infinitesimally brief stimulus (Poldrack et al., 2011). 1

Local Homogeneity Local Homogeneity measures such as the Vogt-Bailey index assume that the haemodynamic characteristics of voxels within a neuronally active brain region are synchronous to each other. Elevated local homogeneity metrics such as an elevated Vogt-Bailey index reflect synchronous neural activity in the local brain region, and thus local functional activation (Wu et al., 2009; Xu et al., 2019). 8

List of Acronyms

BOLD	Blood Oxygen Level-dependent
BIDS	Brain imaging data structure
CNR	Contrast-to-noise ratio
DCT	Discrete Cosine Transform
DICOM	Digital Imaging and Communications in Medicine
EPI	Echo Planar Imaging
FBIRN	Function Biomedical Informatics Research Network
FDR	False Discovery Rate
FSL	Oxford Centre for Functional MRI of the Brain Software Library
FMRIB	Oxford Centre for Functional MRI of the Brain
fMRI	Functional Magnetic Resonance Imaging
FOV	Field of View
FWHM	Full width at half maximum
GLM	General Linear Model
GRAPPA	Generalised Autocalibrating Partially Parallel Acquisitions
HCP	Human Connectome Project
HRF	Haemodynamic Response Function
INU	Intensity non-uniformity
MB	Multi-band factor
MNI	Montreal Neurological Institute
MRI	Magnetic Resonance Imaging
NifTi	Neuroimaging Informatics Technology Initiative
NNL	Nordic Neuro Lab

PCA	Principal Component Analysis
PVE	Partial Volume Effect
RF	Radio frequency
SAR	Specific-absorption rate
SENSE	Sensitivity Encoding
SMS	Simultaneous Multi Slice
SNR	Signal-to-noise ratio
TSNR	Temporal Signal-to-noise ratio
TE	Time of Echo
TR	Time of Repetition
UMRI	The University of Malta Magnetic Resonance Imaging Platform
VB Index	Vogt-Bailey Index

1 Introduction to the study

1.1 Introduction

This chapter presents the problem statement, background and context, objectives, scope, summary of research methodology, ethical considerations and relevance of the study.

1.2 Problem statement

Traditionally, fMRI studies utilised a model-based approach for analysing neuronal activation (hereafter functional activation) in the cortex (Stroman, 2016, p. 195). Recently, the field of fMRI has made strides towards more data-driven methodologies. This includes the Vogt-Bailey (VB) index, a locally developed data-driven method. However, the VB index has not yet been rigorously tested across different pulse sequences, particularly across different voxel volumes. Furthermore, the fMRI sequences currently in use have poor spatial resolution using larger voxel volumes to maintain adequate signal-to-noise ratio (SNR) (Triantafyllou et al., 2005). Larger voxels lead to increased susceptibility to the partial volume effect (PVE) limiting the accuracy by which functional activation may be localised (Hu & Glover, 2009). Therefore, rigorous examination of functional activation analysis with the VB index for various voxel volumes is required, which could lead to the optimisation of the pulse sequences used.

1.3 Background and context

1.3.1 Data analysis in Functional MRI

Methodological approaches to the study of functional activation in fMRI are categorised as either model-based or data-driven. Model-based methods are constructed upon a priori model, where the time course signal of each voxel is statistically compared with a user-specified model (Stroman, 2016, p. 195). The general linear model (GLM) is one notable example of model-based methods, and often utilises the convolution of the experiment's stimulus function with the hemodynamic response function (HRF) as a priori model (Zang et al., 2004). However, model-based methods are limited by the fact that the HRF varies across brain regions and individuals (Miezin et al., 2000) due to differences in neural activity, heart rate, respiration, and baseline cerebral blood flow across different participants (Handwerker et al., 2004). Alternatively, data-driven methods allow data to be the primary driver of results (Calhoun, 2018). One such method, the VB index, makes use of a searchlight approach by calculating the local correlation of each voxel's temporal signal relative to its neighbours. Then, using spectral graph theory, it defines the voxels in the searchlight as individual vertices connected together with edges weighted according to their pairwise correlations (Bajada et al., 2020). Finally, the algorithm calculates the normalised algebraic connectivity (VB index) of the graph, whose magnitude determines the strength of the graph's connections. In other words, large VB indices point to correlated voxels and thus local functional activation (Farrugia et al., 2022; Farrugia et al., 2024).

1.3.2 Functional MRI sequences

The accurate interpretation of any methodological approach following an fMRI study depends amongst other factors on the optimisation of the pulse sequence which contains the timings and duration of the Radio frequency (RF) and gradient pulses necessary for generating and localising the MR signal (McRobbie et al., 2006, p. 31). The specific scanning parameters of the sequence depend on the specific application of the fMRI study. In any case, the scanning parameters should be tweaked such that the time series of images provided have adequate spatial resolution, contrast-to-noise ratio (CNR) and SNR (Molloy et al., 2014). Ideally, the images are produced within a reasonable time-frame to ensure patient comfort and to reduce motion related artefacts. However, the image quality parameters might not always be positively related. Hence, despite being optimal to reduce the PVE, a high spatial resolution could lead to an unsuitable reduction in the SNR. Therefore, the optimal fMRI sequence achieves a balance between image quality parameters and also acquisition time (Stroman, 2016, p. 130).

1.4 Objectives of the study

The aim of the study was to assess functional activation in fMRI using different gradient-echo echo-planar imaging (EPI) sequences with differing voxel volumes. The study was motivated by the fact that the VB index has not yet been rigorously tested across different pulse sequences. The aim of the study was achieved through the following objectives:

1. Develop three different pulse sequences with differing voxel volumes.
2. Test the sequences on a cohort of 10 research volunteers.
3. Compare image quality at each sequence.

4. Analyse the data using the VB index, and a traditional model-based approach; the GLM.
5. Compare the results of each sequence qualitatively and quantitatively together.
6. Compare the results obtained with the VB index and the GLM qualitatively and quantitatively together and with literature.

1.5 Scope of the study

The study was limited to a small cohort of 10 research volunteers. As a consequence of time limitations, larger cohorts were not possible. The MRI data was gathered using the MRI scanner provided by the University of Malta Magnetic Resonance Imaging (UMRI) platform.

1.6 Research methodology

The first portion of the study involved the development of three different gradient echo EPI pulse sequences with different voxel volumes to assess functional activation at increasing spatial resolution. Then, a total of research 10 volunteers were recruited and scanned in three separate fMRI acquisitions using the pulse sequences. During the scanning, the participants were subjected to a block design finger-tapping experiment. The data was first preprocessed and then analysed using the GLM and the VB index. The results obtained were compared qualitatively and quantitatively together across pulse sequences and data analysis techniques. Quantitative comparison of image quality parameters such as the SNR across the different sequences was also conducted.

1.7 Ethical considerations

The study made use of primary fMRI data acquired from 10 adult volunteers. The volunteers provided informed consent prior to being scanned. The gathered data was pseudo-anonymised and personal information such as names or identification numbers were not available to the researcher. Only the principal supervisor could link the volunteer’s study code to their personal information, crucial in the event of an abnormality. The study was approved by the University Research Ethics Committee of the University of Malta.

1.8 Relevance of the study

The relevance of the study for the various stakeholders is as follows:

1. For the medical physics profession; The study aims to assess the VB index across pulse sequences which could help in designing more robust fMRI studies, further develop the VB index, and optimise local fMRI sequences. Ultimately, this could lead to the improvement in the quality of an fMRI study. This work can also be of interest to those developing new data-driven approaches for the analysis of fMRI data.
2. For patients, the study could enhance the accuracy by which functional activation in the brain is determined and hence enhance the understanding of neurological and psychiatric conditions.

1.9 Conclusion

This chapter introduced the study. The next chapter provides a review of the literature. Chapter three describes the research methodology used throughout the study, while chapter four presents the results. Chapter five discusses the results obtained, and chapter six summarises the most important conclusions of the study, proposes recommendations arising from the study, and provides suggestions for future research.

2 Literature review

2.1 Introduction

The study aimed to investigate functional activation analysis with the VB index across pulse sequences, focusing primarily on the spatial resolution. Hence, this chapter presents the theoretical foundations of the VB index, discusses typical fMRI sequences, and the scanning parameters that need to be modified to permit modification of the spatial resolution while maintaining adequate SNR and CNR. Furthermore, a critical and comprehensive review of the literature will also be performed to investigate the typical scanning parameters employed in fMRI sequences. To conduct the review, several electronic research databases were used including Google Scholar, IOPscience, Scopus, and IEEE Xplore. The databases were last consulted on 01/06/2024 and the review included articles published between 1960 and 2024. The keywords used varied throughout the review, but when possible, the PICO framework was followed. As an example, some keywords used in the literature review included: “fMRI, Vogt-Bailey Index, pulse sequences, spatial resolution, SNR”. Articles were included in the review if they were written in English, and made use of BOLD fMRI. Conversely, articles were excluded if they contained inadequate methodology or had insufficient results. Articles were analysed according to 1) title, and year of publication, 2) research methodology, and MRI system used, 3) number of participants or the type of phantoms tested, 4) results, 5) strengths and limitations of the study.

2.2 The Vogt-Bailey Index

The determination of functional activation in fMRI is preceded by an appropriate data analysis method, which as mentioned in the introduction could be either model-based or data-driven. The study aims to assess a locally developed data-driven algorithm, the VB index (Bajada et al., 2020; Farrugia et al., 2022; Farrugia et al., 2024) across pulse sequences, particularly across voxel volumes. The VB algorithm, which makes use of spectral graph theory, iteratively goes over each voxel, considers the voxels’ neighbours, and represents the local neighbourhood of voxels as vertices on a feature similarity graph. Edges join the vertices (voxels) together, and the weighting assigned to each edge represents the similarity between the fMRI time series signal of a pair of vertices. Figure 1 illustrates an example of a graph which contains 9 vertices, each representing a voxel. In this illustration, the vertices are connected by edges, and the thickness assigned to each edge reflects the pairwise similarity between the time-series signal of the vertices (voxels) connected by the edge.

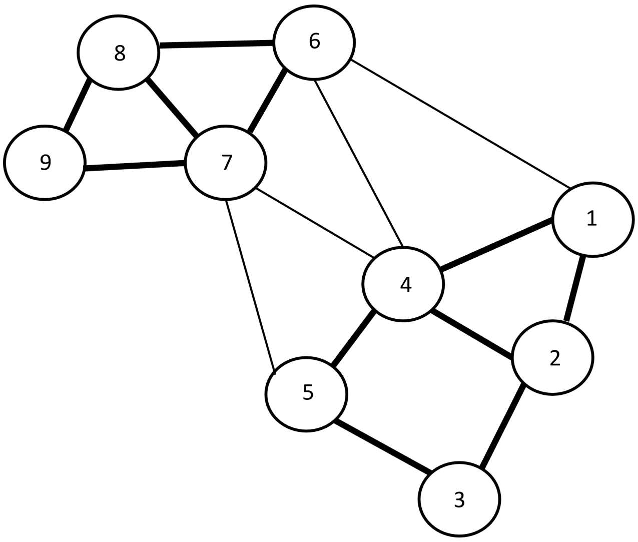

Figure 1. An illustration of a graph containing 9 vertices. Every vertex represents an individual voxel, and the edges connecting the vertices represent the pairwise similarity between the fMRI time series of each pair of voxels. In this simple illustration, thicker edges translate to more similarity (higher weighting). All disconnected vertices are considered to be connected with a weight of zero.

The pairwise similarities (hence the weights of the edges) of the fMRI time series signal of each voxel are computed using the Pearson correlation coefficient, and are represented via a similarity matrix (**A**). Each element of the similarity matrix contains the weight (w_{ij}) of the edge connecting a vertex *i* with another *j*. Considering the example illustrated in figure 1, the similarity matrix could be represented as in (2.1) (Bajada et al., 2020).

$$\mathbf{A} = \begin{pmatrix} 0 & w_{12} & w_{13} & \dots & w_{19} \\ w_{21} & 0 & w_{23} & \dots & w_{29} \\ w_{31} & w_{32} & 0 & \dots & w_{39} \\ \vdots & \vdots & \vdots & \ddots & \vdots \\ w_{91} & w_{92} & w_{93} & \dots & 0 \end{pmatrix} \tag{2.1}$$

Additional information of the graph is provided by the degree matrix (**D**), a diagonal matrix with each element d_{ij} denoting the sum of the weights of the edges connecting to vertex *i* (von Luxburg, 2007). Again, using the aforementioned example in figure 5, the degree matrix could be represented as in (2.2).

$$\mathbf{D} = \begin{pmatrix} \sum_{j=1}^{9} w_{1j} & 0 & 0 & \dots & 0 \\ 0 & \sum_{j=1}^{9} w_{2j} & 0 & \dots & 0 \\ 0 & 0 & \sum_{j=1}^{9} w_{3j} & \dots & 0 \\ \vdots & \vdots & \vdots & \ddots & \vdots \\ 0 & 0 & 0 & \dots & \sum_{j=1}^{9} w_{9j} \end{pmatrix} \tag{2.2}$$

Finally, both the similarity and degree matrices are combined to form the Laplacian matrix ($\mathbf{L} = \mathbf{D} - \mathbf{A}$) which provides a complete description of the graph. After formulating the graph of a local neighbourhood of voxels, the VB algorithm partitions the graph into a number of disjoint clusters ($B, C, ...$) such that vertices which exhibit strong similarity (correlated time-series signals) are grouped together, but separated from those with which they exhibit weak similarity. The VB algorithm partitions the graph in a way that minimises the total weight that is "cut" during the partition, thereby removing the weakest edges. Mathematically, the VB algorithm achieves this by minimising the Ratio cut function, which for a two cluster partition is given by equation (2.3) (Farrugia et al., 2022).

$$Ratiocut(B, C) = \left(\frac{1}{n_B} + \frac{1}{n_C}\right) \sum_{\substack{i \in B \\ j \in C}} w_{ij} \tag{2.3}$$

Where n_B and n_C denote the number of vertices in clusters B and, C respectively, w_{ij} are the weights of the edges connecting vertices v_i in subset B with vertices v_j in subset C. Pictorially, using the previous example in figure 1, one could partition the graph as in figure 2 which minimises the total weight of the edges cut by removing the weakest edges (in this example thinnest edges). As seen in figure 2, this separates the graph into two disjoint clusters, with each cluster having strongly "bound" vertices. The minimum value of the ratio cut function in equation (2.3) has previously been proven by Farrugia et al. (2022) to be the second eigenvalue of the Laplacian matrix **L**, defined previously. In other words:

$$Min(Ratiocut) \approx \lambda_2 \tag{2.4}$$

Previously, Fiedler (1973) termed λ_2 the algebraic connectivity, since larger λ_2 denote that the graph is more strongly connected and hence harder to partition. In the VB algorithm, λ_2, normalised between 0 and 1, is termed as the VB index. The VB algorithm computes the VB indices for each voxel across

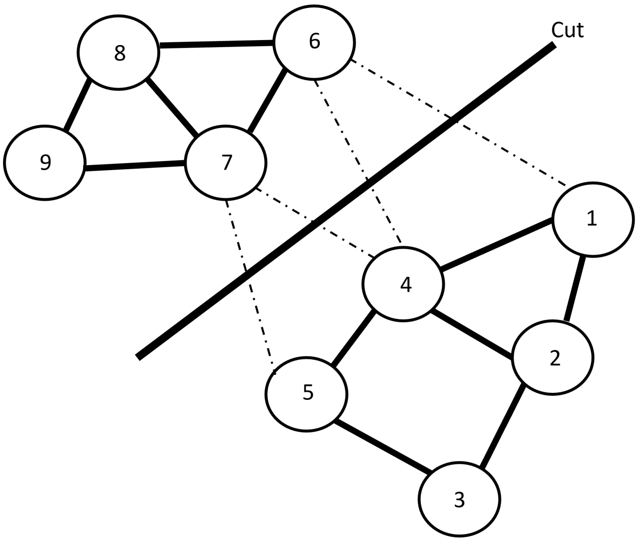

Figure 2. Using the previous example in figure 1, partitioning the graph in two subsets involves minimising the amount of weight that is cut.

the cortex using a searchlight approach. The VB algorithm considers a voxel at the centre of the searchlight (kernel), and takes into account the neighbouring voxels. The algorithm formulates the graph of the neighbourhood by calculating the Laplacian, and determines the VB index of the Laplacian, which is assigned to the voxel at the centre of the kernel. The VB algorithm then slides the kernel to the adjacent voxel and repeats this process. This procedure is performed iteratively for each voxel in the fMRI data, as highlighted in figure 3. In the context of functional activation analysis, a smaller VB index points to weakly connected graphs, indicating that the time series signal of the local neighbourhood of voxels is weakly correlated. Thus, low VB indices indicate non-synchronous changes in the fMRI signal of the local neighbourhood of voxels. Conversely, higher VB indices correspond to local correlations in the time-series signal of the neighbourhood voxels, which is synonymous to Local Homogeneity or local functional connectivity. Local homogeneity measures in fMRI such as the VB index assume that a neuronally active brain region is characterised by elevated local homogeneity (high VB index), which reflects synchronous neural activity in the local brain region (Wu et al., 2009; Xu et al., 2019). Furthermore, the VB algorithm has also been termed as an edge-detection technique, since it looks for sharp changes (boundaries) in the local functional organisation of the cortex (Farrugia et al., 2022).

2.3 Motivation of research

The VB index has not yet been tested rigorously across various pulse sequence. The study aims to analyse functional activation with the VB index across pulse sequences with differing voxel volumes, which could lead to the optimisation of the pulse sequences currently employed. Therefore, the remainder of the review will focus on discussing the typical pulse sequences employed in fMRI, and user-selectable parameters which may be modified to permit changes in voxel volumes while maintaining adequate SNR and CNR.

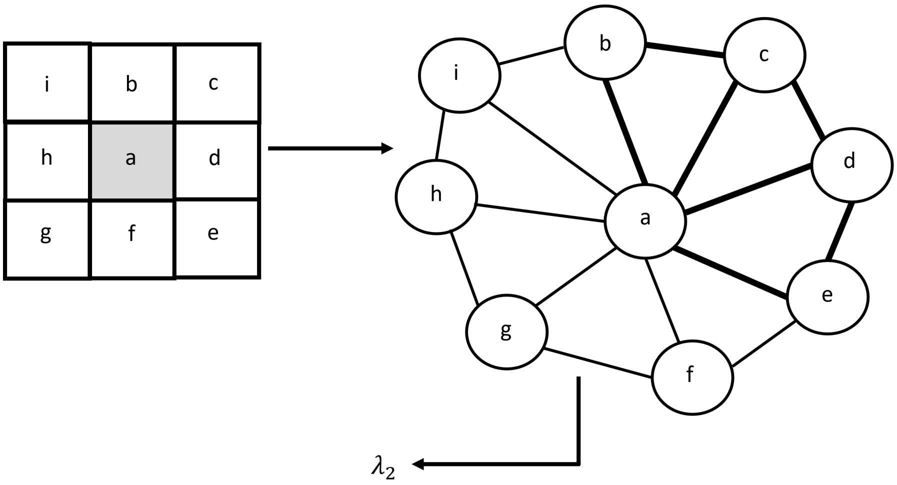

Figure 3. A simplified 2D workflow of the VB index. Considering the nearest neighbours of the voxel at the centre of the searchlight, the affinity, degree, and Laplacian matrices are computed. This is followed by the VB index of the Laplacian. The kernel then moves on to the next voxel, putting for example voxel *b* at the centre of the searchlight and so on.

2.4 Functional MRI pulse sequences

Neuronal activation is paired with an increase in oxygenated blood supply to the activated region, resulting in a local reduction of deoxygenated blood. Blood oxygenation level dependent effect (BOLD) fMRI indirectly measures neuronal activity by capitalising on local differences in the volumes of oxygenated and deoxygenated blood and the differences in magnetic susceptibility between oxygenated blood which is diamagnetic, and deoxygenated blood which is slightly paramagnetic (Holdsworth & Bammer, 2008). The net result is a local increase in the MR signal in regions with increased neural activity (BOLD effect) which is modelled by the HRF illustrated in figure 4, and may be mapped using T_2^* weighted MRI (Buxton, 2009, p. 7).

There are two principal pulse sequences utilised in MRI: the spin-echo and gradient-echo sequences (Stroman, 2016). Although spin-echo sequences potentially offer higher-quality images, they are significantly less sensitive to the BOLD effect when compared to gradient-echo sequences, since gradient-echo sequences have the capability of producing T_2^* weighted images (Norris, 2012). Therefore, most fMRI studies are conducted with gradient-echo sequences (Holdsworth & Bammer, 2008). In addition

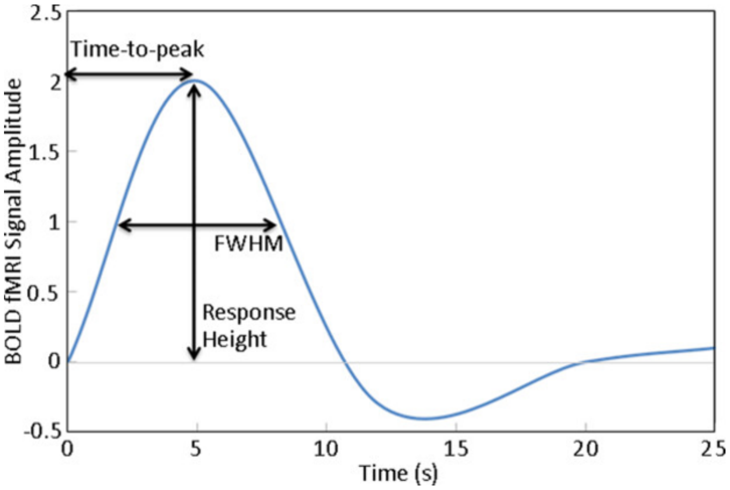

Figure 4. The canonical Haemodynamic Response Function, which relates neural activity and the corresponding change in the fMRI signal in the activated region. Adopted from: Rangaprakash et al. (2018) licensed under CC BY 4.0.

to this, to speed up image acquisition, most fMRI studies utilise fast imaging techniques such as Echo Planar Imaging (EPI) in conjunction with gradient-echo sequences (Volz et al., 2019).

2.4.1 Gradient-echo EPI

A chronogram containing the timings of the RF pulses and gradient fields in a typical gradient-echo EPI sequence is illustrated in figure 5. As with conventional gradient-echo sequences, EPI sequences commence through the simultaneous application of a slice selective RF pulse with a frequency bandwidth, and a magnetic field gradient along the z-axis (G_z). Through the phenomenon of nuclear magnetic resonance, the magnetic moments of hydrogen nuclei within the slice are perturbed by some flip angle α away from the static field B_0 (Poustchi-Amin et al., 2001) and precess in phase, resulting in a precessing transverse magnetisation vector as illustrated in figure 6 (McRobbie et al., 2006, p. 143). However, as a consequence of T_2^* relaxation, the precession of the hydrogen nuclei dephase with time (Gossuin et al., 2010).

After slice-selective excitation, phase (G_y) and frequency (G_x) encoding gradient fields applied along the y-axis and x-axis respectively, localise the signal on the slice. The phase encoding gradient, turned on briefly prior to sampling the MR signal, induces a spatially dependant phase change to the precession of the hydrogen nuclei (Currie et al., 2013). The frequency encoding gradient, applied during data collection, consists of a negative lobe which accelerates dephasing of the transverse magnetisation, and a positive lobe which reverses dephasing. This brings the nuclei's precession back into phase, forming a gradient echo, which constitutes the MR signal and is measured by a receiver coil (Jenkinson, M, 2018). As a consequence of G_x, the Larmor frequency of hydrogen nuclei is also spatially dependent along the x-axis. Consequently, signal localisation on the slice is achieved through the analysis of the echo's phase and frequency (Plewes & Kucharczyk, 2012).

In conventional gradient-echo sequences, a single pulse sequence acquires data from one slice and from a single phase-encoding step. Thus, the pulse sequence is repeated several times for each slice. However, EPI techniques employ a series of bipolar frequency-encoding gradients, forming a train of gradient echoes as seen in figure 5. Using an accompanying phase-encoding gradient, each gradient-echo is phase-encoded onto a subsequent phase encoding line (Poustchi-Amin et al., 2001). The time elapsed from the application of the RF pulse to the point at which the central k-space line is sampled is referred to as the time of echo (TE) (Bernstein et al., 2004). The main advantage of EPI is the ability to capture all the phase encoding steps of a slice in a single sequence (single-shot EPI) (Jenkinson, M, 2018). However, compared to conventional sequences, EPI sequences typically have poor spatial resolution (Jezzard & Clare, 1999; Volz et al., 2019).

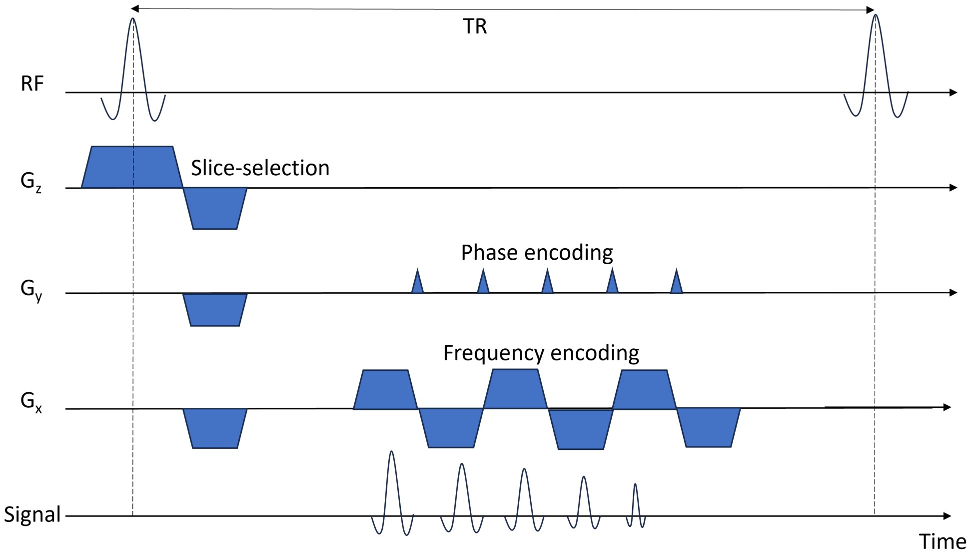

Figure 5. The gradient-echo EPI imaging sequence. Adapted from (McRobbie et al., 2006)

2.5 Scanning parameters of an fMRI pulse sequence

Pulse sequences are composed of several scanning parameters which may be altered prior to an MRI study. The values of the scanning parameters have an effect on the SNR, CNR and spatial resolution of the resulting time-series of images (Buxton, 2009, p. 78). Table 1 provides the median and range of values of some major scanning parameters of a typical gradient-echo EPI sequence acquired from a

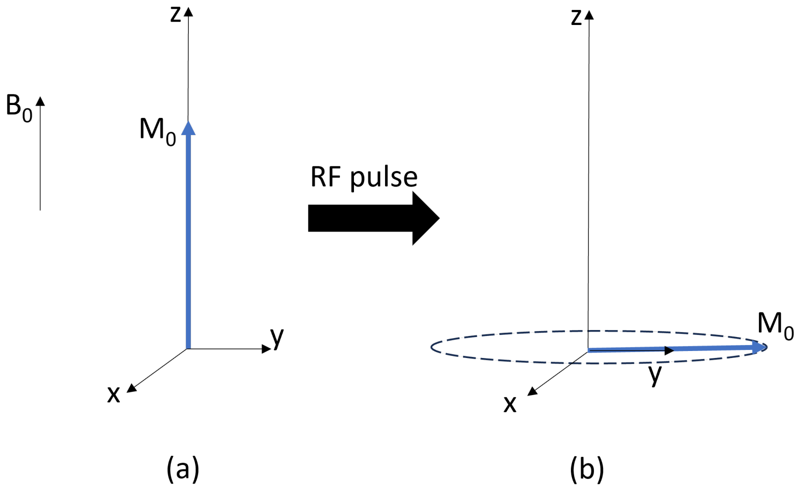

Figure 6. The net magnetisation is initially aligned along the main magnet's magnetic field (B_0) i.e., the z-axis (a). The RF pulse excites and flips the net magnetisation of the hydrogen nuclei by some angle α away from the z-axis (b). In this case α=90°

review of eight different fMRI studies (Dong et al., 2014; Liu et al., 2010; Rastegarnia et al., 2023; Shukla et al., 2010; Tian et al., 2012; Uğurbil et al., 2013; R. Yuan et al., 2013; Zang et al., 2004). The study aims to assess the VB index with pulse sequences having increasingly higher spatial resolution. Therefore, the next portion of the review discusses the individual scanning parameters which need to be altered to modify spatial resolution while maintaining adequate SNR and CNR.

2.6 Signal-to-noise ratio

One of the major issues associated with the use of smaller voxels is the associated reduction in the SNR, which varies linearly with the voxel volume (Triantafyllou et al., 2005). This may be one of the reasons as to why most fMRI studies identified in table 1 used large voxels (3 $\times$ 3 $\times$ 3 mm^3). The study intends to assess functional activation analysis with the VB index across voxels of volumes that are typical in fMRI studies, but also volumes that may be considered smaller than typical. Thus, to permit reductions in the voxel volume, optimising SNR mediating parameters including the repetition time (TR), flip angle and the readout bandwidth is required.

2.6.1 Repetition time

In fMRI, several volumes are sequentially collected over time to sample the time-varying BOLD signal in activated brain regions. Thus, each slice in the volume is re-excited after some repetition time (TR)

(Huettel et al., 2014). Most of the literature presented in table 1 used longer TR values ($\geq$ 2000 ms) for two main reasons. Firstly, longer TR values allow for greater recovery of the longitudinal magnetisation (T_1) that occurs between RF pulses, thereby maximising the SNR (Constable & Spencer, 2001). In addition to this, longer TR values permit the collection of more slices resulting in better brain coverage, and a higher spatial resolution (L. Chen et al., 2015). However, one of the issues with longer TR values is the reduction in the temporal resolution. The advent of acceleration techniques such as simultaneous multi slice (SMS) excitation, have made TR reductions without sacrificing brain coverage and spatial resolution a possibility (Uğurbil et al., 2013). The major advantage associated with the use of a shorter TR is the improvement in the temporal resolution due to a higher sampling rate, which improves the statistical power of the results (Zhang et al., 2023).

The SNR of a single volume acquired with a short TR would be lower compared to that of a longer TR. However, statistical inferences in fMRI as seen previously with the VB index are based on the variation of the voxel's signal over time. Hence, in fMRI the SNR of the fMRI time-series known as the temporal-SNR (TSNR) is of primary importance (Welvaert & Rosseel, 2013). Jahanian et al. (2019) demonstrated that since the number of fMRI volumes collected increases with shorter TR values, the TSNR increases when the scanning time is kept fixed. Furthermore, both Constable and Spencer (2001) and McDowell and Carmichael (2019) who evaluated functional activation in the brain for a range of TR values, recommended the use of shorter TR values (1 to 1.5 s) as it increased BOLD sensitivity, and improved the statistical power of results. Conversely, sub-second TR values might be of little benefit primarily due to the drop in the SNR and the fact that the temporal resolution is limited by the slowly evolving HRF seen previously in figure 4 (Singh et al., 2002).

2.6.2 Flip angle

In conjunction with the TR, the SNR is also dependent on the angle (α) by which the RF pulse flips the net magnetisation during excitation, as illustrated in figure 6. Generally, to maximise the SNR for a particular TR, the flip angle in GRE-EPI sequences is defined to be equivalent to the Ernst angle (α_E) which could be calculated with the following equation (Ernst & Anderson, 1966):

$$cos(\alpha_E) = e^{\frac{-TR}{T_1}} \tag{2.5}$$

As can be seen from equation 2.5, the Ernst angle is dependent on both the TR of the sequence and T_1 of the region under investigation. Since the TR used by most fMRI studies including those in table

1 ($\geq$ 2000 ms) is larger than the T_1 of grey matter ($\approx$ 1331 ms at 3T) (Wansapura et al., 1999), larger flip angles ($>$ 70°) are often favoured. This is evident in the studies analysed in table 1, with the most commonly used flip angle being 90°.

One of the main issues with using large flip angles in fMRI is the increased contamination of inflow artefacts to the fMRI signal. Inflow artefacts result due to the increased blood perfusion to neuronally active regions, altering the apparent T_1 of the brain. This differs from the BOLD contrast, which relies on the relative change in the levels of oxygenated and deoxygenated blood and their differences in T_2^* (Glover et al., 1996). Both BOLD and inflow effects occur simultaneously, but preferentially the signal change associated with inflow effects are reduced in BOLD fMRI through the use of long TR values, lower flip angles (Gao et al., 1996), and simultaneous multi-slice excitation (Howseman et al., 1999).

Although maximum SNR is achieved at the Ernst angle, both Gonzalez-Castillo et al. (2011), and Bodurka et al. (2007) demonstrated that using flip angles which were slightly lower than the Ernst angle did not result in significant reductions in the TSNR. In fact, Bodurka et al. (2007) showed that with a TR of 1000ms and for a high-resolution study (128 $\times$ 128 matrix), it was possible to reduce the flip angle from the theoretical optimal value of around 62° to around 40° with minimal reduction in the TSNR. This is important not only for reducing inflow effects, but also for reducing the specific-absorption rate (SAR) and thus RF-induced patient heating. Furthermore, the use of low flip angles could enhance the outcome of pre-processing steps such as registration and tissue segmentation, since lower flip angles enhance contrast between different brain tissue types (Gonzalez-Castillo et al., 2011).

2.6.3 Readout bandwidth

Another parameter that mediates the SNR is the readout bandwidth (Hz/pixel) which defines the frequency bandwidth from the echo signal transferred onto one voxel. Since noise is distributed across all frequencies, the usage of larger bandwidths increase the proportion of noise in the image, which lowers the SNR (Graessner, J., 2013). However, EPI sequences utilising smaller bandwidths are more prone to magnetic susceptibility related artefacts and distortions (Jezzard & Clare, 1999). In fact, Zou et al. (2005) demonstrated the slight increase in distortions in low bandwidth images (780Hz/pixel) compared with high bandwidth images (1953Hz/pixel). Conversely, due to the increased SNR, Zou et al. (2005) demonstrated an increase in BOLD sensitivity at lower bandwidths.

2.7 Contrast-to-noise ratio

2.7.1 Time of echo

In addition to the SNR, another important image quality parameter in fMRI is the CNR, which is defined as the change in the MR signal between rest and activated states relative to the noise in the image (Stroman, 2016). The differences in T_2^* between activated and baseline states of the time series of images in fMRI constitute the BOLD fMRI signal. However, the observed change in the signal between baseline and activated states is on the order of a few percent, and often exceeds the intrinsic noise only slightly (Jia et al., 2020; Krüger et al., 2001). Thus, optimising CNR mediating parameters such as the time of echo (TE) improves the ability to detect small signal changes by amplifying the contrast between BOLD signal changes and the noise (Schmitt et al., 2012).

Bandettini et al. (1994) and Menon et al. (1993) both demonstrated that the optimal CNR was achieved when the TE equalled the T_2^* baseline relaxation constant of the region under investigation. However, the value for T_2^* varies across different brain regions, across subjects, and across magnetic field strengths (L.-X. Yuan et al., 2021). The average value of T_2^* for both white and grey matter was estimated to be 49ms by Krüger et al. (2001) who measured T_2^* values across different brain regions and across seven adult volunteers at a static magnetic field strength of 3 T. However, anatomical regions which contain tissue with differing magnetic field susceptibilities such as in bone-brain barriers suffer from susceptibility artefacts caused by a local reduction in the apparent T_2^* which reduces the SNR from the affected region (Gorno-Tempini et al., 2002). Therefore, in order to counter the reduction in the SNR caused by magnetic susceptibility effects, a lower TE is generally used in fMRI as analysed in table 1 where most studies used a TE equivalent to 30ms.

2.8 Spatial resolution

The study focused primarily on investigating functional activation with the VB across voxel volumes which determine the spatial resolution of the fMRI image. The spatial resolution of an fMRI study determines the accuracy by which neuronal activation is localised (Hu & Glover, 2009). Generally, the voxels utilised in fMRI studies are larger than those employed with conventional structural MRI, which translates to poorer spatial resolution (Buxton, 2009, p. 126). Most of the studies reviewed in table 1 employed larger voxels of volume 3×3×3mm^3. Conversely, typical voxel volumes in structural MRI of the brain are much smaller in the order of 1×1×1mm^3 (Jenkinson et al., 2017, p. 49). The poorer resolution used typically in fMRI studies may be attributed to the use of EPI which, although provides acceptable imaging times, sacrifices the spatial resolution of the resulting time-series of images (Jenkinson et al., 2017, p. 79).

One of the disadvantages associated with the use of large voxels is the increased susceptibility to the PVE (Weibull et al., 2008), which in fMRI arises as a consequence of voxels being partially filled by both neuronally active tissue and by non-active tissue, as illustrated in figure 7. Since the signal of each voxel is the weighted average from the signals of all tissues encompassed by the voxel, the measured BOLD signal from each voxel would be substantially reduced when compared to the BOLD signal measured had the activated volume encapsulated entirely a voxel (Du et al., 2014). In fact, Mintzopoulos et al. (2009) demonstrated improved detection of BOLD signal when using higher spatial resolution. Furthermore, the PVE limits the accuracy by which boundaries of neuronally active regions are delineated in fMRI (Du et al., 2014).

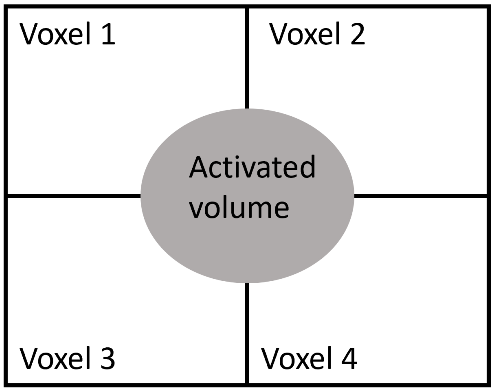

Figure 7. Each voxel in the figure is only partially filled by BOLD activated tissue and due to signal averaging, the measured BOLD signal at each voxel would be substantially reduced. Adapted from Du et al. (2014)

The highly folded nature of the cerebral cortex further increases the probability that voxels encompass heterogeneously functioning tissue, as illustrated in figure 8. The cortical folds entail that voxels may encompass cortical structures that are much further apart than they actually appear (Ciantar et al., 2022). Intuitively, this effect is mostly significant at the boundaries between neuronally active and non-active regions, since voxels may encompass both active and non-active tissue. As discussed previously, the VB index searches for local correlations in the time-series signal of a local neighbourhood of voxels. Consequently, the accuracy by which neuronally active regions are delineated in the VB index is affected not only by the intrinsic signal averaging effects of the PVE but also by the fact that voxels at the boundaries containing both neuronally active and non-active tissue may have a time-course signal that correlates artificially with neighbouring voxels further blurring the edges. These artificial correlations were identified previously by Ciantar et al. (2022) particularly in areas which contained gyral folds.

The effects associated with the PVE can never be fully corrected for (Jenkinson et al., 2017, p. 62). However, the PVE can be reduced by reducing the size of the voxels (Bodurka et al., 2007). The effects associated with the PVE were the primary reason as to why the study focused on investigating functional activation analysis with VB index across pulse sequences with different voxel volumes. Hence, the next few subsections discuss methods on how the size of the voxels may be altered in a pulse sequence. Given that typical fMRI sequences employ large voxels, particular emphasis is placed on methods which may be used to reduce the size of the voxels and improve the spatial resolution.

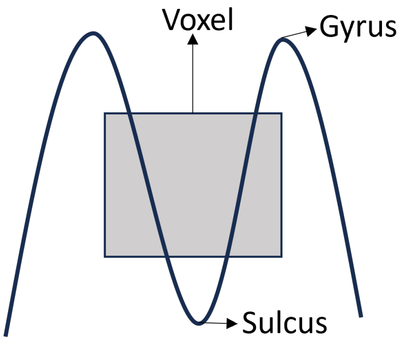

Figure 8. The highly folded nature of the cortex ensures that the actual distance (geodesic distance) between two gyri is much larger than the apparent (Euclidean) distance between them. Thus, the probability of voxels encompassing both gyri increases.

2.8.1 Voxel size

Spatial resolution is predetermined by the volume of the voxels which are themselves determined by three user-selectable parameters: the matrix size, field of view (FOV), and the slice thickness. Typical values for these parameters as defined in fMRI studies are given in table 1. The matrix size denoted by $N_{FE} \times N_{PE}$ represents the total number of measurements made in the frequency encoding (N_{FE}) and phase-encoding (N_{PE}) directions. On the other hand, the FOV is the area in mm^2 covered by the sampling matrix in the phase (FOV_{PE}) and frequency (FOV_{FE}) encoding directions and is denoted by $FOV_{FE} \times FOV_{PE}$. Finally, the depth of the voxel is determined by the slice thickness (Gossuin et al., 2010). The voxel volume is related to these three user-selectable parameters according to equation (2.6) (McRobbie et al., 2006, p. 56):

$$\text{Voxel Volume} = \frac{FOV_{FE}}{N_{FE}} \times \frac{FOV_{PE}}{N_{PE}} \times \text{Slice Thickness} \tag{2.6}$$

Reducing the size of the voxels and achieving a higher spatial resolution requires the acquisition of more phase-encoding and frequency-encoding steps, and the usage of thinner slices, as observed in equation (2.6). In addition to this, the acquisition of more data points increases the readout time for each slice and the scanning time for the entire imaged volume (Hu & Glover, 2009). Consequently, an increase in the TR is required, which reduces the temporal resolution of the study.

Conventional approaches to improving the spatial resolution had focused on improving spatial resolution at the expense of temporal resolution or spatial coverage of the region of interest (Hu & Glover, 2009). For example, Frahm et al. (1993) improved the spatial resolution but sacrificed temporal resolution by increasing the TR. Alternatively, Hoogenraad et al. (1999) increased the spatial resolution but maintained consistent temporal resolution by reducing the number of imaged slices. However, acceleration techniques such as partial Fourier imaging, parallel imaging, multi-shot EPI, multi-band methods or a combination of them provide the possibility of increasing spatial resolution without sacrificing (at least not significantly) both temporal resolution or spatial coverage.

2.8.2 Multi-shot EPI

Multi-shot EPI is a method which divides data acquisition of the EPI sequence into a number of segments. Therefore, instead of acquiring data from each slice in a single excitation, multi-shot EPI acquires data from each slice over multiple excitations (Yun & Shah, 2017). Multi-shot EPI was employed by Hoogenraad et al. (2000) who acquired a matrix size of 256$\times$256 over a 256$\times$256mm^2 FOV by dividing each slice acquisition over four shots, with each shot acquiring 64 phase and frequency encoding lines, resulting in a 1$\times$1mm^2 in-plane resolution. However, a major disadvantage of multi-shot EPI is the increased sensitivity to motion, both physiological or patient related as a consequence of the delay between the acquisition of each segment. Consequently, multi-shot EPI sequences are more susceptible to ghosting artefacts. Apart from this, due to the segmentation of k-space acquisition, multi-shot EPI require longer TR values reducing the temporal resolution (Berman et al., 2021).

2.8.3 In-plane and slice parallel imaging methods

Alternatively, the spatial resolution of the time series of images could be improved by incorporating parallel imaging methods in the EPI sequence, which accelerates data acquisition and enables a higher spatial resolution at a reasonable scanning time (Blaimer et al., 2004). Parallel imaging methods utilise phased array coils, comprised of an array of coil elements surrounding the FOV, with each element containing an independent receiver system capable of reconstructing its own individual image (GE Healthcare, 2005). The coil elements individually undersample the FOV, acquiring fewer phase encoding steps and accelerating data acquisition by the acceleration factor (R). However, as a consequence of the undersampling, the acquired data is aliased and thus several parallel imaging methods have been devised to reconstruct the data into an unaliased image. There are two reconstruction methods; those which reconstruct the data in the image domain such as Sensitivity Encoding (SENSE), and methods which reconstruct the data in k-space such as Generalised Autocalibrating Partially Parallel Acquisition (GRAPPA) (Larkman & Nunes, 2007).

In SENSE, each coil element generates an aliased image. By using the spatially dependent sensitivity profiles of the individual coil elements acquired in an additional reference scan, aliased signals of each pixel are separated creating an unaliased full FOV Image (Pruessmann et al., 1999). Alternatively, k-space based methods such as GRAPPA estimate the unsampled phase-encoding lines for each coil separately. A Fourier transform then generates an individual unaliased image for each coil, which are combined into a full FOV image (Griswold et al., 2002). Reconstructing parallel imaging data with GRAPPA is often preferred in fMRI since it provides superior results when compared with SENSE whose time-series of images are more susceptible to artefacts and noise amplification, resulting in lower SNR (Preibisch et al., 2008).

Fellner et al. (2009) applied GRAPPA for large 3 mm isotropic voxel sizes and noted that the usage of GRAPPA produced images with less geometric distortions when compared to conventional EPI. This result was further iterated by Mintzopoulos et al. (2009) for both smaller $2\times2\times3$ mm^3 and larger $3.1\times3.1\times5$ mm^3 voxels. However, both studies observed a reduction in the TSNR when compared with conventional EPI. In fact, one of the major limitations of parallel imaging methods is the reduction in the SNR which scales by $\sqrt{R}$ as a consequence of the undersampling of phase-encoding lines (Larkman & Nunes, 2007). Despite the reduction in the SNR, Fellner et al. (2009) demonstrated minimal loss in the BOLD signal sensitivity with GRAPPA at an R value of 2, while Mintzopoulos et al. (2009) saw an increase in BOLD sensitivity at the high resolution study with GRAPPA at an R value of 3. These results were also observed by Preibisch et al. (2008) who also demonstrated that an R value of 2 resulted in an insignificant reduction in the BOLD sensitivity for 2^3mm^3 resolution.

The aforementioned studies demonstrate that in-plane parallel imaging methods could be beneficial for EPI image quality, and low R values do not seem to impact BOLD sensitivity significantly. However, parallel imaging methods may not significantly impact the speed of whole brain coverage. This is because although parallel imaging methods skip phase-encoding steps, a suitable TE (30 ms at 3 T) is still required to ensure optimal CNR (Feinberg & Setsompop, 2013). Furthermore, GRAPPA requires the acquisition of reference phase-encoding lines to assist the reconstruction, which as seen with Fellner et al. (2009) could result in a slight increase in acquisition time. Therefore, a more effective way of accelerating data acquisition to improve the spatial resolution is through the simultaneous excitation of multiple slices (SMS), a method that utilises multiband composite RF pulses that excite multiple slices simultaneously (Barth et al., 2016). This results in a scanning time reduction by a factor equivalent to the number of simultaneously excited slices: the multi-band (MB) factor.

The measured signal after a SMS excitation consists of a combination of signals from all the simultaneously excited slices. Therefore, the signal from each slice is not distinguishable since it's aliased with the signal from the other slices (Larkman et al., 2001). Modern SMS methods separate the signals by making use of coil encoding reconstruction techniques utilised in parallel imaging such as image-domain methods (e.g. SENSE) and k-space domain methods (e.g. GRAPPA) (Breuer et al., 2005). However, contrary to parallel imaging, SMS methods do not undersample phase-encoding lines and hence are not subjected to the $\sqrt{R}$ reduction in the SNR previously seen in parallel imaging methods (Setsompop et al., 2012). In addition to this, since both in-plane and slice accelerations rely on parallel imaging reconstructions, incorporating both in the sequence is a possibility.

The usage of SMS in fMRI to speed up acquisition and increase the spatial resolution was endorsed by the 3T fMRI scanning protocol of the Human Connectome Project (HCP) (Uğurbil et al., 2013) who increased the spatial resolution at 3T to 2^3mm^3 by using a high MB factor of 8. In addition to this, at such accelerations, the HCP achieved a sub-second TR (0.72s). The HCP compensated for the large reduction in the SNR at such low TR by scanning volunteers for roughly an hour each. Given that typical fMRI studies are about 15 minutes long (Wall, 2023), this approach by itself might not be optimal.

The usage of the higher MB factors used by the HCP warrants an investigation since it results in higher noise amplification compared with conventional scans, yields lower contrast compared with single-band images (Esteban et al., 2020), and more residual aliasing artefacts as a consequence of imperfections encountered during reconstruction (Uğurbil et al., 2013). Apart from image quality considerations, higher MB factors also necessitate more powerful RF pulses, which translates to a higher SAR (Feinberg & Setsompop, 2013). These factors are likely to be more significant with higher MB factors (Wall, 2023). Risk et al. (2021) evaluated the impact a range of MB factors from 2 to 12 have on functional activation analysis at a 2^3mm^3 isotropic resolution and concluded that there was not a noticeable advantage between a MB factor of 4 and 8. The reduction in the MB factor would require an increase in the TR as observed with Rastegarnia et al. (2023) in table 1 where the TR increased to 1.49s at a MB factor of 4 and a 2^3mm^3 resolution. Nevertheless, this TR value is within the recommended TR values of McDowell and Carmichael (2019) and Constable and Spencer (2001).

2.8.4 Partial Fourier

Another method which may be used to speed up the acquisition and improve spatial resolution is partial Fourier which utilises the property of conjugate symmetry exhibited by k-space data, whereby an image could be generated by sampling a little over half of the desired matrix. Then, the remaining k-space data is estimated by calculating the hermitian conjugate of the acquired data (Feinberg et al., 1986). Partial Fourier acquisitions have two main advantages; the reduced scan time and the reduction in the TE. The reduction in scan time could subsequently be used to optimise the spatial resolution and reduce the aforementioned PVE discussed previously. On the other hand, the reduction in the TE with partial Fourier occurs because fewer phase-encoding lines are acquired before reaching the centre of k-space, reducing the effective TE. This is important in high resolution scans which necessitate a higher TE since more phase-encoding lines are acquired before sampling the centre of k-space. For example, for full k-space coverage, a 128×128 matrix size requires a TE which is roughly twice as large as the optimal TE of 30ms (Jesmanowicz et al., 1998). In such instances, partial Fourier has the capacity to lower the TE to a value that is closer to the optimal value thereby maximising the CNR (Hyde et al., 2001; Jesmanowicz et al., 1998). Accurate partial Fourier reconstructions in EPI require larger portions of k-space to be sampled, and most scanner manufacturers allow only up to a quarter of k-space to be reconstructed. Thus, partial Fourier is not as effective in reducing in-plane scan time when compared with parallel imaging, but its capacity to lower the TE in higher resolution scans has lodged it as part of the high resolution sequence devised by the HCP (Uğurbil et al., 2013).

2.9 Proposed sequences and study design

The present study aims to assess the VB index across various voxel sizes, which could help in optimising the spatial resolution of the pulse sequences used. Upon a comprehensive review of literature, the use of SMS acceleration with as low an MB factor as possible may be the optimal method for improving spatial resolution. The main advantage SMS has over parallel imaging is that they do not suffer from intrinsic SNR reductions. Conversely, the increase in motion induced artefacts make multi-shot EPI undesirable. At higher resolution, the use of partial Fourier may be useful to reduce the effective TE to a value closer to the theoretical optimal 30ms value. Although shorter TR is preferred for optimal temporal resolution, the issue with the SNR at higher resolutions could be alleviated with moderate TR values between 1.5 to 2 s. The MB factor should be scaled accordingly to maintain such TR values. The loss in temporal resolution could be circumvented by the use of block-design motor tasks with an optimal block length ranging between 10 and 20 s (Maus et al., 2010), although this may not be applicable for a wide range of experiments. The TE is proposed to be kept fixed as close to the optimal 30ms value as possible through the application of partial Fourier. Flip angles that are slightly lower than the Ernst angle may be used to reduce the SAR and inflow effects. Finally, the receiver bandwidth may be kept as low as possible to increase both BOLD sensitivity and SNR.

2.10 Conclusion

This chapter presented a critical, comprehensive and review of the literature associated with the study. In the next chapter, we will describe and discuss the research methodology used in the study.

Scanning Parameter	**Median Value**	**Range of Values**
Time of Repetition (ms)	2000	720 →2500
Time of Echo (ms)	30	30 →37
Slice Thickness (mm)	3.2	2 →5
Field of View (mm^2)	220×220	192×192 →240×240
Matrix Size	64×64	64×64 →104×90
Number of Slices	32	30 →72
Flip Angle (α)	90°	52° →90°

Table 1. The median and range of values of the major scanning parameters of gradient-echo EPI sequences used in local correlation studies with 3T MRI scanners. The data was obtained through a literature review of eight studies (Dong et al., 2014; Liu et al., 2010; Rastegarnia et al., 2023; Shukla et al., 2010; Tian et al., 2012; Uğurbil et al., 2013; L.-X. Yuan et al., 2021; Zang et al., 2004).

3 Research methodology

3.1 Introduction

The aim of the study was to assess functional activation analysis across different pulse sequences with differing voxel volumes. This chapter presents the research methodology used throughout the study. The methodology section includes the pulse sequences devised and used during the MRI scanning sessions, and an underpinning of the data analysis conducted in the study. Finally, the limitations encountered in the research methodology shall also be discussed.

3.2 Research approach

The study made use of a mixed research approach, since both quantitative and qualitative methods were employed. The analysis of fMRI data was performed quantitatively using data-driven and model-based algorithms. The results obtained at each sequence were compared quantitatively together using similarity metrics, and qualitatively with literature. Furthermore, comparison of the image quality at each sequence was also performed quantitatively.

3.3 Research strategy

A prospective experimental research strategy was employed, since primary data was collected from research volunteers recruited for the study using an MRI scanner, and analysed quantitatively and qualitatively. An experimental strategy was chosen since fMRI data was collected using pulse sequences to assess functional activation across voxel volumes. The data was collected prospectively, since the data had yet to be collected using specific pulse sequences.

3.4 Data collection technique

Primary MRI data was collected by direct observation from a total of 10 research volunteers scanned with an MRI scanner. Other data collection techniques were unsuitable given the objectives.

3.5 Data collection procedure

The study was carried out in an MRI room within Mater Dei Hospital (Msida, Malta), equipped with a 3T Siemens MAGNETOM Vida (Siemens Healthcare GmbH, Erlangen, Germany) MRI system. The MRI system had been in clinical and research service for less than five years. The BioMatrix Head/Neck 64 channel coil (Siemens Healthcare GmbH, Erlangen, Germany) was used throughout the study for RF transmission and reception of the MRI signal. The study assessed the VB index across three different fMRI pulse sequences, each with a distinct voxel volume, on ten research volunteers.

3.5.1 Participants

A cohort of ten volunteers (9 males and 1 female) were recruited and scanned. At the time of acquisition, the age of the volunteers ranged from 21 to 55 years. Seven of the volunteers were right-handed, and three volunteers were left-handed.

3.5.2 MRI scanning protocols

The volunteers were positioned in a supine position on the MRI's gantry, and the head of the volunteers was placed in the centre of the head coil. Each volunteer was asked to keep as still as possible and were scanned for a period of approximately 1 hour. At any time during the study, volunteers could stop the scan by squeezing a ball to alert the healthcare professionals in charge.

First, a high resolution T1-weighted structural image was acquired for each volunteer using an axial MPRAGE sequence (resolution of 1$\times$1$\times$1 mm^3 isotropic voxels, TE of 2.66ms, TR of 2190ms, Inversion time of 925ms, α of 8°, GRAPPA with R = 2). The scanning time for the T1-weighted structural image was approximately 5 minutes.

One of the major limitations of EPI sequences is their sensitivity to magnetic field inhomogeneities which causes susceptibility distortions and intensity non-uniformities (Hutton et al., 2002). In order to correct for magnetic field inhomogeneities in the preprocessing phase, gradient field maps were acquired for each volunteer. The gradient field maps were acquired with a resolution of 2.5$\times$2.5$\times$2.5mm^3, a TR of 529ms, TE$_1$ of 4.92ms, TE$_2$ of 7.38ms, and a flip angle α of 60°. The total acquisition time for the field mapping sequence for each volunteer was 1 minute and 36 seconds. After acquiring the structural image and the field map, three gradient echo EPI sequences were performed on each subject with voxel volumes of $1.8 \times 1.8 \times 1.8$mm^3, $2 \times 2 \times 2$mm^3, and $2.5 \times 2.5 \times 2.5$mm^3 respectively. Hereafter, these three separate EPI sequences shall be dubbed as the 1.8^{3}mm^3, 2^{3}mm^3, and 2.5^{3}mm^3 sequences respectively. The study aimed to assess functional activation with the VB index across voxel volumes. Therefore, the scanning parameters of the three EPI sequences were kept consistent except for the voxel's volume. This was done to isolate as much as possible the impact of voxel volume on functional activation analysis. Theoretically, the higher resolution sequence (1.8^{3}mm^3) would have poorer SNR and require more drastic acceleration factors. Hence, the scanning parameters of the pulse sequences were optimised for the 1.8^{3}mm^3 resolution sequence. To achieve resolution of 2^{3}mm^3, and 2.5^{3}mm^3, the matrix size and slice thickness were scaled accordingly.

In order to achieve isotropic voxels of volumes 1.8^{3}mm^3, an interleaved SMS acquisition with an MB factor of 4 was used. The TR was set to a value of 1.84s, lower than the TR of most of the studies outlined in table 1. In order to achieve a reasonable TE of 34ms, which was close to the theoretical optimal value of 30ms, Phase Partial Fourier of 6/8 was used. A FOV of 241×241mm^2, a base resolution of 134×134, and slice thickness of 1.8mm were used to achieve voxels of volumes $\approx$1.8^{3}mm^3. The Ernst angle given by equation (2.5) was $cos^{-1}(e^{\frac{-1840}{1331}}) \approx 75.4°$. To minimise in-flow contamination and since it was shown that slight reductions in the flip angle results in negligible reduction in the TSNR (Bodurka et al., 2007), a slightly lower flip angle of 65° was chosen. The readout bandwidth was kept as low as possible at 2072Hz/pixel. The scanning parameters of the EPI sequence were kept mostly consistent for the larger 2mm and 2.5mm isotropic voxel sequences. However, some scanning parameters had to be adjusted either because it was required by the MRI device or because it was necessary to achieve the desired voxel volume. Table 2 summarises the scanning parameters affixed for each EPI sequence. A total of 393 volumes were acquired with each BOLD sequences. The scanning time for each BOLD sequence was approximately 12 minutes.

3.5.3 fMRI paradigm

During the three EPI BOLD sequences, the subjects performed repetitive block design finger tapping tasks. The fMRI experiment consisted of a baseline/rest condition where no intended motor activity was expected, followed by periods where the subjects performed finger tapping tasks with their right thumb or index. Instructions were provided to the subjects prior to each fMRI sequence via a mirror attached to the Siemens head coil, which reflected instructions from a 40-inch MR-compatible monitor. This monitor, a Nordic Neuro Lab (NNL) (NordicNeuroLab, Bergen, Norway) device, was situated in the control room.

	Voxel Volume (mm^3)		
Sequence Parameters	**1.8**^{3}	**2**^{3}	**2.5**^{3}
TR (s)	1.84	1.84	1.84
TE (ms)	34	34	34
Flip angle ($^\circ$)	65	65	65
MB factor	4	4	4
Phase Partial Fourier	6/8	6/8	6/8
FOV (mm^2)	241 $\times$ 241	240 $\times$ 240	240 $\times$ 240
Matrix Size	134 $\times$ 134	120 $\times$ 120	96 $\times$ 96
Slice Thickness (mm)	1.8	2	2.5
Bandwidth (Hz/Px)	2072	2084	2084

Table 2. Summary of the scanning parameters used for each of the three EPI sequences with voxels of volumes $1.8^3 mm^3$, $2^3 mm^3$, and $2.5^3 mm^3$ respectively.

The design of the baseline and stimulus conditions, presented at different intervals were developed using the PsychoPy[1] software (Peirce et al., 2019). Prior to the scanning session, the subjects were informed about the tasks they would perform during the fMRI acquisition. Furthermore, before each fMRI sequence began, subjects viewed an information screen as seen in figure 9a on the NNL monitor for one minute.

The PsychoPy paradigm was synchronised with the fMRI volume acquisition through the NNL SyncBox. Before acquiring each fMRI volume, the SyncBox sent a signal to the computer presenting the stimulus in the form of an “s” keyboard response. Thus, after the PsychoPy code presented the instructions shown in figure 9a, it waited for the MRI volume acquisition to commence in order to continue. During this waiting period, the participants were instructed to wait for the pre-scanning to complete as seen in figure 9b. The EPI sequence was started when the instructions provided by figure 9b were presented. After the pre-scan was complete, the MRI system prior to capturing the first fMRI volume triggered

---

[1] https://psychopy.org/index.html

the PsychoPy paradigm via the NNL SyncBox which then sent the first “s” keyboard response to the computer. In response to this, the PsychoPy paradigm started presenting the stimuli.

Instructions:

Tap your right thumb when you see a red cross on the right.

Tap your right index when you see a blue cross on the right.

Please wait for the MRI pre-scanning to complete

(a) (b)

Figure 9. The pre-scanning instructions shown to the volunteers prior to the fMRI experiment.

The stimuli were presented for a period of approximately 18.4s (10 fMRI volumes) followed by a rest period equivalent in duration. During the stimuli presentation, subjects were instructed to tap either their right thumb or their right index finger as seen in figures 10a and 10c respectively. As seen in both figures, subjects were asked to tap repeatedly their right thumb if they saw a red cross on the right side of the screen and their right index finger if they saw a blue cross on the right side of the screen. During the rest condition presented after each stimulus, subjects were asked to stare at a small cross at the centre of the screen, as seen in figure 10b. The order of presentation of the stimuli was randomised, but each stimulus was accompanied by a rest period equal in duration.

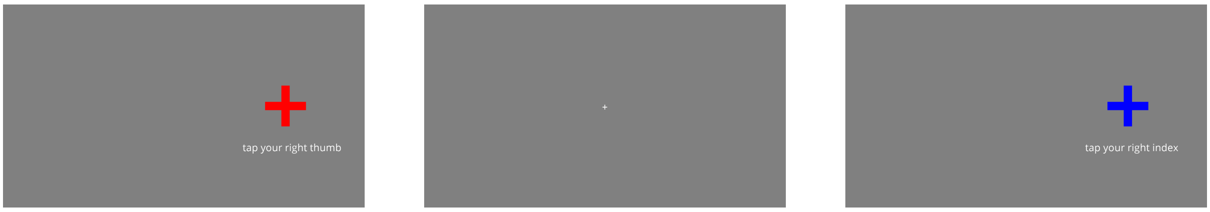

(a) (b) (c)

Figure 10. The stimuli and baseline conditions presented to the volunteers during the fMRI experiment.

3.6 Data collection tool

The data collection tools used in the study were a 3T Siemens MAGNETOM Vida (Siemens Healthcare GmbH, Erlangen, Germany) MRI system, and a Head/Neck 64 channel coil (Siemens Healthcare GmbH, Erlangen, Germany).

3.7 Data analysis technique

After the MRI data was collected, it was prepared for analysis (pre-processed) and then analysed to acquire the functional activation maps. The data processing pipeline performed may be divided into three major portions. First, the data was structured and organised into an appropriate data structure standard. Then, the data was pre-processed and assessed for quality. The fMRI data was then analysed using the VB index (Bajada et al., 2020) and the GLM (Friston et al., 1994).

3.7.1 Data organisation

The first portion of the data analysis procedure involved organising the MRI data acquired from the MRI scanner in the Digital Imaging and Communications in Medicine (DICOM) file format in a structured way. The data was structured according to the brain imaging data structure (BIDS) standard (Gorgolewski et al., 2016). Figure 11 provides an illustration of an MRI data set that was organised into the BIDS standard. As shown in the figure, the BIDS standard organises the raw DICOM (.dcm) data acquired from the scanner into a series of subfolders for each participant (e.g. sub-01). Within each volunteer's subfolder, the BIDS standard organises structural and functional MRI images in separate subfolders denoted by "anat" and "func" respectively as seen in figure 11. The main advantage that the BIDS convention offers is that it facilitates data preprocessing by allowing pre-processing software packages to automatically pre-process the data without requiring manual intervention (Gorgolewski et al., 2016).

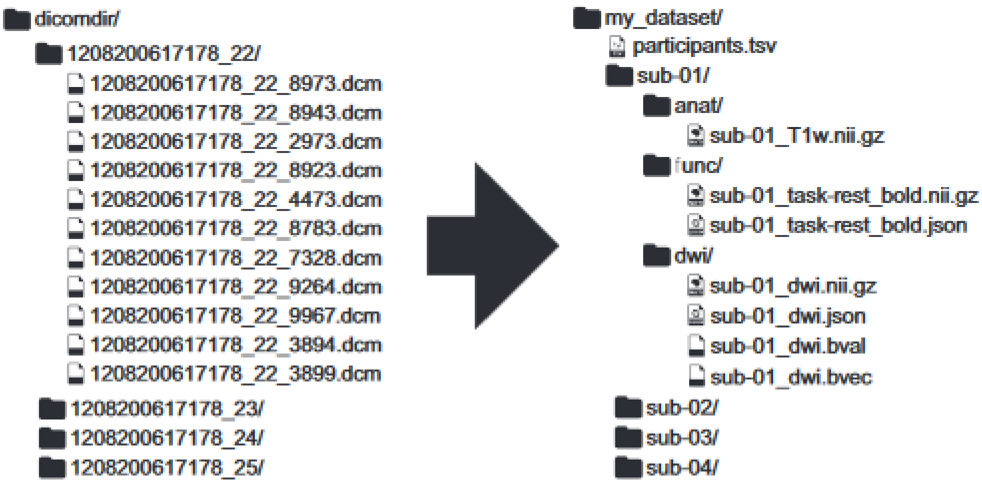

Figure 11. Illustration of a dataset structured according to the BIDS standard. Adopted from Gorgolewski et al. (2016) licensed under CC BY 4.0.

The data was organised in BIDS format using “BIDSKIT” [2], a Python based tool that converted the DICOM data into Neuroimaging Informatics Technology Initiative (NIfTI) format and organised the data according to the BIDS standard (Tyszka, 2024).

3.7.2 Image quality

The raw data quality of the organised data was then checked for quality using “MRIQC” version 23.1.0, an open-source tool that automates quality control protocols for both structural and functional MRI data (Esteban et al., 2017). MRIQC computed several image quality metrics for both structural and functional data. The image quality metrics outputted by MRIQC were used to compare data quality obtained with the various pulse sequences.

The SNR and the TSNR of the three different fMRI sequences tested determined by MRIQC were compared statistically. A One-way repeated measures ANOVA test was used to determine whether there were statistical differences in the mean SNR and TSNR of the three sequences. An alpha level of 0.05 was used. When statistical significance was indicated by the ANOVA test, post-hoc pairwise comparisons were performed using the Holm-Bonferroni test to identify which pairs of sequences differed significantly.

3.7.3 Data preprocessing

After being organised according to the BIDS standard, the raw MRI data was pre-processed to prepare the data for fMRI analysis. The aim of pre-processing is to reduce the impact non-neural sources have on the fMRI data, and to detect and correct for artefacts present in the data (Esteban et al., 2019). Two of the most common artefacts in fMRI acquisitions are susceptibility distortions and motion artefacts. Susceptibility distortions, which are caused by inhomogeneities of the magnetic field, primarily occur at air-tissue boundaries such as the sinuses. These distortions lead to artefacts in the fMRI data, and cause signal loss and geometric distortions in the affected regions (Poldrack et al., 2011). Figure 12 shows a slice from the mean fMRI image of one of the volunteers acquired with the 2.5^3mm^3 sequence highlighting substantial signal loss in the frontal lobe characteristic of susceptibility distortions. Alternatively, motion artefacts, primarily caused by involuntary movement of the volunteer lead to a mismatch of the location of subsequent images in an fMRI time-series (Poldrack et al., 2011).

---

[2] https://github.com/jmtyszka/bidskit

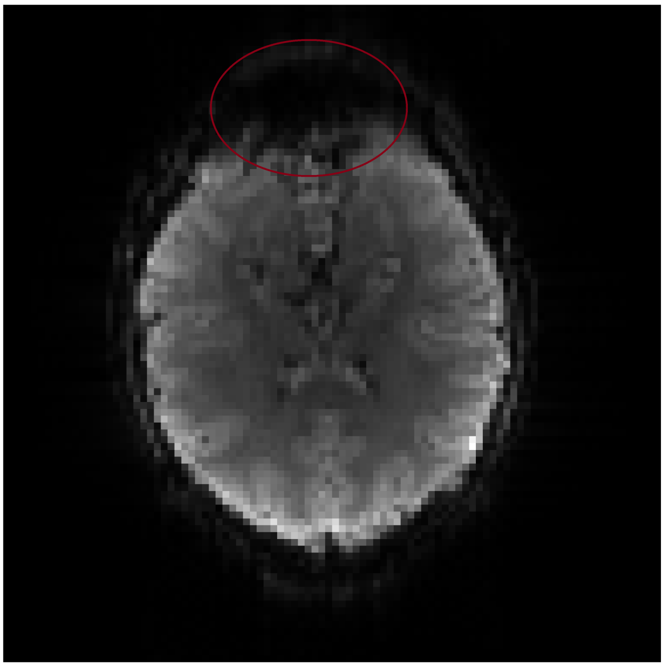

Figure 12. Highlighted are the susceptibility artefacts present in the raw fMRI data of one of the volunteers acquired with the 2.5^{3}mm^3 sequence.

In this study, fMRIprep (Esteban et al., 2020; Esteban et al., 2019) version 23.2.0 was used to pre-process the raw MRI data. Figure 13 illustrates the pre-processing pipeline performed by fMRIprep. As seen from the figure, the pipeline is split into two pre-processing streams that process both structural and functional MRI data.

The T1-weighted image was first corrected for voxel intensity non-uniformity (INU) (Tustison et al., 2010), which causes a smooth intensity variation across the image even within the same tissue type (Belaroussi et al., 2006). The skull was then removed from the INU corrected T1-weighted image, rendering a skull-stripped T1-weighted image.

Apart from pre-processing the structural T1-weighted image, fMRIprep also pre-processed the BOLD fMRI data in a separate pipeline as seen in figure 13. First, a BOLD reference image was generated for each sequence and subject, composed of the average of the time-series of images. From this reference image, a brain mask was created eliminating regions outside the brain that are irrelevant for fMRI analysis (Gilford, 2024). Head motion was corrected for by rotating and translating the time series to align them with the reference BOLD image determined in the first step of the fMRI preprocessing pipeline (Esteban et al., 2020). The susceptibility distortions discussed previously in figure 12, caused by air-tissue interfaces, were addressed by fMRIprep using the field maps acquired for each subject. These field maps were used by fMRIprep to compute the local magnetic field inhomogeneities and quantify the distance that each voxel was shifted by (Poldrack et al., 2011). In addition to this, the fMRI data of the volunteers were aligned with their respective T1-weighted image (co-registration). Finally, for inter-subject analysis, fMRIprep computed the transformations required for spatially normalising the co-registered fMRI data to the common Montreal Neurological Institute (MNI) 152 template (Esteban et al., 2020).

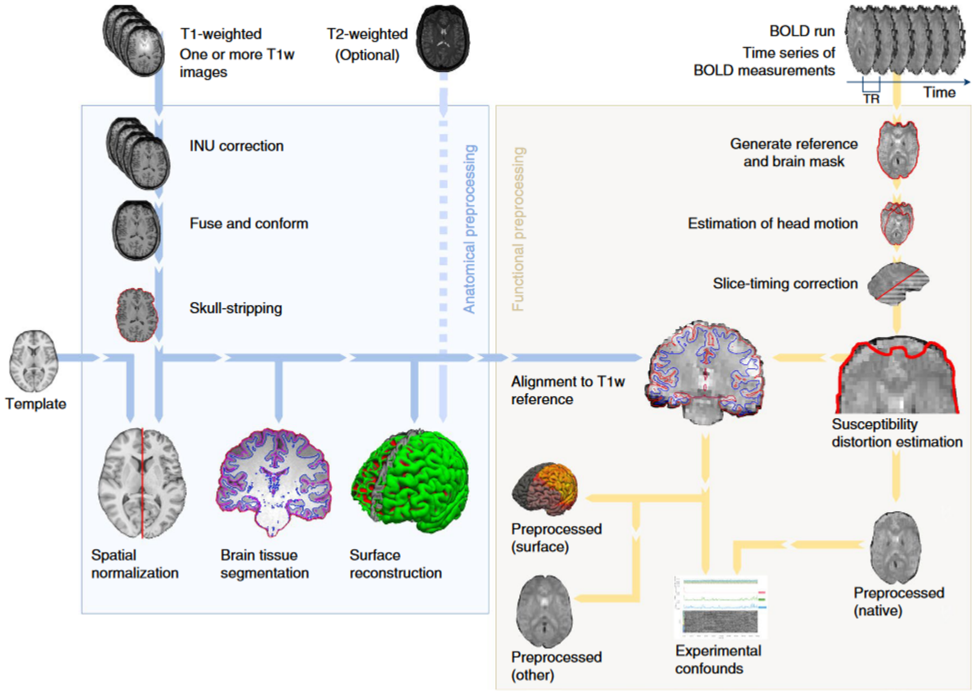

Figure 13. The pre-processing pipeline conducted by fMRIprep for the structural data and functional data. Adopted from: Esteban et al. (2020) licensed under CC BY 4.0. Note that for this study, the “fuse and conform” step for the anatomical pipeline was not performed, since only one T1-weighted image was acquired at each run. In addition to this, “slice timing correction” for the functional pipeline was not applied, as the temporal interpolation performed may propagate artefacts along the time-series of images (Poldrack et al., 2011).

3.7.4 FMRI data analysis

The preprocessed fMRI data acquired at each resolution and for each subject was analysed using two different data analysis techniques, a model-based method; the GLM, and a data-driven technique; the VB index. The next couple of sections discuss briefly the theory and implementation of the GLM, and the VB index.

3.7.5 The General Linear Model

The standard data analysis technique employed in fMRI is the GLM, which models the time-series signal of each voxel into one or several variables known as regressors (Jenkinson et al., 2020). The aim of the GLM is to find statistically which voxels in the fMRI time-series of images have a time-course signal that correlates with the expected signal variation upon performing a task during the fMRI experiment (Monti, 2011; Poline & Brett, 2012). In the GLM, the time-series signal of each voxel is modelled as a weighted summation of multiple regressors plus some residual error term that accounts for the differences between the fitted model and the time-series signal. In matrix notation, the GLM of a single voxel may be represented by equation (3.1), where **Y** is an $N \times 1$ vector that contains the voxel intensity of a particular voxel over the entire time-course (over N volumes) (Jenkinson et al., 2020; Monti, 2011; Poline & Brett, 2012).

$$\mathbf{Y} = \mathbf{X}\boldsymbol{\beta} + \boldsymbol{\epsilon} \tag{3.1}$$

Apart from this, the matrix term **X** commonly known as the design matrix is an $N \times M$ matrix with each column containing a different regressor. In fMRI, the regressors represent the expected MRI signal time-course of a neuronally active voxel i.e., the predicted response to a stimulation. In addition to the predicted responses, the design matrix may also contain additional regressors of non-interest (hereafter confounds) embedded modelling nuisance variables such as motion and low-frequency drifts, that if not modelled, reduce the statistical power of the results (Jenkinson et al., 2020; Monti, 2011; Poline & Brett, 2012). Each regressor in the design matrix is weighed by an appropriate scaling parameter $\boldsymbol{\beta}$ that associates a magnitude to its respective regressor, indicating the degree to which the data is explained by the regressor. The scaling parameters $\boldsymbol{\beta}$ are typically estimated using the ordinary least squares approach, which minimises the squared difference between the observed time-series signal and the model's prediction. Finally, ϵ represents the residual error, i.e., the differences between the model fit and the observed data (Bishop, 2006).

The pre-processed fMRI data acquired at each sequence and for each subject was analysed with the GLM using an algorithm developed with Python 3.11. The GLM analysis script used during the GLM analysis, available on GitHub [3], utilised the *Nilearn* library version 0.10.3[4] which includes several built-in functions and tools for GLM analysis. The first portion of the GLM analysis involved computing a first level GLM analysis on the fMRI data for each subject individually. The first level GLM performed consisted of a

---

[3] https://github.com/KristianGalea/M.Sc-Dissertation-Code.git

[4] https://nilearn.github.io/stable/index.html

voxelwise (mass univariate) analysis, meaning that the GLM was applied independently to each voxel in the fMRI time-series (Jenkinson et al., 2020). For each volunteer, three separate first level GLM runs were performed, one for each pulse sequence. Firstly, the design matrix expressed by **X** in equation (3.1) which contained both the experimental regressors and the confound regressors was created for each first-level run. Figure 14 illustrates the design matrix used in the first level GLM computation for a particular volunteer. The figure is subdivided into a series of columns each representing a different regressor. The rows of the matrix represent the signal associated with the regressor at each fMRI volume during the fMRI time-series.

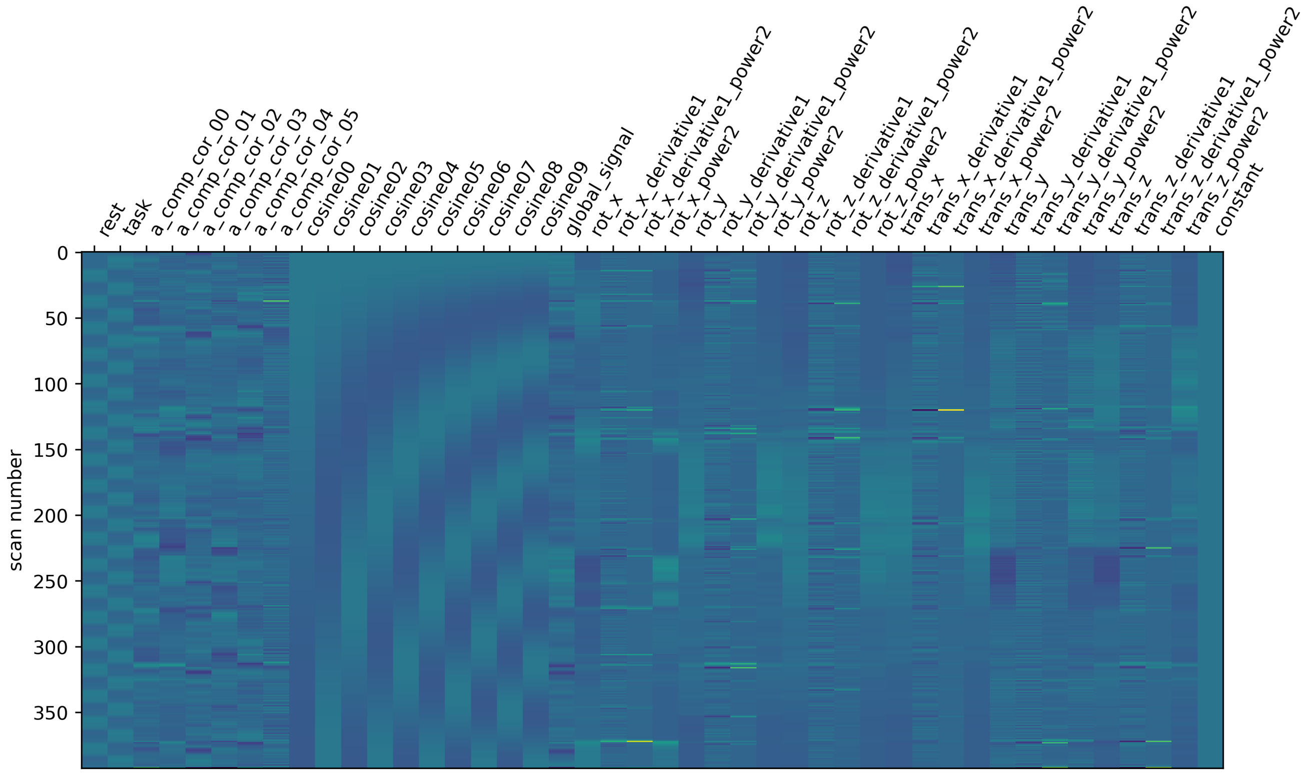

Figure 14. The design matrix of one of the volunteers used in the computation of the first level GLM analysis

The first two columns of the design matrix seen in figure 14 contained the two essential experimental regressors; a regressor that models BOLD signal response during the period where the volunteer performed a task and the second experimental regressor that accounted for the rest period. The two experimental regressors modelled the BOLD response, i.e., the expected time-course signal of a voxel encompassing BOLD activated tissue. The expected signal change in response to a brief stimulus due to the BOLD effect was modelled by the Glover HRF, which is illustrated by figure 15a. The volunteers performed block-design tasks for 10 MRI volumes ($10 \times TR$) followed by an equal-length rest period. Therefore, the experimental regressors were modelled by convolving the Glover HRF with the stimulus function of a duration of $10 \times TR = 10 \times 1.84s$. Figure 15b illustrates the stimulus function given by the boxcar function having a duration of 18.4 s which was convolved with the Glover HRF to yield the experimental regressors for a single task-period. This function corresponded to the idealised expected MRI signal change in a voxel that is active by the BOLD effect during the task-window.

(a) The Glover HRF

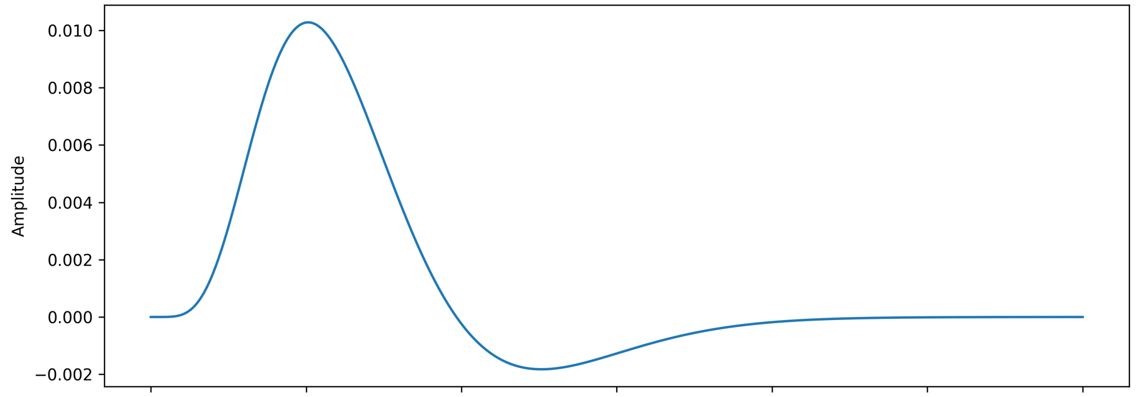

(b) The stimulus function and experimental regressor

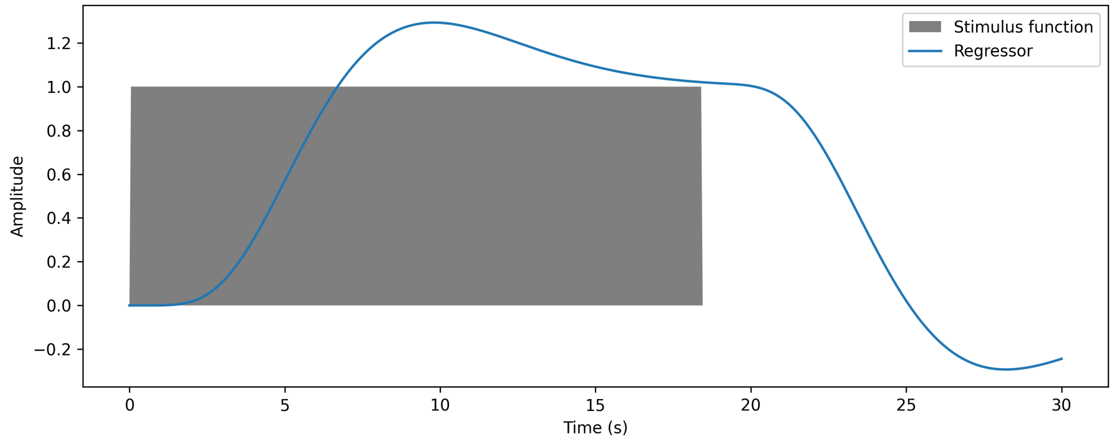

Figure 15. The experimental regressor (b) is given as the convolution of the Glover HRF (a) with the stimulus function (grey shaded box in b). The experimental regressor yields the idealised expected MRI signal change in response to the 18.4s task window.

Apart from the experimental regressors, a number of confound regressors were also modelled in the design matrix and can be visualised by the additional columns of the design matrix in figure 14. These confound regressors were all outputted during the pre-processing of the fMRI data by fMRIprep. The confounds selected were based on recommendations by various literature (Esteban et al., 2020; Goebel, 2014; Parkes et al., 2018; Power et al., 2012; Satterthwaite et al., 2013).

Included in the design matrix were six motion regressors, representing the 6 rigid-body motion parameters; 3 parameters that modelled translation and 3 parameters that modelled rotation in the x, y, z dimensions. In the design matrix of figure 14, these are labelled as “trans_x”, “trans_y”, “trans_z”, “rot_x”, “rot_y”, and “rot_z”. Although these 6 rigid motion parameters provide an estimate of volunteer head motion, they are not able to account fully for head motion (Parkes et al., 2018). Therefore, higher order motion parameter regressors were included in the design matrix, since it was shown that these confounds improved motion regression performance, particularly for data with higher head motion (Satterthwaite et al., 2013). The higher order motion parameter regressors included the temporal derivatives of the 6 rigid-body motion regressors (e.g., rot_x_derivative1), the square of the 6 rigid-body motion regressors (quadratic regressors, e.g., e.g., rot_x_power2), and the temporal derivatives of the quadratic regressors (e.g., rot_x_derivative1_power2). Consequently, a total of 24 motion related confound regressors were included in the design matrix.

Apart from this, two additional confound regressors were considered that provided information on which fMRI volumes exhibited large and sudden motion artefacts (outlier volumes). These two confound regressors were the framewise displacement and the derivative of the root mean squared variance over voxels (DVARS) suggested by Power et al. (2012). Framewise displacement is a parameter that quantifies the bulk head motion (in mm) between one fMRI volume in the time-series to the next. Alternatively, DVARS refers to the difference in root-mean-square of the intensity of a volume with a subsequent volume (Power et al., 2012). Following the suggestions of Satterthwaite et al. (2013) and Power et al. (2012) respectively, a threshold of 0.5 mm was chosen for the framewise displacement and a threshold of 2 for the standardised DVARS. Consequently, volumes which exhibited a framewise displacement and a DVARS that exceeded the threshold were eliminated (scrubbed) from the fMRI GLM analysis.

Physiological and MRI scanner noise sources often manifest as low-frequency drifts in the voxel's time-course signal and may cause a substantial reduction in the statistical power of the GLM results (Goebel, 2014). The low frequency physiological or the scanner related sources of noise were modelled and accounted for using firstly a set of low frequency regressors provided by fMRIprep known as discrete cosine transform (DCT) basis regressors which were added to the design matrix, labelled as "cosineXX". The second group of confound regressors to model physiological noise sources were extracted by fMRIprep after principal component analysis (PCA), a technique that characterises relevant signals from noise within a region of interest. The signals extracted by PCA are referred to as principal components, and are ordered according to the amount of information (variance) that they explain from the original data (Greenacre et al., 2022). In fMRIprep, PCA is applied on anatomical brain regions which are unlikely to contain BOLD activity (e.g., cerebrospinal fluid and white matter) (Behzadi et al., 2007). In accordance with Esteban et al. (2020), the top six principal components that explained the most variance were included as confound regressors to the design matrix of the GLM, labelled as "a_comp_cor_xx". The final confound regressor included in the design matrix which have been shown to improve confound suppression performance when used with PCA is global signal regression (“global_signal”), defined as the average time-series signal across the entire brain (Parkes et al., 2018).

In the study, the GLM was used to perform hypothesis testing and make a statistical inference on which voxels exhibited statistical differences between the task and rest regressors, which would point to BOLD activation. It is good to point out that the “thumb” and “index” events were not separated as separate regressors but grouped in a single regressor; “task”. This was done because the subsequent analysis technique, the VB index does not analyse different task events separately. Thus, a fairer comparison between the two techniques was achieved by grouping the thumb and index events. In the GLM, the null hypothesis tested was that there was not a positive statistical difference between the size (weight) associated with the task and rest regressors. The alternate hypothesis was that there was a positive statistically significant difference between the weight associated with the task regressor and the rest regressor. The one-sided alternate hypothesis formulated tested can be expressed as a contrast vector by (3.2):

$$\boldsymbol{\beta_2} - \boldsymbol{\beta_1} > 0 = \boldsymbol{\beta_2} > \boldsymbol{\beta_1} \tag{3.2}$$

Where $\boldsymbol{\beta_2}$ and $\boldsymbol{\beta_1}$ relate to the weights of the task and rest regressors respectively.

Prior to the application of an appropriate test statistic to test the null hypothesis, the fMRI data was spatially smoothened through a convolution process with a Gaussian filter. This is a commonly employed preprocessing step in fMRI analysis and involves sliding a kernel across the image and replacing the intensity of the voxel at the centre of the kernel with a weighted average of the neighbourhood voxel’s intensity (Jahn, 2019). Although spatial smoothing effectively blurs the image and reduces spatial resolution, it was adopted in the GLM algorithm for two main reasons. First, smoothing improves the SNR of the fMRI images (Poldrack et al., 2011). Second, smoothing reduces the effect of inter-subject anatomical variability i.e., accounts for the fact that the anatomical position of functional activity will vary between volunteers due to inter-subject anatomical variation (Alahmadi, 2021). Therefore, smoothing increases the probability of detecting common activation patterns in group-wise analysis. The degree of smoothing depends on the full width at half maximum (FWHM) of the Gaussian filter. Weibull et al. (2008) investigated the optimal FWHM at different voxel volumes. In this study, the FWHM value suggested by Weibull et al. (2008) at 1.8^{3}mm^3 resolution was used throughout for consistency. Therefore, throughout the study, smoothing was performed with a FWHM of 2.67$\times$1.8mm $=$ 4.806 mm.

Then, after the data was smoothened, a one-sample t-test, that assessed the significance of the contrast vector (Ardekani & Kanno, 1998) of equation (3.2) was applied for each voxel individually (mass-univariate analysis). The first level analysis outputted statistical maps for each first-level run containing the t-values computed at each voxel (hereafter t-maps). After the individual statistical t-maps were computed for each volunteer and sequence, a second-level analysis was performed in order to make a broader inference of functional activation at a group level. The aim of this step was ultimately to determine which voxels showed significant task-rest contrast consistently at a group level. In order to perform a second-level analysis, the statistical t-maps acquired had to be spatially normalised to a common template brain. This involved transforming the images in a way that a particular voxel would contain the t-scores from the same anatomical location in each of the volunteers (Stroman, 2016). The MNI152NLin2009cAsym T1-weighted template[5] with a resolution of 1^3mm^3 was chosen as the template brain, and fMRIprep as part of the preprocessing pipeline, outputted the transformations necessary to transform the fMRI data registered to the T1-weighted image of the volunteer to the MNI152NLin2009cAsym space. The transformations to MNI space were achieved using the transformation tools provided by the Advanced Normalization Tools (ANTs)[6] library.

Then, a voxel-wise one-sample t-test was performed on the spatially normalised t-maps to test the null hypothesis (H_0) that voxels did not exhibit statistically significant task-rest contrast across all subjects (J. Chen, 2019). An alpha level of 0.05 was chosen to decide whether to reject the null hypothesis. The statistical test was applied for each voxel separately, which meant that on average, 5% of all voxels in the image would be statistically false positives (type I error). Given the large number of voxels in an image, the number of false positives can consequently amount to the several thousands. This problem, which is known as the "multiple testing problem", was alleviated by applying the Bonferroni correction method. The Bonferroni method controlled the familywise error rate (FWE) i.e., the probability of a type I error anywhere in the image (Poldrack et al., 2011). The Bonferroni method outputted a statistical threshold at a Bonferroni corrected level of significance 0.05, which was used to threshold the second-level t-map such that voxels which had a t-score that exceeded this threshold were deemed as statistically significant rejecting the null hypothesis. The second-level analysis was repeated for each sequence separately.

3.7.6 The Vogt-Bailey index

The second data analysis technique used to analyse the fMRI data was the VB index, whose theoretical foundations have already been discussed in the literature review. Unlike the GLM which relies on a model of the expected BOLD response via the design matrix, the VB index is a data-driven approach,

---

[5] https://github.com/templateflow/tpl-MNI152NLin2009cAsym.git

[6] https://github.com/ANTsX/ANTsPy.git

hypothesising functional activation results purely on the data without the use of a user-defined model. The VB's non-reliance on a design matrix is seemingly advantageous: 1) it facilitates data analysis since the fMRI data analysis only requires the fMRI data itself as opposed to the GLM which requires a user-specified design matrix, 2) the fact that the VB does not rely on a model means that it may be sensitive to neuronal activity that does not follow the same pattern as the experimental regressors for example seen in figure 15b. However, this advantage also comes with a drawback; the VB index does not regress out confounding signals such as motion, which the GLM addresses through the use of confound regressors.

To address this issue, the current optimal approach for VB index analysis is to denoise the fMRI data prior to performing analysis using the VB index. Prior work on identifying the optimal denoising pipeline for the VB index was conducted by Aalberdi (2024) who tested several open-source Python based denoising pipelines[7] (Kliemann et al., 2022) on task-based fMRI data. The pipeline which provided the optimal results for the VB index (labelled as pipeline "B" by the authors of the denoising pipeline) was used to denoise the task-based fMRI data of this study. The denoising pipeline B, developed based on the work of Satterthwaite et al. (2013) involves several denoising steps designed to regress out confounding signals from the MRI data. The denoising pipeline contains several denoising steps, some of which were utilised in the GLM previously, such as motion regression, and scrubbing outlier fMRI volumes.

The first step in the VB analysis involved denoising the fMRI data with the aforementioned Satterthwaite et al. (2013) denoising pipeline "B". Thus, the Satterthwaite et al. (2013) denoising pipeline was applied on the fMRI data co-registered to the respective T1-weighted image, for each volunteer and sequence. Afterwards, the VB analysis was performed on the denoised data using two separate VB index approaches. In the first method (hereafter VB method 1), the smoothing operations performed during the GLM analysis were replicated i.e., the denoised fMRI data was smoothened prior to VB analysis to provide as fair a comparison with the GLM as possible. The VB index[8] (Bajada et al., 2020; Farrugia et al., 2022; Farrugia et al., 2024) was then applied on the denoised and smoothened data. In the second VB index approach (hereafter VB method 2), the denoised and unsmoothened data was first analysed with the VB index, and then smoothing was applied on the resulting VB maps. This approach ensured that the VB index, which is an edge detection technique, was applied on unsmoothened data preserving the contrast between the edges of functionally distinct regions. In both approaches, in order to allow cross-subject analysis, the results obtained for each volunteer were spatially normalised to the MNI152NLin2009cAsym template using the transforms provided by fMRIprep as was done during the GLM analysis.

---

[7] https://github.com/adolphslab/rsDenoise.git

[8] https://github.com/VBIndex/py_vb_toolbox.git

A one-sample t-test was then applied for each VB approach separately to determine which voxels had a VB value that was significantly higher than the baseline during the experiment across all the volunteers. The VB statistical analysis was carried out using Python and the script used is available on GitHub[9]. A one-sample t-test was applied against an appropriate baseline. The distribution of VB values in both methods across the participants exhibited the shape of a skewed Gaussian, indicating asymmetry in the VB index distribution, as seen in figure 16 which shows the probability density function of the VB index data in method 2 of one participant at a particular sequence. Hence, the median VB index averaged across all volunteers was chosen as the baseline due to the median's lower sensitivity to outliers when compared to the mean value (Leys et al., 2013). A one-sample t-test with an alpha level of 0.05 determined which voxels exhibited a VB index that was significantly higher than the baseline across all subjects. As with the GLM analysis, the Bonferroni correction method was also applied to control the rate of false positives, and the resulting t-maps obtained were thresholded to include voxels with a Bonferroni corrected level of significance of 0.05. As with the GLM, this analysis was performed for the fMRI data acquired at each sequence separately.

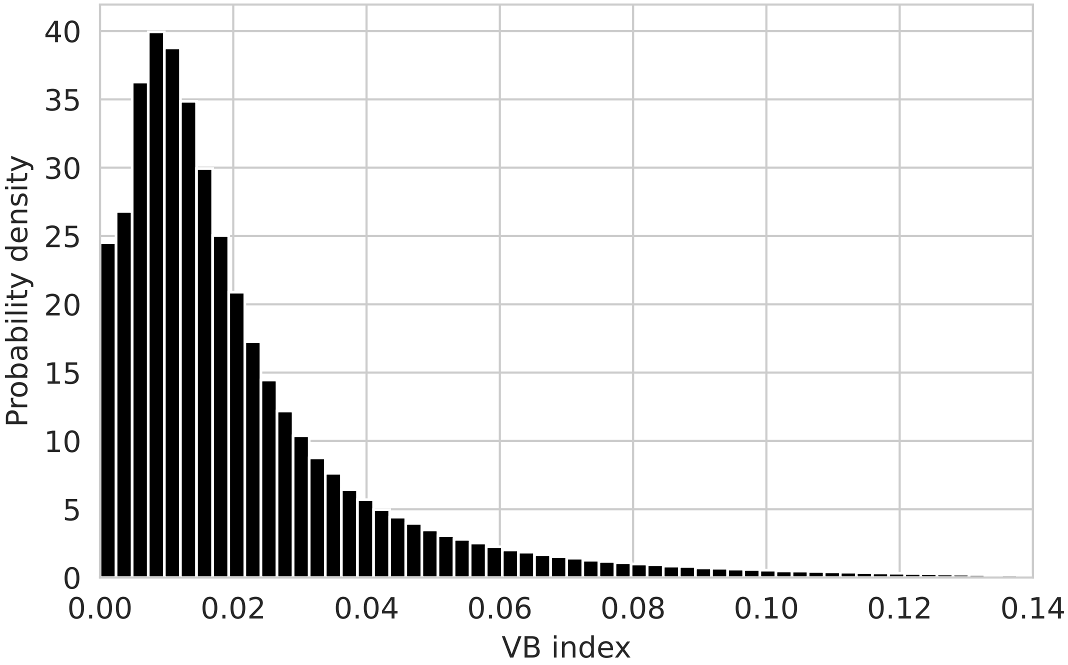

Figure 16. The probability density function of the VB indices of VB method 2 from the resulting spatially normalised VB map of one of the volunteers for the 1.8^3mm^3 sequence.

---

[9] https://github.com/KristianGalea/M.Sc-Dissertation-Code.git

3.7.7 Accuracy of functional localisation

The GLM and VB index analysis outputted group-level statistical t-maps thresholded to include voxels with a t-score that had a Bonferroni corrected level of significance α of 5% (p-value < 0.05). These voxels highlighted brain areas that showed group-wise statistically significant evidence to reject the null hypothesis and accept the alternate hypothesis. It is important to note that the alternate hypothesis for the GLM and VB index analysis differ. For the GLM, the alternate hypothesis posits that voxels exhibit statistically significant task-rest contrast across the group. For the VB index, the alternate hypothesis suggests that voxels have a VB index that is statistically higher than the baseline VB index across the group. Nevertheless, as discussed in the literature review, a high VB index suggests that the voxel's time-course signal is highly correlated to its neighbouring voxels which is analogous to local homogeneity (Farrugia et al., 2022; Farrugia et al., 2024). Hence, both the statistically significant results of the GLM and the VB index shall be treated as signs of functional activation, and hereafter the thresholded statistical maps shall be referred to as activation maps.

The next step in the analysis involved comparing the resulting activation maps with those of established literature. This part of the analysis aimed to assess the accuracy by which the cortical areas responsible for thumb and index movements were mapped, and to determine if spatial resolution impacted this accuracy. It is good to point out that due to the lack of available ground truth, this step had to be performed subjectively through comparison with the results of established literature.

As an approximate guideline, the results of Gountouna et al. (2010) were used to determine the brain regions that should have been activated during the present fMRI experiment in response to the thumb and index finger tapping tasks. Gountouna et al. (2010) studied functional activation in fMRI with a cohort of 14 volunteers subjected to right-handed finger tapping tasks, each scanned on three separate MRI scanners. Figure 17 illustrates group-level fMRI activation maps highlighting brain regions with statistically significant differences at a group level between the right-handed random finger tapping condition and the rest condition. The portion of the activation maps highlighted in red represent regions deemed statistically significant across all MRI scanners tested. Conversely, the blue and green regions were only deemed as statistically significant in two and one MRI scanners respectively. Robust and consistent activations were observed in the left hemisphere, particularly in the left premotor, left primary motor and left supplementary motor areas. In addition to this, activations in the thalamus, and the cerebellum were also observed. These activation maps were taken as a guide of the brain regions expected to be significantly activated during the present task-based experiment.

Situated in the primary motor cortex that forms part of the frontal lobe is the "hand knob" area, an

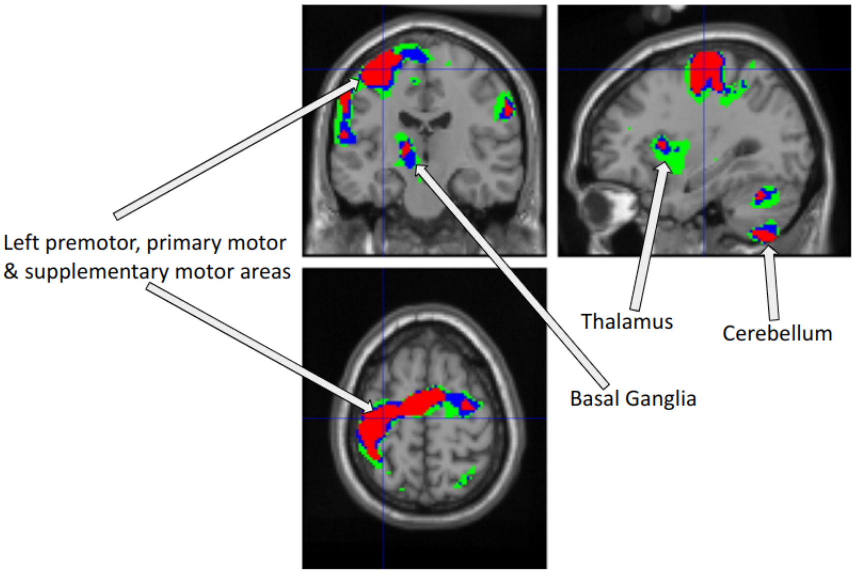

Figure 17. Labelled activation maps highlighting voxels deemed significantly activated between random finger tapping and rest conditions. The regions highlighted in red represent overlapping regions of activation between 3 MRI scanners. Alternatively, blue and green regions represent regions highlighted as active in two and one MRI scanners only respectively. Image adapted from Gountouna et al. (2010) with permission from Elsevier.

anatomical landmark that is of particular interest for this experiment. The “hand knob” is an “omega” shaped anatomical structure responsible for hand motor function (Pimentel et al., 2011). Figure 18 shows slices from the average T1-weighted image of the volunteers normalised to MNI space highlighting the “hand knob” region. The image is presented in radiological view with the left/right side portions of the image labelled by “L” and “R” respectively.

3.7.8 Cross-comparison between sequences and data-analysis techniques

The resulting fMRI activation maps obtained at each pulse sequence were quantitatively compared using similarity metrics to assess the effect resolution has on functional activation results. The Python script used to compute the similarity metrics is available on GitHub[10]. Firstly, the total number of statistically significant voxels were computed for each of the results obtained at each sequence and data analysis technique. Then, a pairwise similarity metric, the Dice-Sørensen coefficient (hereafter Dice coefficient) was used to assess the spatial similarity of the activation maps across pulse sequences. The Dice coefficient is defined as the ratio of the number of statistically significant voxels that overlap in both maps to the average number of statistically significant voxels. Thus, the Dice coefficient (D) was

---

[10] https://github.com/KristianGalea/M.Sc-Dissertation-Code.git

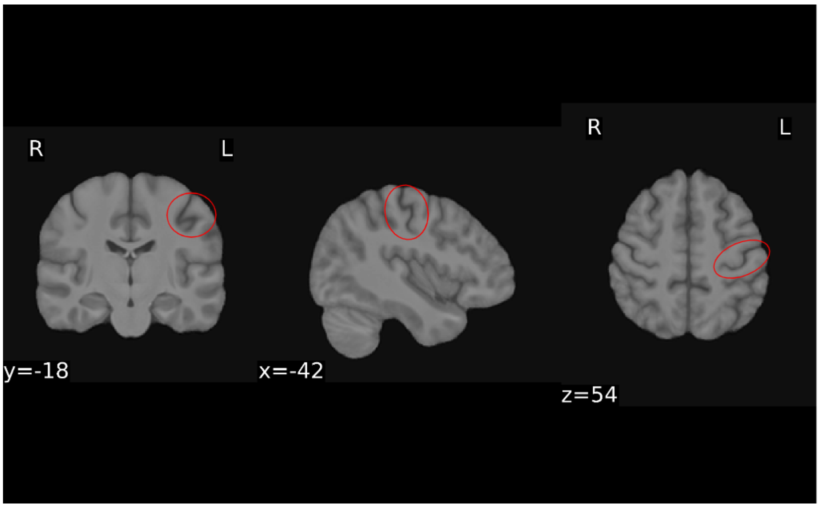

Figure 18. Coronal, sagittal and transverse slices displaying the “hand knob” region highlighted in red.

calculated using equation (3.3) (Bach et al., 2022).

$$D = \frac{2|A \cap B|}{|A| + |B|} \tag{3.3}$$

Where $|A \cap B|$ represent the intersection of the two activation maps (A and B) i.e., the total number of voxels deemed significant in both maps. Alternatively, $|A|$ and $|B|$ represent the total number of statistically significant voxels in activation maps A and B respectively. In case of perfect congruence of the activation maps, the Dice coefficient outputs a value of 1, and 0 otherwise. The Dice coefficient was used to assess the pairwise spatial similarity of the activation maps across pulse sequences. Thus, for each pairwise comparison, the total number of statistically significant voxels in both maps ($|A| + |B|$) was calculated. Then, for each pairwise comparison, the intersection of the activation maps ($|A \cap B$) was determined by calculating the total number of voxels which were labelled as statistically significant in both activation maps. The Dice coefficient was then calculated using equation (3.3).

The activation from the GLM were also compared with those from the VB index. This analysis aimed to determine how closely the VB index results matched to those of the GLM, the standard data analysis technique in fMRI (Poline & Brett, 2012). The Dice coefficient was not optimal for this task because although some overlap between the GLM and VB results was expected, particularly in the brain areas of figure 17, they are intrinsically different data analysis techniques. Primarily, the VB’s non-reliance on a design matrix may translate to the detection of brain activity that does not follow the traditional “expected” fMRI BOLD signal response i.e., the experimental regressors seen in figure 15b. If such were the case, the GLM results were only expected to be a subset of the VB index’s results. As a result, while the intersection of the two activation maps $|A \cap B|$ may be substantial, a large difference in the size of

A and B can penalise the Dice coefficient by amplifying the denominator $|A| + |B|$. In other words, the Dice coefficient penalises differently sized activation maps. Instead, this analysis assessed the degree of alignment between the VB results and the GLM, while recognising that statistically significant voxels unique to the VB method do not necessarily indicate inaccuracies. Consequently, the Overlap coefficient was deemed as better suited since it is defined as the ratio of the intersection of the two activation maps divided by the total number of voxels in the smaller of the two activation maps (i.e., the activation map which contains the least amount of significant voxels $min(|A|, |B|)$). The overlap coefficient was thus calculated using equation (3.4) (Alarcon, 2019).

$$OC = \frac{|A \cap B|}{min(|A|, |B|)} \tag{3.4}$$

Pairwise comparisons between the GLM and VB results acquired with the two approaches were conducted with the Overlap coefficient across all the pulse sequences tested. For each cross-comparison, the intersection of the VB index and the GLM was determined by calculating the total number of voxels which were labelled as statistically significant in both activation maps. This result was divided by the number of statistically significant voxels in the activation map that contained the least number of statistically significant voxel, as seen in equation 3.4.

3.8 Ethical considerations

The study was approved by the University Research Ethics Committee of the University of Malta with the application ID of FHS-2023-00578. The notification of ethics approval is provided in appendix A.

3.9 Limitations of the research methodology

The research methodology had a number of limitations which should be considered particularly for future work.

1. The analysis performed with the VB index involved a statistical test to identify voxels with a VB index that was statistically higher than the median VB value. Ideally, future work should incorporate a control group consisting of fMRI data from volunteers acquired during a resting-state fMRI experiment should be used. Statistical comparison may be performed between the task group

and the control group. However, due to the time limitations, the study did not feature a control group.

2. The scanning parameters of the 2^3mm^3 and 2.5^3mm^3 sequences were kept as consistent with those of the 1.8^3mm^3 sequence to study the impact of spatial resolution on functional activation results. This meant that the scanning parameters of the 2^3mm^3 and 2.5^3mm^3 sequences were not optimised for the 2^3mm^3 and 2.5^3mm^3 resolution, which could impede image quality.
3. The study utilised a relatively small sample size of 10 volunteers, which may limit the replicability of the results (Turner et al., 2018).

3.10 Conclusion

The research methodology of the study was presented in this chapter. The next chapter presents the results obtained.

4 Results

4.1 Introduction

The aim of the study was to investigate functional activation analysis with the VB index in task-based fMRI using different pulse sequences with varying voxel volumes. A total of ten research volunteers were recruited and scanned using three separate fMRI acquisitions with voxel volumes of 1.8^3mm^3, 2^3mm^3 and 2.5^3mm^3 respectively. The volunteers were subjected to a block design finger-tapping experiment. The fMRI data was then preprocessed, and analysed using two separate data analysis techniques. The first is the standard fMRI data analysis technique, the GLM, and the second technique is the VB index which has not yet been rigorously tested across pulse sequences. This section presents the results obtained with both data analysis techniques, and any measures of image quality obtained at each sequence.

4.2 Image quality assessment

The image quality of the raw fMRI data from the three tested pulse sequences was assessed using MRIQC. Figure 19 displays the variation in the static SNR (19a) and TSNR (19b) across the three different pulse sequences tested. The fMRI images of the 2.5^3mm^3 sequence exhibited the highest mean TSNR and mean SNR at 49.890 ± 9.533 and 2.264 ± 0.186 respectively. The mean SNR and TSNR reduced to 37.456 ± 4.606 and 2.163 ± 0.188 respectively at 2^3mm^3. Finally, the mean TSNR and SNR were 31.680 ± 2.548 and 2.185 ± 0.176 respectively at 1.8^3mm^3.

A One-way repeated measures ANOVA tested for significant differences in the mean SNR and TSNR across pulse sequences, with a level of significance of 0.05. When the ANOVA test indicated statistical significance, the Holm-Bonferroni post-hoc performed pairwise statistical comparison. The ANOVA test showed that the static mean SNR varied significantly across pulse sequence resolution (F(2, 18)=11.782, p=0.003). The Holm-Bonferroni test concluded that the mean static SNR obtained with the 2^3mm^3 sequence did not differ significantly from the mean SNR of the 1.8^3mm^3 (p=0.411). On the other hand, the mean SNR of the 2.5^3mm^3 sequence differed significantly from the 1.8^3mm^3 (p<0.001) sequence and the 2^3mm^3 (p=0.005) sequence. In addition, the ANOVA test indicated that the mean TSNR varied significantly across the pulse sequences (F(2, 18)=19.094, p=0.001). The Holm-Bonferroni test concluded that the mean TSNR obtained with the 1.8^3mm^3 sequence differed significantly from the mean TSNR of the 2^3mm^3 (p=0.006) sequence and the 2.5^3mm^3 (p=0.004) sequence. Similarly, the mean TSNR of the 2^3mm^3 sequence and the 2.5^3mm^3 sequence differed significantly (p=0.006).

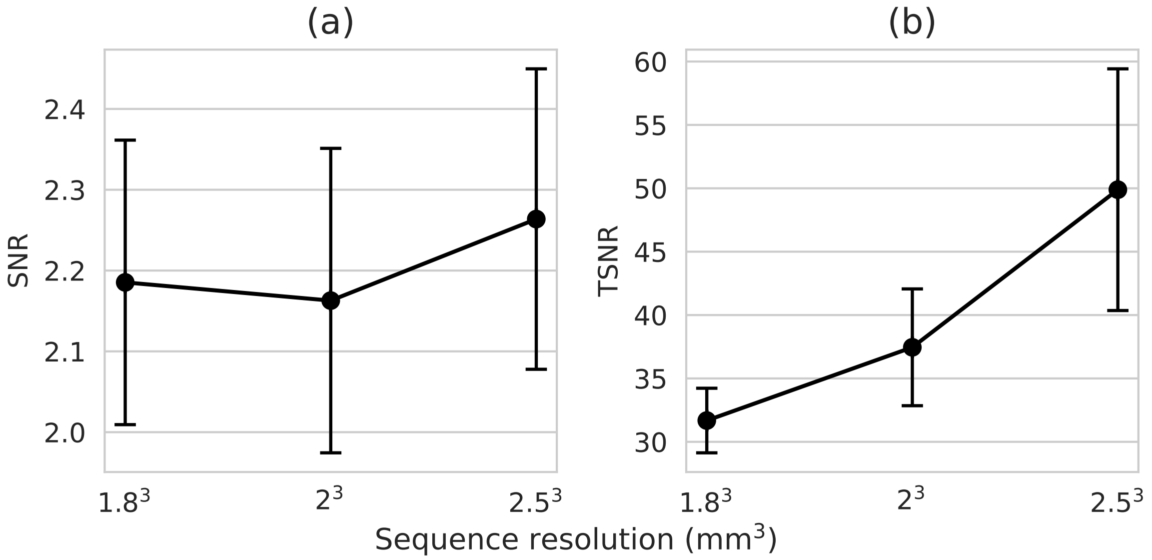

Figure 19. The variation in the average SNR (a) and TSNR (b) across pulse sequence resolution as outputted by MRIQC. Error bars indicate 95% confidence intervals for the mean SNR and TSNR. The confidence intervals ($\Delta\bar{x}$), determined with Python 3.11 were calculated using the Student's t-distribution: $\Delta\bar{x} = \pm t_{\alpha,n-1}\frac{s}{\sqrt{n}}$ (Boos & Hughes-Oliver, 2000), where s is the sample standard deviation, n is the size of the sample, α is the significance level defined as 0.025 to obtain the 95% confidence intervals, and $t_{\alpha,n-1}$ is the critical t-value. The mean SNR of the 2.5^3mm^3 sequence differed significantly from both the 2^3mm^3 and 1.8^3mm^3 sequences. However, there was not a statistically significant difference between the mean SNR of the 2^3mm^3 and 1.8^3mm^3 sequences. Alternatively, the mean TSNR of all pairs of sequences differed significantly.

4.3 fMRI data analysis

4.3.1 General Linear Model

The fMRI data was initially analysed using the GLM, which is the standard technique for detecting functional activation in fMRI. The GLM analysis involved a first-level voxel-wise one-sample t-test performed at a subject level, which assessed the statistical significance between the task and rest conditions of the fMRI experiment. The statistical t-maps from each volunteer were then combined in a group-level analysis to test the null hypothesis that no voxels showed statistically significant task-rest contrast across all subjects, using an alpha level of 0.05. The Bonferroni correction method adjusted the p-value to control the FWE, and the corrected p-value was used to threshold the resulting statistical t-maps obtained during the group-level analysis to include only statistically significant voxels in the final activation maps. Figure 20 illustrates the resulting group-level activation maps obtained from the GLM analysis at all the sequences. The first column displays a coronal slice and a transverse slice from the resulting activation maps. On the other hand, the second column displays sagittal slices from the resulting activation maps. Each row of the figure corresponds to the activation maps acquired at a particular sequence. The voxel's intensity in the activation maps correspond to the t-statistic derived during the GLM analysis. Only voxels with statistically significant t-values at the group-level ($p<0.05$), following Bonferroni correction, are included in the activation maps. For the statistically significant voxels included in the figure, the alternate hypothesis was accepted that the voxels included exhibited group-wise statistically significant differences between the task and rest conditions of the fMRI experiment. The activation maps are overlayed on the average T1-weighted image of the volunteers normalised to MNI space. Furthermore, included for each subfigure displayed in figure 20 are the coordinates at which the slices displayed were acquired (e.g., x=-42 in mm) in MNI space. For the sagittal slices, negative coordinates, e.g., -42 denote that the slice was taken from the left hemisphere of the brain. The left-right brain orientation for the coronal and transverse slices displayed in the first column of figure 20 are dubbed by "L" and "R". The position of the slices were chosen such that they include portions of the motor cortex particularly the hand knob region seen previously in figure 18, the cerebellum, the basal ganglia, the thalamus and the occipital lobe. The format for the presentation of the activation maps seen in figure 20 shall be repeated hereafter.

Figure 20a and figure 20b display coronal, transverse and two sagittal slices respectively from the group-level GLM activation map acquired with the 1.8^3mm^3 sequence. Only statistically significant voxels ($p<0.05$) are included in the activation maps. Similarly, coronal, transverse, and sagittal slices from the group-level GLM activation map acquired with the 2^3mm^3 sequence are found in figures 20c and 20d respectively. Finally, figure 20e shows a coronal and transverse slice, while figure 20f shows sagittal slices from the group-level GLM activation map of obtained with the 2.5^3mm^3 sequence. To allow a better visualisation of the volumetric statistical maps, particularly statistically significant areas not necessarily shown in the slices presented previously, figure 21 illustrates the activation maps projected on a transparent "glass" brain. Figures 21a, 21b, and 21c illustrate the glass-brain GLM projections obtained for the 1.8^3mm^3, 2^3mm^3 and 2.5^3mm^3 sequences respectively.

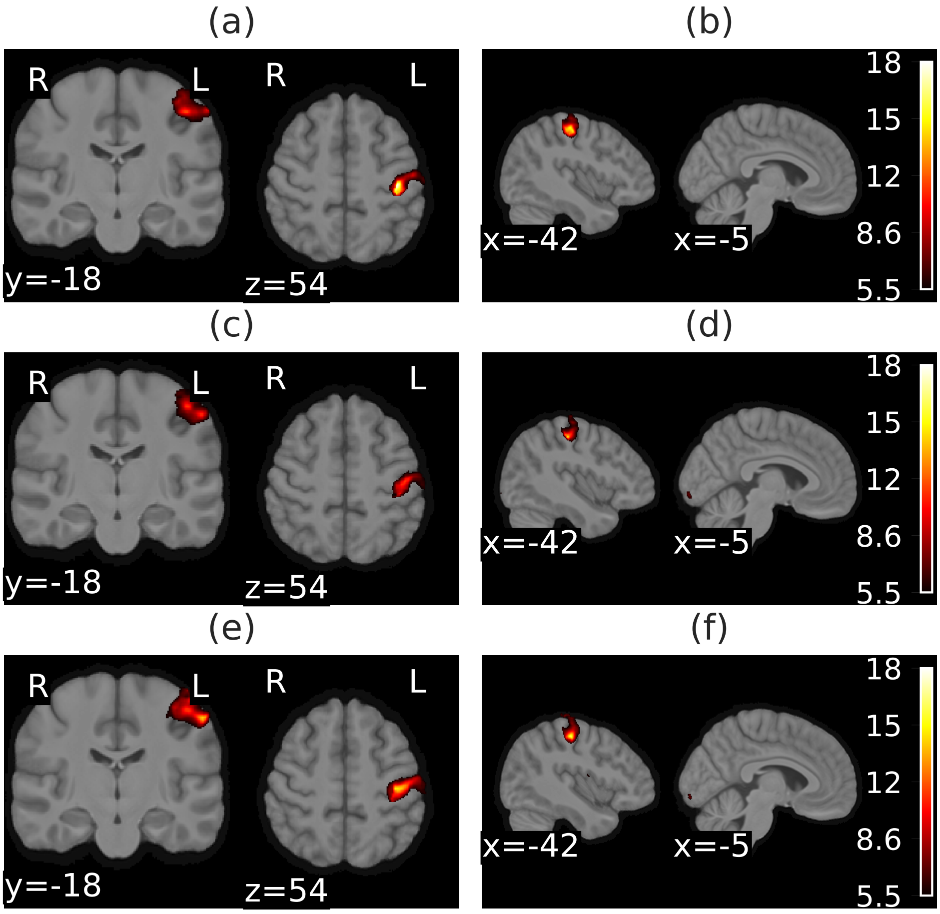

Figure 20. The activation maps signifying statistically significant voxels across the group (Bonferroni corrected p-value < 0.05) obtained during GLM analysis. The first row (a, b) displays the t-maps from the 1.8^3mm^3 sequence, the second row (c, d) displays the t-maps from the 2^3mm^3 sequence, and the third row (e, f) displays the t-maps from the 2.5^3mm^3 sequence.

4.3.2 Vogt-Bailey Index

The preprocessed fMRI data was then also analysed using the VB index, a data-driven data analysis technique which has not yet been tested across pulse sequences. Unlike the GLM, the VB index does not rely on a design matrix to regress out confounding signals arising due to for example motion. Hence, a denoising algorithm was first applied on the fMRI data prior to the VB analysis. Then, the denoised data of each volunteer acquired at each sequence was analysed with the VB index using two separate approaches; VB method 1 and VB method 2. The first approach aimed to simulate the smoothing operations as performed with the GLM to allow as fair a comparison. Hence, in the first approach, the denoised data was first smoothened using the FWHM used in the GLM, and the smoothened denoised data was analysed with the VB index. The second VB approach aimed to preserve the functional edge contrast of the original data. Hence, in the second approach, the VB index was applied to the denoised

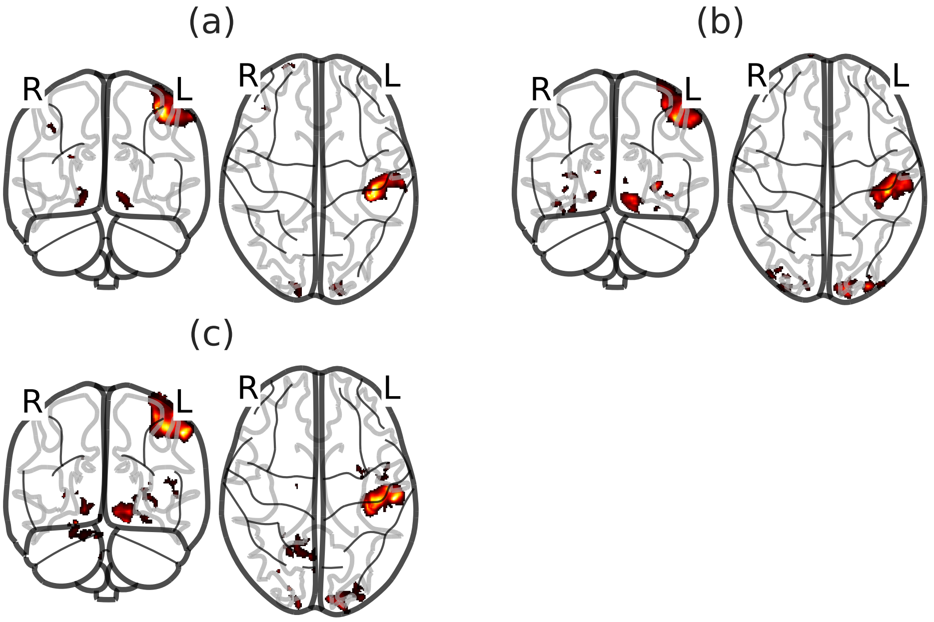

Figure 21. Activation maps obtained with the GLM projected on a transparent rendering of a brain. Figures (a), (b) and (c) represent activation maps obtained with the 1.8^3mm^3, 2^3mm^3, and 2.5^3mm^3 sequences respectively.

and unsmoothened data and then the resulting VB maps were smoothened using the FWHM used with the GLM. In both cases, a one sample t-test was performed with Bonferroni correction to test the null hypothesis that no voxels had a VB index that was statistically higher ($p<0.05$) than the median VB index across all volunteers. The analysis was performed for each sequence separately.

The Bonferroni thresholded statistical maps acquired with VB method 1 are given in figure 22. Coronal, transverse and sagittal slices from the activation maps of the VB index approach 1 obtained with the 1.8^3mm^3 resolution sequence are shown in figures 22a and 22b. Included in the activation map are voxels with sufficient statistical evidence ($p<0.05$) to accept the alternate hypothesis that the voxels have a VB index that is statistically higher than the median VB index at a group level. In addition to this, figures 22c and 22d show coronal, transverse and sagittal slices from the activation maps obtained with the VB index method 1 for the 2mm^3 sequence. Finally, the VB activation map obtained with VB method 1 for the 2.5^3mm^3 sequence are provided by figures 22e and 22f which show coronal, transverse and sagittal slices respectively.

The Bonferroni thresholded statistical maps acquired with VB method 2 are given in figure 23. Figures 23a and 23b show coronal, transverse and sagittal slices from the activation maps of the VB index method 2 for the 1.8^3mm^3 sequence. Coronal, transverse and sagittal slices from the resulting activation map acquired when analysing the fMRI data acquired of the 2^3mm^3 sequence using the VB method 2 are given in figures 23a and 23b. Similarly, figures 23c and 23d display slices acquired from the activation maps obtained when analysing the 2.5^3mm^3 sequence with the VB index method 2. As was done with the GLM, the VB activation maps obtained with both VB approaches were projected on transparent “glass” brains, which are shown in figure 24. Figures 24a, 24b, and 24c illustrate the glass-brain projections obtained with VB method 1 for the 1.8^3mm^3, 2^3mm^3 and 2.5^3mm^3 sequences respectively. Alternatively, figures 24d, 24e, and 24f illustrate the glass-brain projections obtained with the VB method 2 for the 1.8^3mm^3, 2^3mm^3 and 2.5^3mm^3 sequences respectively.

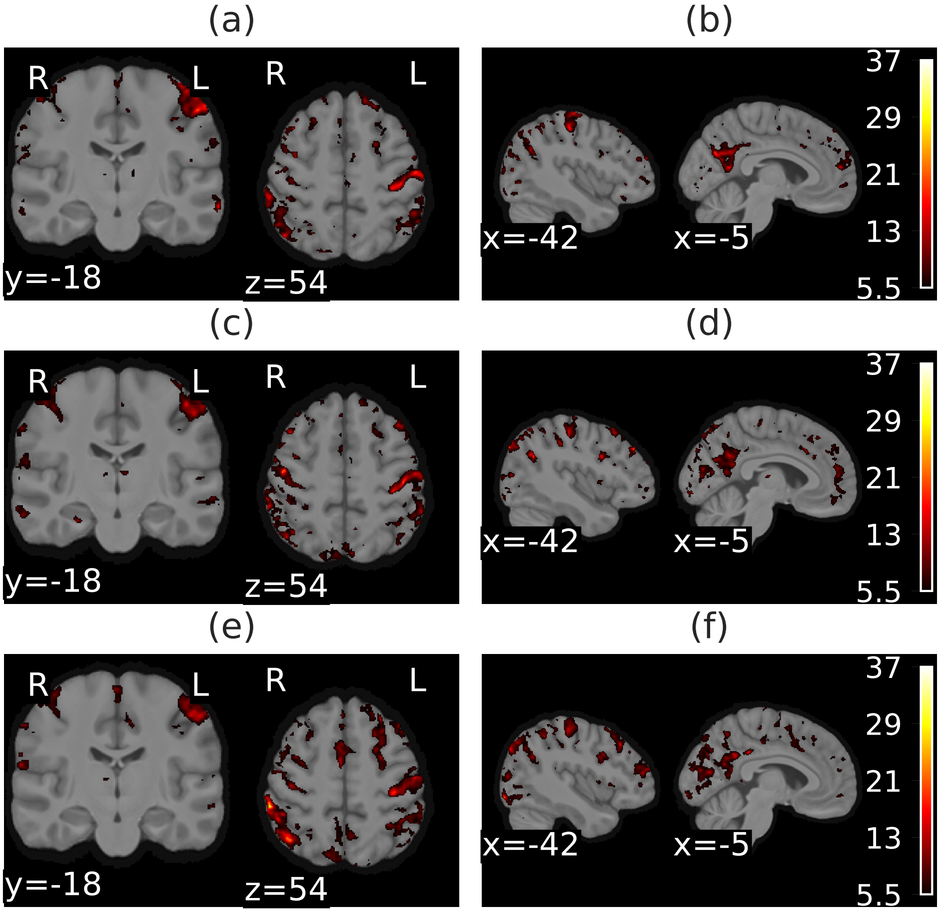

Figure 22. The activation maps signifying statistically significant voxels across the group (Bonferroni corrected p-value < 0.05) obtained during VB index analysis with method 1. The first row (a, b) displays the t-maps from the 1.8^3mm^3 sequence, the second row (b, c) displays the t-maps from the 2^3mm^3 sequence, and the third row (e, f) displays the t-maps from the 2.5^3mm^3 sequence.

4.4 Comparison of activation maps

The activation maps obtained at each sequence were compared quantitatively using the Dice coefficient, which assessed the reproducibility of the results for each data analysis technique across pulse

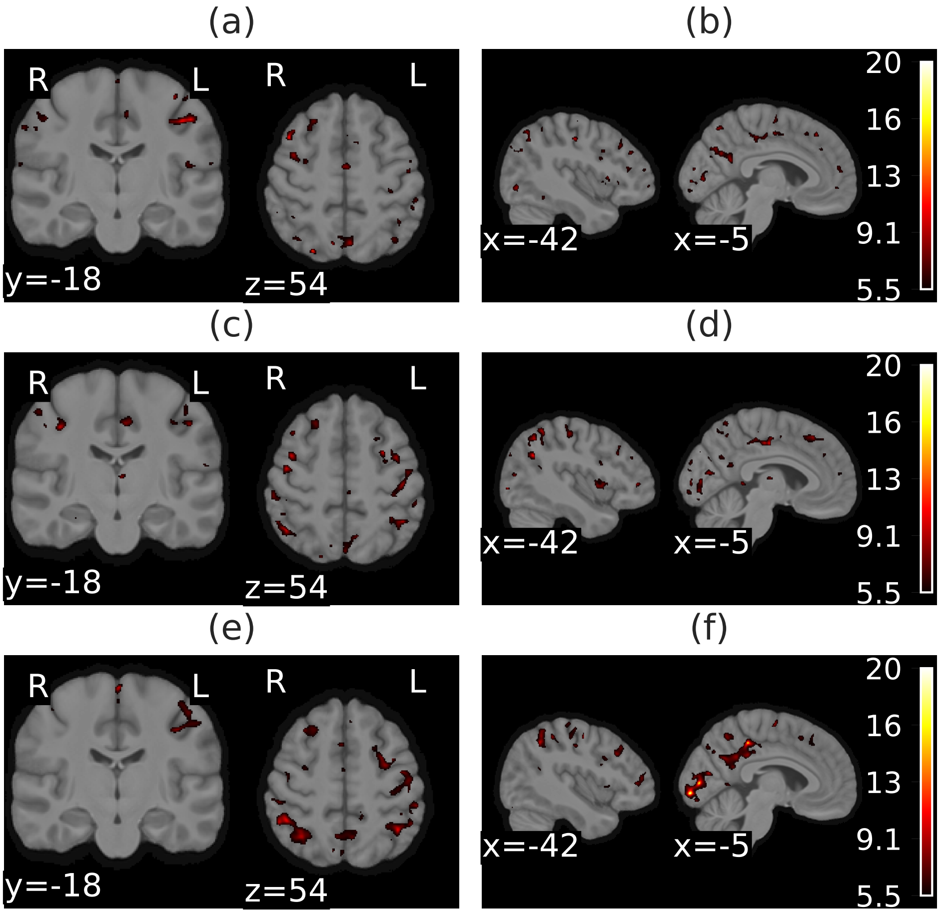

Figure 23. The activation maps signifying statistically significant voxels across the group (Bonferroni corrected p-value < 0.05) obtained during VB index analysis with method 2. The first row (a, b) displays the t-maps from the 1.8^3mm^3 sequence, the second row (b, c) displays the t-maps from the 2^3mm^3 sequence, and the third row (e, f) displays the t-maps from the 2.5^3mm^3 sequence.

sequences. The Dice coefficients obtained when performing pairwise comparison of the different activation maps at each sequence obtained with the GLM analysis are displayed in figure 25a. The Dice coefficients are arrayed in the form of a symmetric matrix. The columns and the rows represent the different activation maps presented in the previous subsection. The columns and rows of the matrix denoted by 1.8, 2.0, and 2.5 refer to the activation maps acquired with the 1.8^3mm^3, 2^3mm^3, and 2.5^3mm^3 pulse sequences respectively. The main diagonal of the matrix shows the Dice coefficients of each activation map compared to itself, which always equal to 1. The matrix is symmetric about the main diagonal. The intersection of the columns and the rows of the matrix represent the Dice coefficient obtained at the two activation maps corresponding to the respective row and column. In addition to this, figure 25b displays the Dice coefficients obtained when performing pairwise comparison of the activation maps obtained with the VB index method 1 across the pulse sequences. Finally, figure 25c displays the Dice coefficients obtained during comparison of the activation maps obtained during VB index

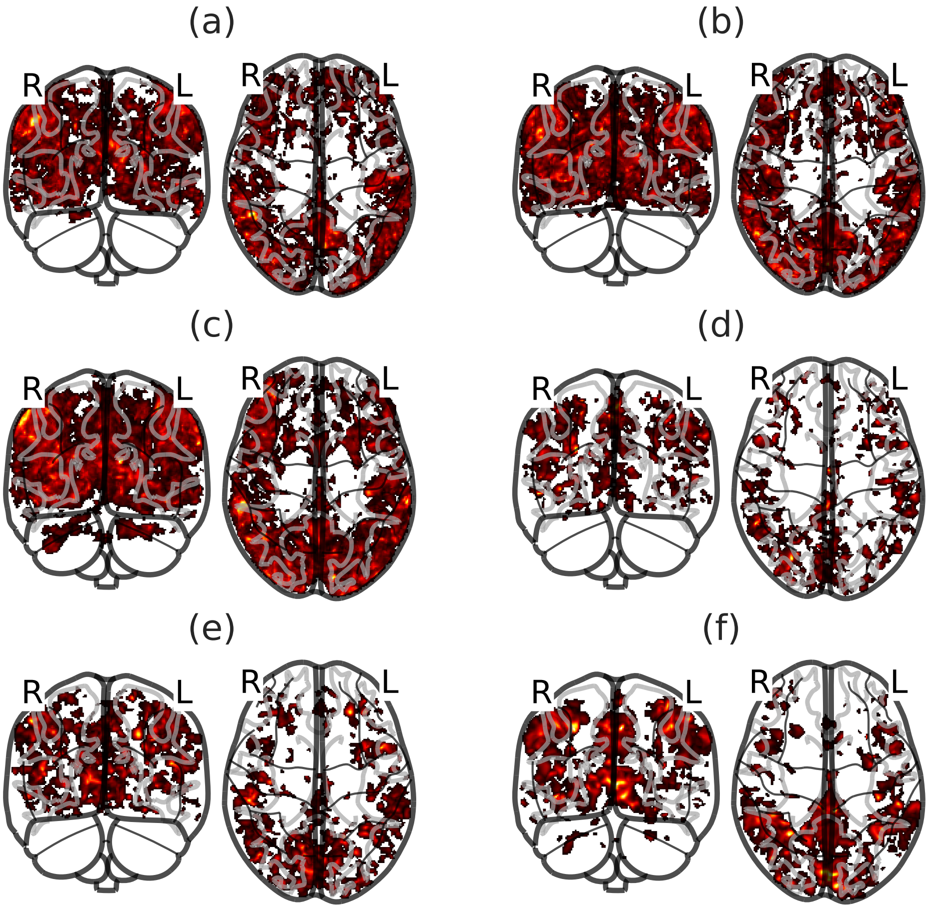

Figure 24. Activation maps obtained with the VB index projected on a transparent rendering of a brain. Figures (a), (b) and (c) represent activation maps obtained with VB method 1 for the 1.8^3mm^3, 2^3mm^3, and 2.5^3mm^3 sequences respectively. Figures (d), (e), and (f) represent the activation maps obtained with the VB method 2 for the 1.8^3mm^3, 2^3mm^3, and 2.5^3mm^3 sequences respectively.

method 2 across the pulse sequences. Overall, the GLM produced higher Dice coefficients compared to the VB index. In addition, VB method 1 had higher Dice coefficients when compared to VB method 2. It is good to point out that confidence intervals were not computed for the Dice coefficients obtained for two reasons. First, the parametric approximation of confidence intervals for the Dice coefficient relies on too many underlying assumptions. Second, in this study, the activation maps were computed using parametric tests (t-tests) based on data from 10 volunteers. Hence, using non-parametric methods such as bootstrapping for estimating confidence intervals entailed that the parametric tests would need to be performed on a reduced sample size, which would violate the assumptions of the parametric methods used. Therefore, it was not feasible within the scope of this study to compute confidence intervals for the Dice coefficient and also for the Overlap coefficient.

A cross-comparison between the activation maps of the GLM and the VB index was also performed across each sequence. This was achieved with the overlap coefficient which assessed the congruence of the VB activation maps to the GLM activation maps. Comparison of the VB activation maps acquired for each approach to the GLM was performed across all the sequences tested. Figures 26 shows the resulting overlap coefficients obtained, presented in a similar configuration as the Dice coefficients. Figure 26a displays the overlap coefficients, comparing the activation maps obtained at each sequence with the VB method 1 to the GLM. Alternatively, 26b displays the overlap coefficients, comparing the activation maps obtained at each sequence with the VB method 2 to the GLM. In general, the activation maps of the VB method 1 exhibited larger overlap with the GLM. Finally, the total number of statistically significant voxels for each activation map was determined at each sequence and is given in figure 27. The activation maps acquired with the VB index had overall a higher number of statistically significant voxels compared to the GLM by approximately an order of magnitude. The VB method 1 had larger numbers of statistically significant voxels compared to VB method 2. Across all data analysis approaches, the number of statistically significant voxels was higher at poorer resolution.

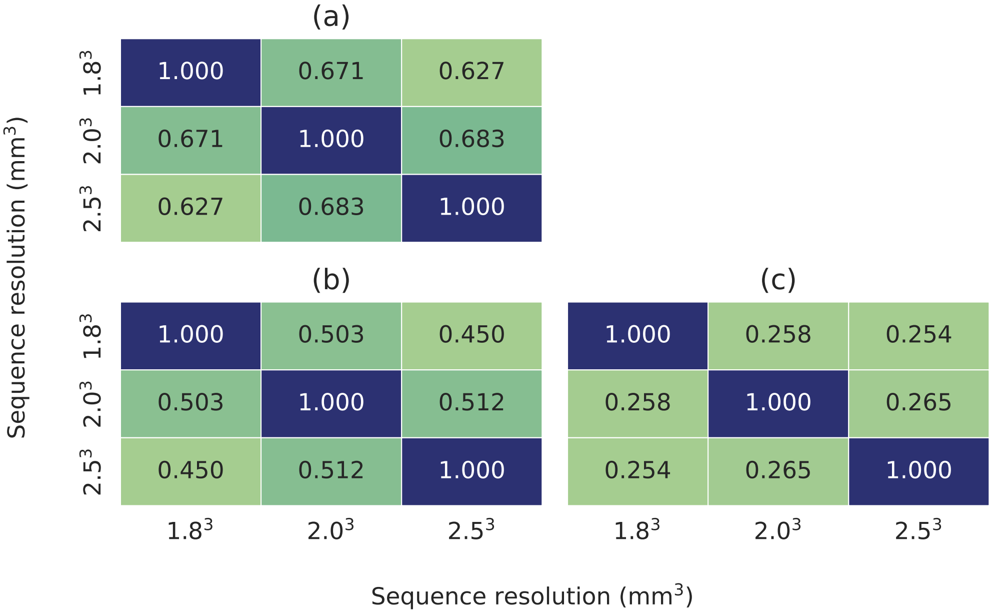

Figure 25. The Dice coefficients obtained when comparing the activation maps obtained with the GLM (a), VB method 1 (b), and VB method 2 (c) across pulse sequences.

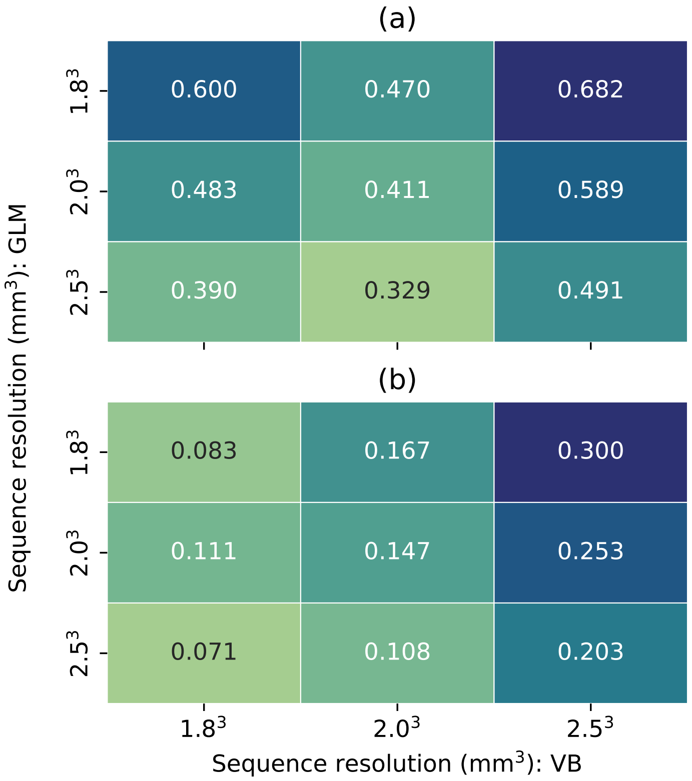

Figure 26. The overlap coefficients obtained when comparing the activation maps of the VB method 1 with the GLM (a), and the VB method 2 with the GLM (b).

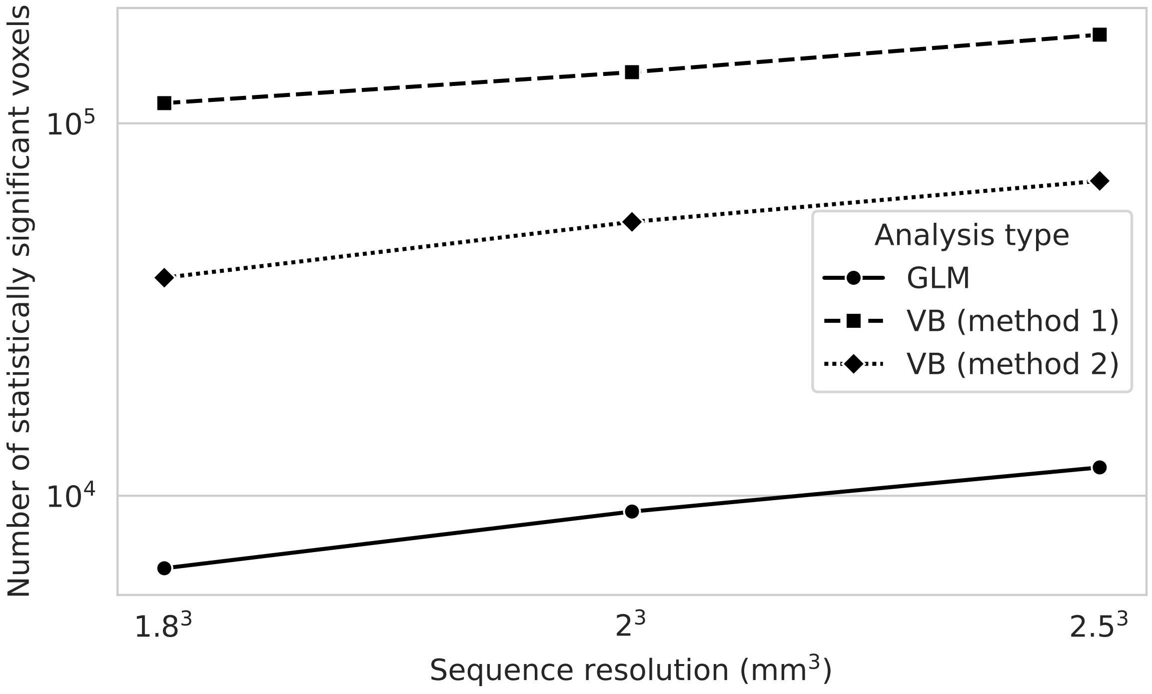

Figure 27. The number of statistically significant voxels across pulse sequence for each data analysis technique. The y-axis is scaled logarithmically.

5 Discussion

5.1 Introduction

The aim of the study was to investigate functional activation using task based fMRI across pulse sequences with different scanning parameters. The study was motivated by the fact that the VB index, a data-driven fMRI data analysis technique, has not yet been rigorously tested across pulse sequences. Therefore, three different pulse sequences with approximately identical scanning parameters except for the voxel volume were used. The first pulse sequence featured the larger voxel volume employed in a typical fMRI study of 2.5^3mm^3. Subsequent sequences employed voxels of volume 2^3mm^3 and 1.8^3mm^3, representing an approximately 49% and 63% reduction in voxel volume respectively from the 2.5^3mm^3 sequence. A total of 10 research volunteers were recruited, scanned and the fMRI data was preprocessed and analysed with the VB index and the traditional GLM which served as a baseline.

5.2 Discussion

5.2.1 Image quality

The study investigated the effect spatial resolution has on functional activation analysis with the VB index. Spatial resolution was chosen as the scanning parameter in question when investigating the VB index across sequences due to two main reasons. Firstly, spatial resolution directly affects the susceptibility of the fMRI study to the PVE. In other words, larger voxels are at an increased risk of being partially filled by both neuronally active tissue and non-active tissue obscuring the BOLD signal detected (Du et al., 2014). Secondly, despite the theoretical benefits of higher spatial resolution, fMRI studies generally make use of large voxels ($\geq 2.5^3$mm^3) as observed previously in table 1. This is likely because single-shot EPI sequences, commonly used in fMRI, prioritise fast data acquisition over high spatial resolution (Jezzard & Clare, 1999). Furthermore, the benefits of higher spatial resolution are countered by the reduction in both the SNR and TSNR (Triantafyllou et al., 2005) which may affect the ability to detect the small signal fluctuations arising due to the BOLD effect (Welvaert & Rosseel, 2013). Indeed, the comparison of image quality across the sequences performed in this study revealed a statistically significant reduction in the TSNR and SNR between the 2.5^3mm^3 sequence and both of the higher resolution 2^3mm^3 and 1.8^3mm^3 sequences. The substantially large number of MRI volumes (393) acquired per fMRI run in this study could have alleviated the impact of the significant TSNR reduction. In fact, Murphy et al. (2007) demonstrated that a TSNR of at least 10 would be required with 400 fMRI volumes to detect the BOLD signal (p-value=0.05) at 5% contrast relative to the baseline MRI signal. Interpolating this value linearly to the typical 4% BOLD contrast at 3T (van der Zwaag et al., 2009) would entail that a TSNR of approximately 20 would be required for adequate BOLD signal detection, which is lower than the lowest TSNR observed in this study of 31.680 $\pm$ 2.548 for the 1.8^{3}mm^3 sequence. This is important for future work since it implies that the number of fMRI volumes (and hence scanning time) particularly for the poorer 2.5^{3}mm^3 resolution sequence could be reduced without warranting a significant reduction in detection power.

5.2.2 Volunteer study

A cohort of 10 research volunteers were recruited and scanned while performing sequential finger tapping tasks with the three separate pulse sequences employing different voxel volumes. The volunteer's fMRI data was first preprocessed to correct for artefacts present, and then analysed using two separate approaches; the standard model-based approach via the GLM, and VB index which has not been rigorously tested across pulse sequences.

The GLM analysis featured the creation of a design matrix which contained the experimental regressors i.e., the task and rest conditions, and confound regressors. Then, a mass-univariate one-sample t-test was applied on the fMRI data of each volunteer separately to assess the statistical significance between the task and rest regressors. The analysis featured a first-level smoothing operation with a smoothing FWHM (4.806 mm) that was constant across the pulse sequences. The first-level statistical maps obtained were normalised to MNI space, and a second-level one-sample t-test determined which voxels exhibited statistically significant differences between the task and rest conditions at a group level. The statistical maps obtained were thresholded with Bonferroni correction to include only voxels with a level of significance of 0.05 in the resulting activation maps.

The GLM activation maps obtained at each sequence are given by figure 20. The activation maps revealed clusters of statistically significant voxels predominantly in the left portion of the cerebral cortex across the pulse sequences. The contralateral nature of motor cortical activation was in agreement with the results of Gountouna et al. (2010) illustrated in figure 17 and with the results of other literature (Turesky et al., 2018; Witt et al., 2008; Wüthrich et al., 2023). The transverse slices of the activation maps given by figures 20a, 20c, and 20d, for the 1.8^{3}mm^3, 2^{3}mm^3 and 2.5^{3}mm^3 sequences respectively revealed that much of the "hand knob" region of the motor cortex was statistically significant. The detection of functional activation in the "hand knob" region highlighted in figure 18 was of primary interest for this study, since it is responsible for hand motor function (Pimentel et al., 2011) through it's outputs to the pyramidal tract (Khushu et al., 2001). The coronal slices in figures 20a, 20c, and 20d, and the sagittal slices seen in figures 20a, 20c, and 20d for the 1.8^3mm^3, 2^3mm^3 and 2.5^3mm^3 sequences respectively showed the functional activation detected in the "hand knob" region from a different perspective. Overall, the results obtained in the motor cortex were consistent across pulse sequences, and with the results of literature (Gountouna et al., 2010; Turesky et al., 2018; Witt et al., 2008; Wüthrich et al., 2023).

The activation maps were projected on transparent "glass-like" brains to allow a better visualisation of portions of the activation maps not captured by the previously discussed slices. The three glass-brain projections corresponding to the 1.8^3mm^3, 2^3mm^3 and 2.5^3mm^3 sequences are given by figures 21a, 21b and 21c respectively. Apart from functional activation in the motor cortex, these projections also demonstrate that functional activation was detected across the sequences bilaterally in the occipital lobe which sits at the back of the head, and is responsible for visual perception (Queensland-Government, 2022). In general, functional activation in the occipital lobe was consistent across the pulse sequences. However, the area of activation in the occipital lobe for the 1.8^3mm^3 sequence was smaller compared to that observed for the poor resolution sequence. Apart from this, clusters of functional activation were detected for the 2.5^3mm^3 sequence in the cerebellum, and the thalamus in agreement with literature (Gountouna et al., 2010; Turesky et al., 2018). Cerebellar activity was not detected for the 1.8^3mm^3 and 2^3mm^3 sequences, which is mainly because the FOV did not cover the cerebellum (at least not fully) since further expansion of the FOV necessitated an increase in the number of slices and hence the TR.

The results obtained with the GLM served a baseline for comparison using the VB index (Bajada et al., 2020), a data-driven approach that has not yet been tested across pulse sequences, which motivated the study. The functional activation analysis performed with the VB index featured the application of a denoising algorithm on the fMRI data and a VB analysis that consisted of two separate approaches. The first approach (VB method 1) aimed to replicate the smoothing operations performed during GLM analysis to provide as fair a comparison as possible to the GLM. Consequently, the denoised data was smoothened before the application of the VB analysis. In the second approach (VB method 2), the VB analysis was performed first and the resulting VB maps were smoothened. These two separate VB approaches were performed for two reasons. Firstly, the VB method 1 was conducted to reproduce the style of the GLM analysis. Therefore, the results obtained with the VB method 1 aimed to validate the VB index across pulse sequences with the GLM. On the other hand, the VB method 2 was performed mainly due to the intrinsic operation of the VB index. As discussed in the literature review, the VB index is an algorithm that detects the edges between functionally distinct regions (Farrugia et al., 2024). Since spatial smoothing effectively blurs the data (Jahn, 2019), using the VB index prior to spatial smoothing may not be the optimal approach, as the edges between functionally distinct regions will consequently also be blurred out due to the smoothing. Instead, performing the VB analysis on the raw data ensures that the edge contrast of the original data is preserved. In the VB method 2, smoothing is performed on the VB maps after VB analysis to account for the fact that even after spatial normalisation to a common space, the anatomical position of functional activation is subject dependent and will vary (even if slightly) across participants (Alahmadi, 2021). Smoothing in the second-level for the VB method 2 was thus a necessary step in order to get meaningful statistically significant results. In both VB approaches, the VB maps were normalised to a common MNI space. Then, a one-sample t-test was applied to the VB maps at each sequence to determine which voxels had a VB index that was statistically higher than the median VB index across the group. Bonferroni correction was applied to threshold the resulting statistical maps and include voxels with a level of significance of 0.05 in the resulting VB activation maps.

Slices from the VB activation maps at each sequence acquired using the VB method 1 are given in figure 22. The transverse slices obtained from the VB activation maps using VB method 1 with the 1.8^3mm^3, 2^3mm^3 and 2.5^3mm^3 sequences given by figures 22a, 22c, and 22e respectively revealed that statistically significant functional activation was detected in the “hand knob” region of the motor cortex highlighted previously in figure 18. A subjective comparison of the VB activation maps of figure 22 with those of the GLM in figure 20 revealed high conformance in the “hand knob” region. An alternate view of the “hand knob” region is provided in the coronal slices of figures 20a, 20c, and 20e and the left sagittal slice of figures 20b, 20d, and 20e. These slices showed functional activation was detected in the “hand knob” region consistently across pulse sequences in conformance with the GLM.

The VB analysis was also performed with a second approach that performed smoothing after processing the data with the VB index to preserve edge contrast between functionally distinct regions. Figure 23 displays the resulting VB activation maps obtained with the VB method 2. Figure 23 showed that functional activation was detected in the “hand knob” region with VB method 2 across the pulse sequences. However, compared to the GLM activation maps and the VB method 1 activation maps whereby most of the “hand knob” region and other parts of the motor cortex were labelled as statistically significant, only portions of the “hand knob” were labelled as statistically significant during the VB analysis with method 2. This can be clearly seen by the transverse slices of figures 23a, 23b, and 23c corresponding to the 1.8^3mm^3, 2^3mm^3 and 2.5^3mm^3 sequences respectively which show “hand knob” activation localised to a smaller area compared to those seen previously in figures 20 and 22 for the GLM and VB method 1 respectively. Similarly, the coronal slices of figures 22a, 22c, and 22e and the left sagittal slice of figures 22b, 22d, and 22f corresponding to the VB method 2 activation maps for the 1.8^{3}mm^3, 2^{3}mm^3 and 2.5^{3}mm^3 sequences respectively also showed that statistically significant clusters of voxels were localised to a specific portion of the “hand knob” region.

The VB activation maps obtained with both VB approaches revealed statistically significant regions in the occipital lobe. These statistically significant occipital regions may be visualised by the right sagittal slice of the activation maps in figures 22 and 23 for the VB method 1 and VB method 2 respectively. As observed in the “hand knob” region, the VB method 1 exhibited larger clusters in the occipital region when compared to the VB method 2. These observations were valid across the pulse sequences. Apart from this, the VB activation maps obtained with both VB approaches also revealed statistically significant clusters of voxels were detected in the Cerebellum with the 2.5^{3}mm^3 sequence. These clusters may be observed by the glass-brain projections of figures 24c and 24f corresponding to the 2.5^{3}mm^3 sequences obtained with the VB method 1 and VB method 2 respectively. Both of these observations conformed with the results of the GLM.

The glass brain projections of the activation maps obtained with the VB index in both approaches seen in figure 24 revealed clearly that functional activation with the VB index was not predominantly limited to the motor cortex and the occipital lobe but also included a variety of other brain regions. Conversely, the glass-brain projections acquired with the GLM in figure 21 revealed that functional activation detected with the GLM was predominantly limited to the motor cortex and the occipital lobe, irrespective of the pulse sequence used.

These observations may be explained by discussing the inherent limitations of the GLM approach. A crucial component in the GLM analysis is the design matrix, composed of a weighted set of user-specified regressors that define the model and are used to explain the time-series signal for each voxel (Leibovici & Smith, 2001). Embedded in the design matrix are the experimental regressors which model the BOLD response to the experimental condition (i.e., task-related signal time courses) (Jenkinson et al., 2017). The experimental regressors in the GLM are often modelled by convolving the HRF with the experimental condition of the experiment obtaining the expected BOLD time-series in a neuronally active voxel. Consequently, one of the limitations of the GLM is that it assumes that the data may be analysed using an HRF that is constant across brain regions and subjects (Morante et al., 2021). Previous work had demonstrated the HRF has shown significant inter-subject variation violating this assumption (Aguirre et al., 1998; Handwerker et al., 2004). Furthermore, the shape of the HRF has also been shown to vary across different brain regions within a subject (Miezin et al., 2000). These variations in the HRF are a consequence of several factors including inter-subject and intra-subject differences in neural activity, vasculature, and respiration amongst others (Handwerker et al., 2004). One approach to address these limitations includes expanding the design matrix to include additional regressors that account for these variations in the HRF. This includes expanding the HRF by adding its temporal derivatives to the design matrix to account for slight temporal shifts (Poline & Brett, 2012). Alternatively, the HRF may be modelled as a linear combination of a constrained set of basis functions. The experimental regressor may then be modelled by convolving the experimental paradigm with the basis functions to create a set of experimental regressors (Poldrack et al., 2011). In this study, the experimental regressor used was composed of a single HRF which limited the detection power of the GLM model used (Aguirre et al., 1998) and could have been one of the reasons as to why functional activation detection was mainly limited to the motor cortex and the occipital lobe. More robust GLM studies should incorporate more complex experimental regressors to better account for inter-subject and intra-subject variations. In any case, regardless of the complexity of the experimental regressors used, this concept highlights the fact that the detection power of the GLM is reliant on a user-specified design matrix. The VB index due to its data-driven nature was not constrained by this limitation, which could have been the reason why the functional activation detected by the VB index was more expansive. It is good to point out that the statistical analysis performed with the VB in both approaches was by no means optimal. In both approaches, the voxel-wise one-sample t-test performed assessed whether voxels had a VB index that was statistically higher than the median VB index across the group. Another approach would incorporate a control group such as rest-state fMRI data acquired from a group of participants to act as a benchmark. Then statistical testing may be performed between the experiment group from which task-based fMRI data was acquired and the control group.

Nevertheless, the initial subjective comparison between the GLM and VB index revealed that the VB method 1 produced reproducible results across the pulse sequences tested in the motor cortex in conformance with the GLM. Furthermore, the VB method 2 also reproducibly revealed contralateral motor cortical activation across the pulse sequences. However, as opposed to the GLM and VB method 1 whereby most of the motor cortex was statistically significant, motor cortical activation in the VB method 2 was localised to a specific portion. This is not necessarily a poor result since the smoothing approach of VB method 2 differed from the others. Furthermore, somatotopic evaluations of finger tapping tasks with fMRI did reveal that functional activation due to index and thumb movements were localised to specific anatomical portions of the primary motor cortex as opposed to being smeared across the entire motor cortex (Lotze et al., 2000).

The VB method 2 applied the VB index on unsmoothened data, which meant that the edge contrast between functionally distinct regions were not blurred out. Since the VB index is an edge detection algorithm, this process could have improved the accuracy by which the edges between functionally distinct regions were detected and hence by which neuronal activity was localised. Smoothing was then performed at a second level to account for inter-subject anatomical differences. This could explain why only portions of the “hand knob” region were labelled as active as seen in figure 23. This effect was observed across sequences but primarily in the higher 1.8^3mm^3 and 2^3mm^3 resolution sequences, which may be due to less PVE that amplified edge contrast. On the contrary, the smoothing applied to the denoised data in VB method 1 blurred out the edges of functionally distinct regions, which could have caused the VB index to label the motor cortex as one large conjoined cluster as was seen with the GLM. These hypotheses would favour the use of VB index method 2 where edge detection accuracy is of primary importance, such as in somatotopic studies, but VB index method 1 when conformance with more established data analysis techniques such as GLM is required.

The VB analysis in both approaches detected functional activation in areas that were not detected during the GLM analysis. One of these regions includes the thalamus, which is responsible for relaying motor activity from the basal ganglia and cerebellum to the motor cortex (Sommer, 2003). The thalamic activity was detected across the pulse sequences with VB method 1 as seen by the coronal and right sagittal slice of figure 22. Furthermore, thalamic activity was also detected with VB method 2 sequence as seen from the coronal and right sagittal slice of figures 23c and 23d respectively for the 2^3mm^3 sequence. Thalamic activity was also detected with the VB method 2 for the other sequences but are not present in the particular slices presented in figures 23. The thalamic activity detected by the VB index in both approaches was in agreement with literature (Turesky et al., 2018; Witt et al., 2008; Wüthrich et al., 2023). In addition to this, functional activation was detected with the VB index in both approaches across the pulse sequences in brain areas lying directly anterior to the hand knob region corresponding to the premotor and supplementary motor areas in agreement with literature (Gountouna et al., 2010; Turesky et al., 2018; Witt et al., 2008; Wüthrich et al., 2023). The premotor area plays an important role in guiding movement in response to sensory information (Buccino et al., 2001). Alternatively, the supplementary motor area is responsible for initiating and sequencing motor tasks (Khushu et al., 2001). The VB analysis also detected functional activation in the area situated directly posterior to the motor cortex known collectively as the parietal lobe which is responsible for decision-making, spatial awareness and speech comprehension amongst others (Bisley & Goldberg, 2010). Functional activation was detected in the parietal lobe with both VB approaches and across the pulse sequences tested. As in the previous cases, the parietal activation detected with the VB method 1 was larger in area compared to those of the VB method 2 which could be a consequence of the first-level smoothing performed that reduced the edge contrast compared to VB method 2. The transverse slice of figures 22 and 23 for the VB method 1 and 2 respectively, revealed that functional activation detected by the VB index in the parietal lobe was predominantly bilateral. In addition to this, the sagittal slices showed that parietal activation was detected with the VB index in both the superior and inferior parietal lobules. These observations were observed in both VB approaches and across pulse sequences. Finally, the VB activation maps in both approaches revealed functional activation in the prefrontal cortex, which is responsible for higher cognitive tasks (Henri-Bhargava et al., 2018).

5.2.3 Quantitative comparison of activation maps

The activation maps obtained with the GLM and the two VB approaches were compared quantitatively together across pulse sequences using the Dice coefficient to evaluate the reproducibility of functional activation results across the pulse sequences for each data analysis technique. Furthermore, the conformity of the VB index to the GLM was assessed with the Overlap coefficient. The level of similarity between two activation maps were benchmarked based on the size of Dice coefficient or Overlap coefficient. The ranges specified by Wilson et al. (2017) will be used to describe similarity between two activation maps. The spatial similarity of a pair of activation maps will be described as being low if their similarity metric is within: 0.00 to 0.19, low-moderate: 0.20 to 0.39, moderate: 0.40 to 0.59, moderate-high: 0.60 to 0.79 or high: 0.80 to 1.00.

5.2.4 Reproducibility across pulse sequences

The activation maps obtained using the GLM across the pulse sequences were compared together using the Dice coefficient, which are displayed in figure 25a. Overall, the Dice coefficients obtained with the GLM across pulse sequences were moderately-high ($\approx$0.6-0.7) which suggested reproducible results across the sequences tested as observed in the subjective comparison. The lowest spatial similarity was between the GLM activation maps acquired with the 1.8^3mm^3 and 2.5^3mm^3 sequences, with a Dice coefficient of 0.627. Alternatively, the greatest spatial similarity was exhibited between the GLM activation maps acquired with the 2^3mm^3 and 2.5^3mm^3 sequences, having a Dice coefficient of 0.683. Figure 27 demonstrated that the activation maps obtained with poorer resolution had a larger number of statistically significant voxels compared to the higher resolution sequences. This may be partially attributed to the fact that cerebellar activity was detected with the 2.5^3mm^3 sequence but not with the higher resolution sequences. Furthermore, larger areas of functional activation were detected in the occipital lobe for the 2^3mm^3 and 2.5^3mm^3 sequences compared to the 1.8^3mm^3 sequence. These observations would explain why the greatest dissimilarity was observed between the 1.8^3mm^3 and 2.5^3mm^3 sequences, while the greatest spatial similarity was observed between the 2^3mm^3 and 2.5^3mm^3 sequences.

One parameter which could have introduced some bias in the quantitative comparisons is intrinsic smoothing. As a consequence of the PVE, the fMRI data acquired from the scanner has some intrinsic smoothing (Harri et al., 2007). The PVE is more significant at poorer resolution, meaning that the level of intrinsic smoothing is higher at poorer resolution. In the study, constant smoothing was applied during the data analysis. Since the fMRI data acquired with the three pulse sequences had different degree of intrinsic smoothing, the net result was that the poorer resolution sequence had higher net smoothing. This could have contributed partially to the larger number of statistically significant voxels detected with the poorer resolution sequences, as seen in figure 27. Consequently, the Dice coefficient may have been penalised due to differences in the size of the activation maps, which could be partially attributed to the varying degree of net smoothing. Ideally, as suggested by Weibull et al. (2008) and Molloy et al. (2014) if higher spatial specificity is not required, higher smoothing should be applied to higher resolution data to account for lower intrinsic smoothing.

The Dice coefficients obtained for the VB index method 1 provided in figure 25b, were moderate in value ($\approx$0.5) and were lower than those seen in the GLM, suggesting lower reproducibility across sequences. The highest spatial similarity for the VB method 1 was observed between the activation maps of the 2^3mm^3 and 2.5^3mm^3 sequences, with a Dice coefficient of 0.512. The greatest dissimilarity was observed between the activation maps of the 1.8^3mm^3 and 2.5^3mm^3 sequences, having a Dice coefficient of 0.450.

On the other hand, the Dice coefficients obtained with the VB method 2 are given in figure 25c. Overall, the Dice coefficients for the VB index method 2 were within the low-moderate range ($\approx$0.25) and were lower than those obtained with both the GLM and VB method 1. This meant that the results of VB method 2 were less reproducible across pulse sequences compared to both the GLM and VB method 1. As with the GLM and VB method 1, the highest spatial similarity for the VB method 2 activation maps were exhibited between the activation maps acquired with the 2^3mm^3 and 2.5^3mm^3 sequences, having a Dice coefficient of 0.265. Furthermore, the greatest dissimilarity was exhibited between the activation maps acquired with the 1.8^3mm^3 and 2.5^3mm^3 sequences, having a Dice coefficient of 0.254.

5.2.5 Conformance of the Vogt-Bailey Index with the General Linear Model

The conformance of the VB results with the GLM was assessed using the Overlap coefficient. The initial subjective comparison performed earlier revealed that the VB method 1 exhibited the highest conformance to the GLM, while the VB method 2 exhibited more localised functional activation when compared to the GLM. Figure 26a provides the overlap coefficients quantifying the overlap between the

GLM and the VB method 1, and figure 26b provides the overlap coefficients quantifying the overlap between the GLM and the VB method 2. The results revealed that indeed the VB method 1 exhibited the highest overlap with the GLM activation maps, in agreement with the subjective comparison.

In general, as seen in figure 26a, the overlap between the VB method 1 and the GLM was moderate to moderate-high (0.4 to 0.7). The VB method 1 activation map acquired with the 2.5^3mm^3 sequence exhibited the highest overall overlap with the GLM across pulse sequences. The highest overlap (0.682) was between the GLM activation map obtained with the 1.8^3mm^3 sequence and the VB method 1 activation map obtained with the 2.5^3mm^3 sequence. Conversely, the lowest overlap (0.329) was exhibited between the GLM activation map obtained with the 2.5^3mm^3 sequence and the VB method 1 activation map acquired with the 2^3mm^3 sequence.

Alternatively, figure 26b demonstrated that, in general, the overlap between the GLM and the VB method 2 was in the low to low-moderate range ($\approx$ 0.1 to 0.3), signifying that the VB method 2 was the least conformal to the GLM. The highest overlap (0.300) was exhibited between the GLM activation map obtained with the 1.8^3mm^3 sequence and the VB method 2 activation maps obtained with the 2.5^3mm^3 sequence. In general, the VB method 2 activation maps acquired using the higher resolution sequences exhibited smaller overlap with the GLM. In both VB approaches, the highest conformance with the GLM was exhibited with the 2.5^3mm^3 sequence. This could be a consequence of the higher amount of intrinsic smoothing due to poorer resolution, which swelled the statistically significant clusters detected in the motor cortex.

5.3 Conclusion

The study aimed to assess functional activation with the VB index across pulse sequences. To achieve the aim, the study developed 3 fMRI pulse sequences with distinct voxel volumes, and applied the pulse sequences on a cohort of 10 volunteers. Then, the data was analysed with the VB index, and with the GLM which served as the baseline. The results obtained with both techniques were compared qualitatively with literature, quantitatively across pulse sequences with the Dice coefficient, and quantitatively together with the Overlap coefficient. Consistent functional activation maps were produced across the pulse sequences with GLM and the VB method 1. The activation maps obtained with the VB method 2 were less consistent across the pulse sequences. Overall, the results obtained with the VB index method 1 which saw the VB being applied on smoothened data conformed well with the GLM. The results of the VB index method 2 were less conformal to the GLM, as functional activation results were more spatially localised. The more localised activation detected with the VB index method 2 could be because the intrinsic functional edge contrast of the raw data was preserved since the VB index was applied on unsmoothened data. In both VB index approaches, the highest overall conformance with the GLM was obtained with the 2.5^3mm^3 sequence. In both approaches, the VB index detected functional activation in areas not detected by the GLM, which could be due to the intrinsic limitations of the GLM approach that relies on a user-specified design matrix. This chapter discussed the results obtained in the study, and the next chapter will summarise the conclusions, and provide some recommendations for professional practise and future work.

6 Conclusions and recommendations

6.1 Introduction

The study investigated functional activation analysis in BOLD fMRI with three separate pulse sequence employing voxel volumes of 1.8^3mm^3, 2^3mm^3, 2.5^3mm^3 respectively. The motive of the study was to test a data-driven algorithm, the VB index across pulse sequences and benchmark the results with the GLM, an established fMRI data analysis technique. A cohort of 10 research volunteers were recruited and scanned with the three fMRI sequences. The data was analysed with the GLM which served as the baseline, and then with the VB index using two separate VB index methods. The first VB approach saw the application of the VB index on smoothened fMRI data as was performed with the GLM to allow as fair a comparison. The second VB approach featured the application of the VB index on the raw fMRI data to preserve the functional edge contrast, and smoothing was applied on the resulting VB index maps. The resulting activation maps were compared across pulse sequences qualitatively with literature and quantitatively using the Dice coefficient and the Overlap coefficient.

6.2 Summary of conclusions from the study

The main conclusions that emerged from the study were:

1. Significant reductions in the TSNR were observed between the 2.5^3mm^3, 2.0^3mm^3, and 1.8^3mm^3 sequences, corresponding to 63% and 49% reductions in voxel volumes. Alternatively, significant reductions in the SNR were observed between the 2.5^3mm^3 sequence and the two other sequences, but not between the 2.0^3mm^3 and the 1.8^3mm^3 sequences. Despite these significant reductions, the large number of fMRI volumes acquired ensured that the TSNR values across the pulse sequences remained within the baseline TSNR values suggested by Murphy et al. (2007) for adequate detection power.
2. The GLM analysis consistently detected functional activation across all three pulse sequences in the “hand knob” region of the motor cortex and the occipital lobe. For the 2.5^3mm^3 resolution sequence, thalamic and cerebellar activity was detected with the GLM but not with the higher resolution sequences. However, the latter was probably due to the fact that the FOV in the higher resolution sequences did not cover the entirety of the cerebellum.
3. The VB index methods (1 and 2) consistently detected functional activation in the “hand knob”

region of the motor cortex and the occipital lobe as with the GLM. Apart from this, both VB index methods detected functional activation consistently across pulse sequences in areas not detected by the GLM including the parietal lobe, the prefrontal, the premotor, and supplementary motor areas, in conformance with literature.

4. The GLM had the highest reproducibility of results across pulse sequences with moderately-high Dice coefficients (0.6 to 0.7). The VB method 1 had moderate reproducibility of results across pulse sequences with Dice coefficients in the order of 0.5. On the other hand, the VB method 2 had the lowest reproducibility of results across pulse sequences with low-moderate Dice coefficients ($\approx$0.25).
5. In general, the results of the VB method 1 showed good conformance with the GLM, with overlap coefficients ranging from moderate to moderately-high (0.4 to 0.7). The 2.5^{3}mm^3 sequence, in particular, exhibited the highest conformance between the VB method 1 and GLM activation maps.
6. The VB method 2 showed overall less conformance with the GLM, exhibiting low to low-moderate Overlap coefficients. However, the different smoothing approach employed in the VB method 2 to preserve edge contrast meant that this technique was not directly comparable to the GLM. As with the VB method 1, the VB method 2 activation map obtained with the 2.5^{3}mm^3 sequence was most conformal to the results of the GLM, with low-moderate Overlap coefficients (0.2 to 0.3). The higher conformance observed with the 2.5^{3}mm^3 sequence may result from the higher intrinsic smoothing present at lower resolution.

6.3 Recommendations for professional practice

The following are recommendations for professional medical physics practice:

1. The TSNR values obtained, particularly with the 2.5^{3}mm^3 sequence were high and exceeded the recommended baseline values suggested by Murphy et al. (2007). Consequently, fMRI scanning sessions utilising particularly the 2.5^{3}mm^3 sequence could be shortened to reduce scanning times without warranting a significant reduction in BOLD signal detection power.
2. If conformity with the GLM is required during VB index analysis, the VB index method 1 may be used, i.e., the VB analysis may be applied on spatially smoothened fMRI data. Furthermore, the 2.5^{3}mm^3 sequence may be used in conjunction with the VB index method 1 to enhance conformity with the GLM.

3. For a somatotopic evaluation of functional activation with the VB index, the VB method 2 should be used to preserve the original functional edge contrast of the fMRI data. In this case, the VB index may be applied on unsmoothened to preserve the functional edge contrast of the fMRI data. The usage of the higher resolution 1.8^{3}mm^3 and 2^{3}mm^3 sequences in this case may be more appropriate as the subjective comparison did not reveal reductions in the detection power at high resolution in the “expected” areas such as the motor cortex and the occipital lobe, and also in areas not identified by the GLM. If somatotopic analysis with the VB index is employed but higher conformance with the GLM is required, then the 2.5^{3}mm^3 sequence should be used. However, further validation of both methods across a wider cohort of volunteers is required to ensure the generalisability of the results.

6.4 Recommendations for future research

Suggestions for further research are:

1. The study performed a group level statistical analysis with the VB index by statistically comparing the VB index of each voxel to the median VB index at a group level. Ideally, a control group composed of rest-state fMRI data from a group of participants is incorporated as a benchmark. Future work is needed to validate the results obtained with the VB index by incorporating a control group and statistically comparing the VB indices between the experiment and the control group.
2. The results obtained with the VB index in both methods revealed functional activation in a wide variety of brain regions that were not detected by the GLM. Future work is needed to study how correlated the fMRI signal of brain regions which are predominantly involved in hand motor function such as the “hand knob” are to these auxiliary regions. This could help in providing more explainability as to why model-based methods may not be able to detect functional activation in these regions, and also help to further explain the function these regions have in relation to the neural mechanisms of the underlying brain function.
3. A total of 10 research volunteers were recruited for the study. Ideally, the results from the study should be validated across a larger cohort of volunteers. Larger cohorts may be important to allow detection of subtle effects that may not be readily apparent in smaller cohorts.

6.5 Conclusion

The study achieved its aim and objectives by developing 3 separate fMRI pulse sequences with distinct voxel volumes, and applying the pulse sequences on a cohort of 10 volunteers. Image quality at each sequence was assessed with the SNR and the TSNR. The data was analysed with a conventional model-based technique that served as a baseline and with the VB index in two separate approaches. The resulting activation maps were compared qualitatively with literature, and quantitatively together across sequences. The results showed that the results of the GLM and the VB method 1 exhibited moderate to moderately high reproducibility across pulse sequences. However, the VB method 2 exhibited less reproducibility across sequences. Furthermore, the results obtained with the VB index method 1 conformed well with the results of the GLM, particularly at poorer resolution. The VB method 2 showed less conformance with the GLM, which could be due to the different smoothing approach employed.

References

Aalberdi, A. (2024). *Evaluation and Development of MRI Techniques for the Quantification of Biologically Significant Boundaries in the Human Cerebral Cortex* (bachelor's dissertation). University of Mondragon.

Aguirre, G. K., Zarahn, E., & D'esposito, M. (1998). The variability of human, BOLD hemodynamic responses. *NeuroImage*, *8*(4), 360–369. https://doi.org/10.1006/nimg.1998.0369

Alahmadi, A. A. S. (2021). Effects of different smoothing on global and regional resting functional connectivity. *Neuroradiology*, *63*(1), 99–109. https://doi.org/10.1007/s00234-020-02523-8

Alarcon, N. (2019). Similarity in graphs: Jaccard versus the Overlap Coefficient. Retrieved July 18, 2024, from https://developer.nvidia.com/blog/similarity-in-graphs-jaccard-versus-the-overlap-coefficient/

Ardekani, B. A., & Kanno, I. (1998). Statistical methods for detecting activated regions in functional MRI of the brain. *Magnetic Resonance Imaging*, *16*(10), 1217–1225. https://doi.org/10.1016/S0730-725X(98)00125-8

Bach, P., Hill, H., Reinhard, I., Gädeke, T., Kiefer, F., & Leménager, T. (2022). Reliability of the fMRI-based assessment of self-evaluation in individuals with internet gaming disorder. *European Archives of Psychiatry and Clinical Neuroscience*, *272*(6), 1119–1134. https://doi.org/10.1007/s00406-021-01307-2

Bajada, C. J., Costa Campos, L. Q., Caspers, S., Muscat, R., Parker, G. J. M., Lambon Ralph, M. A., Cloutman, L. L., & Trujillo-Barreto, N. J. (2020). A tutorial and tool for exploring feature similarity gradients with MRI data. *NeuroImage*, *221*, 117140. https://doi.org/10.1016/j.neuroimage.2020.117140

Bandettini, P. A., Wong, E. C., Jesmanowicz, A., Hinks, R. S., & Hyde, J. S. (1994). Spin-echo and gradient-echo epi of human brain activation using bold contrast: A comparative study at 1.5 T. *NMR in Biomedicine*, *7*(1-2), 12–20. https://doi.org/10.1002/nbm.1940070104

Barth, M., Breuer, F., Koopmans, P. J., Norris, D. G., & Poser, B. A. (2016). Simultaneous multislice (SMS) imaging techniques. *Magnetic Resonance in Medicine*, *75*(1), 63–81. https://doi.org/10.1002/mrm.25897

Behzadi, Y., Restom, K., Liau, J., & Liu, T. T. (2007). A component based noise correction method (CompCor) for BOLD and perfusion based fMRI. *NeuroImage*, *37*(1), 90–101. https://doi.org/10.1016/j.neuroimage.2007.04.042

Belaroussi, B., Milles, J., Carme, S., Zhu, Y. M., & Benoit-Cattin, H. (2006). Intensity non-uniformity correction in MRI: Existing methods and their validation. *Medical Image Analysis*, *10*(2), 234–246. https://doi.org/10.1016/j.media.2005.09.004

Berman, A. J. L., Grissom, W. A., Witzel, T., Nasr, S., Park, D. J., Setsompop, K., & Polimeni, J. R. (2021). Ultra-high spatial resolution BOLD fMRI in humans using combined segmented-accelerated VFA-FLEET with a recursive RF pulse design. *Magnetic Resonance in Medicine*, *85*(1), 120–139. https://doi.org/10.1002/mrm.28415

Bernstein, M. A., King, K. F., & Zhou, X. J. (2004). *Handbook of MRI Pulse Sequences*. Elsevier.

Bishop, C. M. (2006). *Pattern recognition and machine learning*. Springer Science+Business Media, LLC.

Bisley, J. W., & Goldberg, M. E. (2010). Attention, Intention, and Priority in the Parietal Lobe. *Annual Review of Neuroscience*, *33*(Volume 33, 2010), 1–21. https://doi.org/10.1146/annurev-neuro-060909-152823

Blaimer, M., Breuer, F., Mueller, M., Heidemann, R. M., Griswold, M. A., & Jakob, P. M. (2004). SMASH, SENSE, PILS, GRAPPA: How to Choose the Optimal Method. *Topics in Magnetic Resonance Imaging*, *15*(4), 223. https://doi.org/10.1097/01.rmr.0000136558.09801.dd

Bodurka, J., Ye, F., Petridou, N., Murphy, K., & Bandettini, P. A. (2007). Mapping the MRI voxel volume in which thermal noise matches physiological noise—Implications for fMRI. *NeuroImage*, *34*(2), 542–549. https://doi.org/10.1016/j.neuroimage.2006.09.039

Boos, D. D., & Hughes-Oliver, J. M. (2000). How large does n have to be for Z and t intervals? *The American Statistician*, *54*(2), 121–128. https://doi.org/https://doi.org/10.1080/00031305.2000.10474524

Breuer, F. A., Blaimer, M., Heidemann, R. M., Mueller, M. F., Griswold, M. A., & Jakob, P. M. (2005). Controlled aliasing in parallel imaging results in higher acceleration (CAIPIRINHA) for multi-slice imaging. *Magnetic Resonance in Medicine*, *53*(3), 684–691. https://doi.org/10.1002/mrm.20401

Buccino, G., Binkofski, F., Fink, G. R., Fadiga, L., Fogassi, L., Gallese, V., Seitz, R. J., Zilles, K., Rizzolatti, G., & Freund, H.-J. (2001). Action observation activates premotor and parietal areas in a somatotopic manner: An fMRI study. *European Journal of Neuroscience*, *13*(2), 400–404. https://doi.org/10.1111/j.1460-9568.2001.01385.x

Buxton, R. B. (2009). *Introduction to Functional Magnetic Resonance Imaging: Principles and Techniques*. Cambridge University Press.

Calhoun, V. (2018). Data-driven approaches for identifying links between brain structure and function in health and disease. *Dialogues in Clinical Neuroscience*, *20*(2), 87–99. https://doi.org/10.31887/DCNS.2018.20.2/vcalhoun

Chen, J. (2019). Intro to Statistics for fMRI Analysis. https://gate.nmr.mgh.harvard.edu/wiki/whynhow/images/3/3c/20190321_Chen_IntroTofMRIstatistics.pdf

Chen, L., T. Vu, A., Xu, J., Moeller, S., Ugurbil, K., Yacoub, E., & Feinberg, D. A. (2015). Evaluation of highly accelerated simultaneous multi-slice EPI for fMRI. *NeuroImage*, *104*, 452–459. https://doi.org/10.1016/j.neuroimage.2014.10.027

Ciantar, K. G., Farrugia, C., Galdi, P., Scerri, K., Xu, T., & Bajada, C. J. (2022). Geometric effects of volume-to-surface mapping of fMRI data. *Brain Structure and Function*, *227*(7), 2457–2464. https://doi.org/10.1007/s00429-022-02536-4

Constable, R. T., & Spencer, D. D. (2001). Repetition time in echo planar functional MRI. *Magnetic Resonance in Medicine*, *46*(4), 748–755. https://doi.org/10.1002/mrm.1253

Currie, S., Hoggard, N., Craven, I. J., Hadjivassiliou, M., & Wilkinson, I. D. (2013). Understanding MRI: Basic MR physics for physicians. *Postgraduate Medical Journal*, *89*(1050), 209–223. https://doi.org/10.1136/postgradmedj-2012-131342

Dong, M., Qin, W., Zhao, L., Yang, X., Yuan, K., Zeng, F., Sun, J., Yu, D., von Deneen, K. M., Liang, F., & Tian, J. (2014). Expertise modulates local regional homogeneity of spontaneous brain activity in the resting brain: An fMRI study using the model of skilled acupuncturists. *Human Brain Mapping*, *35*(3), 1074–1084. https://doi.org/10.1002/hbm.22235

Du, Y. P., Chu, R., & Tregellas, J. R. (2014). Enhancing the Detection of BOLD Signal in fMRI by Reducing the Partial Volume Effect. *Computational and Mathematical Methods in Medicine*, *2014*, 1–9. https://doi.org/10.1155/2014/973972

EMITEL Consortium. (2016a). Blood oxygenation level dependent contrast (BOLD). Retrieved July 6, 2024, from https://www.emitel2.eu/emitwwwsql/encyclopedia.aspx

EMITEL Consortium. (2016b). Echo planar imaging. Retrieved July 6, 2024, from https://www.emitel2.eu/emitwwwsql/encyclopedia.aspx

EMITEL Consortium. (2016c). Functional Magnetic Resonance Imaging. Retrieved July 6, 2024, from https://www.emitel2.eu/emitwwwsql/encyclopedia.aspx

Ernst, R. R., & Anderson, W. A. (1966). Application of Fourier Transform Spectroscopy to Magnetic Resonance. *Review of Scientific Instruments*, *37*(1), 93–102. https://doi.org/10.1063/1.1719961

Esteban, O., Birman, D., Schaer, M., Koyejo, O. O., Poldrack, R. A., & Gorgolewski, K. J. (2017). MRIQC: Advancing the automatic prediction of image quality in MRI from unseen sites. *PLOS ONE*, *12*(9), e0184661. https://doi.org/10.1371/journal.pone.0184661

Esteban, O., Ciric, R., Finc, K., Blair, R. W., Markiewicz, C. J., Moodie, C. A., Kent, J. D., Goncalves, M., DuPre, E., Gomez, D. E. P., Ye, Z., Salo, T., Valabregue, R., Amlien, I. K., Liem, F., Jacoby, N., Stojić, H., Cieslak, M., Urchs, S., … Gorgolewski, K. J. (2020). Analysis of task-based functional MRI data preprocessed with fMRIPrep. *Nature protocols*, *15*(7), 2186–2202. https://doi.org/10.1038/s41596-020-0327-3

Esteban, O., Markiewicz, C. J., Blair, R. W., Moodie, C. A., Isik, A. I., Erramuzpe, A., Kent, J. D., Goncalves, M., DuPre, E., Snyder, M., Oya, H., Ghosh, S. S., Wright, J., Durnez, J., Poldrack, R. A., & Gorgolewski, K. J. (2019). fMRIPrep: A robust preprocessing pipeline for functional MRI. *Nature Methods*, *16*(1), 111–116. https://doi.org/10.1038/s41592-018-0235-4

Farrugia, C., Arenzana, I., Scerri, K., & Bajada, C. (2022). *The Vogt-Bailey index: A local gradient analysis*. https://doi.org/10.1101/2022.10.14.511925

Farrugia, C., Galdi, P., Irazu, I. A., Scerri, K., & Bajada, C. J. (2024). Local gradient analysis of human brain function using the Vogt-Bailey Index. *Brain Structure and Function*, *229*(2), 497–512. https://doi.org/10.1007/s00429-023-02751-7

Feinberg, D. A., Hale, J. D., Watts, J. C., Kaufman, L., & Mark, A. (1986). Halving MR imaging time by conjugation: Demonstration at 3.5 kG. *Radiology*, *161*(2), 527–531. https://doi.org/10.1148/radiology.161.2.3763926

Feinberg, D. A., & Setsompop, K. (2013). Ultra-fast MRI of the human brain with simultaneous multi-slice imaging. *Journal of Magnetic Resonance*, *229*, 90–100. https://doi.org/10.1016/j.jmr.2013.02.002

Fellner, C., Doenitz, C., Finkenzeller, T., Jung, E. M., Rennert, J., & Schlaier, J. (2009). Improving the spatial accuracy in functional magnetic resonance imaging (fMRI) based on the blood oxygenation level dependent (BOLD) effect: Benefits from parallel imaging and a 32-channel head array coil at 1.5 Tesla. *Clinical Hemorheology and Microcirculation*, *43*(1-2), 71–82. https://doi.org/10.3233/CH-2009-1222

Fiedler, M. (1973). Algebraic connectivity of graphs. *Czechoslovak Mathematical Journal*, *23*(2), 298–305. https://doi.org/10.21136/CMJ.1973.101168

Frahm, J., Merboldt, K.-D., & Hänicke, W. (1993). Functional MRI of human brain activation at high spatial resolution. *Magnetic Resonance in Medicine*, *29*(1), 139–144. https://doi.org/10.1002/mrm.1910290126

Friston, K. J., Holmes, A. P., Worsley, K. J., Poline, J.-P., Frith, C. D., & Frackowiak, R. S. J. (1994). Statistical parametric maps in functional imaging: A general linear approach. *Human Brain Mapping*, *2*(4), 189–210. https://doi.org/10.1002/hbm.460020402

Gao, J.-H., Miller, I., Lai, S., Xiong, J., & Fox, P. T. (1996). Quantitative assessment of blood inflow effects in functional MRI signals. *Magnetic Resonance in Medicine*, *36*(2), 314–319. https://doi.org/10.1002/mrm.1910360219

GE Healthcare. (2005). MR Field Notes. https://mri-q.com/uploads/3/4/5/7/34572113/ge_fieldnotes_volume1-2_coils.pdf

Gilford, C. ((2024). *Localisation of brain activity for SSVEP-based BCIs : An fMRI and EEG study* (Master's thesis). University of Malta. Retrieved April 27, 2024, from https://www.um.edu.mt/library/oar/handle/123456789/118856

Glover, G. H., Lemieux, S. K., Drangova, M., & Pauly, J. M. (1996). Decomposition of inflow and blood oxygen level-dependent (BOLD) effects with dual-echo spiral gradient-recalled echo (GRE) fMRI. *Magnetic Resonance in Medicine*, *35*(3), 299–308. https://doi.org/10.1002/mrm.1910350306

Goebel, R. (2014). Temporal High-Pass Filtering. Retrieved June 30, 2024, from https://www.brainvoyager.com/bvqx/doc/UsersGuide/Preprocessing/TemporalHighPassFiltering.html

Gonzalez-Castillo, J., Roopchansingh, V., Bandettini, P. A., & Bodurka, J. (2011). Physiological noise effects on the flip angle selection in BOLD fMRI. *NeuroImage*, *54*(4), 2764–2778. https://doi.org/10.1016/j.neuroimage.2010.11.020

Gorgolewski, K. J., Auer, T., Calhoun, V. D., Craddock, R. C., Das, S., Duff, E. P., Flandin, G., Ghosh, S. S., Glatard, T., Halchenko, Y. O., Handwerker, D. A., Hanke, M., Keator, D., Li, X., Michael, Z., Maumet, C., Nichols, B. N., Nichols, T. E., Pellman, J., … Poldrack, R. A. (2016). The brain imaging data structure, a format for organizing and describing outputs of neuroimaging experiments. *Scientific Data*, *3*(1), 160044. https://doi.org/10.1038/sdata.2016.44

Gorno-Tempini, M. L., Hutton, C., Josephs, O., Deichmann, R., Price, C., & Turner, R. (2002). Echo Time Dependence of BOLD Contrast and Susceptibility Artifacts. *NeuroImage*, *15*(1), 136–142. https://doi.org/10.1006/nimg.2001.0967

Gossuin, Y., Hocq, A., Gillis, P., & Lam, V. Q. (2010). Physics of magnetic resonance imaging: From spin to pixel. *Journal of Physics D: Applied Physics*, *43*(21), 213001. https://doi.org/10.1088/0022-3727/43/21/213001

Gountouna, V.-E., Job, D. E., McIntosh, A. M., Moorhead, T. W. J., Lymer, G. K. L., Whalley, H. C., Hall, J., Waiter, G. D., Brennan, D., McGonigle, D. J., Ahearn, T. S., Cavanagh, J., Condon, B., Hadley, D. M., Marshall, I., Murray, A. D., Steele, J. D., Wardlaw, J. M., & Lawrie, S. M. (2010). Functional Magnetic Resonance Imaging (fMRI) reproducibility and variance components across visits and scanning sites with a finger tapping task. *NeuroImage*, *49*(1), 552–560. https://doi.org/10.1016/j.neuroimage.2009.07.026

Graessner, J. (2013). Bandwidth in MRI. *MAGNETOM Flash*. https://mriquestions.com/uploads/3/4/5/7/34572113/bandwidth_in_mri_siemens_.pdf

Greenacre, M., Groenen, P. J. F., Hastie, T., D'Enza, A. I., Markos, A., & Tuzhilina, E. (2022). Principal component analysis. *Nature Reviews Methods Primers*, *2*(1), 1–21. https://doi.org/10.1038/s43586-022-00184-w

Griswold, M. A., Jakob, P. M., Heidemann, R. M., Nittka, M., Jellus, V., Wang, J., Kiefer, B., & Haase, A. (2002). Generalized autocalibrating partially parallel acquisitions (GRAPPA). *Magnetic Resonance in Medicine*, *47*(6), 1202–1210. https://doi.org/10.1002/mrm.10171

Handwerker, D. A., Ollinger, J. M., & D'Esposito, M. (2004). Variation of BOLD hemodynamic responses across subjects and brain regions and their effects on statistical analyses. *NeuroImage*, *21*(4), 1639–1651. https://doi.org/10.1016/j.neuroimage.2003.11.029

Harri, M., Mika, T., Jussi, H., Nevalainen, O. S., & Jarmo, H. (2007). Evaluation of partial volume effect correction methods for brain positron emission tomography: Quantification and reproducibility. *Journal of Medical Physics / Association of Medical Physicists of India*, *32*(3), 108–117. https://doi.org/10.4103/0971-6203.35723

Henri-Bhargava, A., Stuss, D. T., & Freedman, M. (2018). Clinical Assessment of Prefrontal Lobe Functions. *CONTINUUM: Lifelong Learning in Neurology*, *24*(3), 704. https://doi.org/10.1212/CON.0000000000000609

Holdsworth, S. J., & Bammer, R. (2008). Magnetic Resonance Imaging Techniques: fMRI, DWI, and PWI. *Seminars in Neurology*, *28*(4), 395–406. https://doi.org/10.1055/s-0028-1083697

Hoogenraad, F. G. C., Pouwels, P. J. W., Hofman, M. B. M., Rombouts, S. A. R. B., Lavini, C., Leach, M. O., & Haacke, E. M. (2000). High-resolution segmented EPI in a motor task fMRI study. *Magnetic Resonance Imaging*, *18*(4), 405–409. https://doi.org/10.1016/S0730-725X(00)00127-2

Hoogenraad, F. G., Hofman, M. B., Pouwels, P. J., Reichenbach, J. R., Rombouts, S. A., & Haacke, E. M. (1999). Sub-millimeter fMRI at 1.5 tesla: Correlation of high resolution with low resolution measurements. *Journal of Magnetic Resonance Imaging*, *9*(3), 475–482. https://doi.org/10.1002/(SICI)1522-2586(199903)9:3<475::AID-JMRI17>3.0.CO;2-Y

Howseman, A. M., Grootoonk, S., Porter, D. A., Ramdeen, J., Holmes, A. P., & Turner, R. (1999). The Effect of Slice Order and Thickness on fMRI Activation Data Using Multislice Echo-Planar Imaging. *NeuroImage*, *9*(4), 363–376. https://doi.org/10.1006/nimg.1998.0418

Hu, Y., & Glover, G. H. (2009). Increasing spatial coverage for high-resolution functional MRI. *Magnetic Resonance in Medicine*, *61*(3), 716–722. https://doi.org/10.1002/mrm.21898

Huettel, S. A., Song, A. W., McCarthy, G., Huettel, S. A., Song, A. W., & McCarthy, G. (2014). *Functional Magnetic Resonance Imaging* (Third Edition). Oxford University Press.

Hutton, C., Bork, A., Josephs, O., Deichmann, R., Ashburner, J., & Turner, R. (2002). Image Distortion Correction in fMRI: A Quantitative Evaluation. *NeuroImage*, *16*(1), 217–240. https://doi.org/10.1006/nimg.2001.1054

Hyde, J. S., Biswal, B. B., & Jesmanowicz, A. (2001). High-resolution fMRI using multislice partial k-space GR-EPI with cubic voxels. *Magnetic Resonance in Medicine*, *46*(1), 114–125. https://doi.org/10.1002/mrm.1166

Jahanian, H., Holdsworth, S., Christen, T., Wu, H., Zhu, K., Kerr, A. B., Middione, M. J., Dougherty, R. F., Moseley, M., & Zaharchuk, G. (2019). Advantages of short repetition time resting-state functional MRI enabled by simultaneous multi-slice imaging. *Journal of Neuroscience Methods*, *311*, 122–132. https://doi.org/10.1016/j.jneumeth.2018.09.033

Jahn, A. (2019). Chapter 5: Smoothing — Andy's Brain Book 1.0 documentation. Retrieved July 12, 2024, from https://andysbrainbook.readthedocs.io/en/stable/fMRI_Short_Course/Preprocessing/Smoothing.html

Jenkinson, M., Bijsterbosch, J., Chappell, M., & Winkler, A. (2020). *Short introduction to the General Linear Model for Neuroimaging*. Oxford University Press.

Jenkinson, M., Chappell, M., Jenkinson, M., & Chappell, M. (2017). *Introduction to Neuroimaging Analysis*. Oxford University Press.

Jenkinson, M. (2018). *Introduction to neuroimaging analysis*. Oxford University Press.

Jesmanowicz, A., Bandettini, P. A., & Hyde, J. S. (1998). Single-shot half k-space high-resolution gradient-recalled EPI for fMRI at 3 tesla. *Magnetic Resonance in Medicine*, *40*(5), 754–762. https://doi.org/10.1002/mrm.1910400517

Jezzard, P., & Clare, S. (1999). Sources of distortion in functional MRI data. *Human Brain Mapping*, *8*(2-3), 80–85. https://doi.org/10.1002/(SICI)1097-0193(1999)8:2/3<80::AID-HBM2>3.0.CO;2-C

Jia, X.-Z., Sun, J.-W., Ji, G.-J., Liao, W., Lv, Y.-T., Wang, J., Wang, Z., Zhang, H., Liu, D.-Q., & Zang, Y.-F. (2020). Percent amplitude of fluctuation: A simple measure for resting-state fMRI signal at single voxel level. *PLOS ONE*, *15*(1), e0227021. https://doi.org/10.1371/journal.pone.0227021

Khushu, S., Kumaran, S. S., Tripathi, R. P., Gupta, A., Jain, P. C., & Jain, V. (2001). Functional magnetic resonance imaging of the primary motor cortex in humans: Response to increased functional demands. *Journal of Biosciences*, *26*(2), 205–215. https://doi.org/10.1007/BF02703644

Kliemann, D., Adolphs, R., Armstrong, T., Galdi, P., Kahn, D. A., Rusch, T., Enkavi, A. Z., Liang, D., Lograsso, S., Zhu, W., Yu, R., Nair, R., Paul, L. K., & Tyszka, J. M. (2022). Caltech Conte Center, a multimodal data resource for exploring social cognition and decision-making. *Scientific Data*, *9*(1), 138. https://doi.org/10.1038/s41597-022-01171-2

Krüger, G., Kastrup, A., & Glover, G. H. (2001). Neuroimaging at 1.5 T and 3.0 T: Comparison of oxygenation-sensitive magnetic resonance imaging. *Magnetic Resonance in Medicine*, *45*(4), 595–604. https://doi.org/10.1002/mrm.1081

Larkman, D. J., Hajnal, J. V., Herlihy, A. H., Coutts, G. A., Young, I. R., & Ehnholm, G. (2001). Use of multicoil arrays for separation of signal from multiple slices simultaneously excited. *Journal of Magnetic Resonance Imaging*, *13*(2), 313–317. https://doi.org/10.1002/1522-2586(200102)13:2<313::AID-JMRI1045>3.0.CO;2-W

Larkman, D. J., & Nunes, R. G. (2007). Parallel magnetic resonance imaging. *Physics in Medicine & Biology*, *52*(7), R15. https://doi.org/10.1088/0031-9155/52/7/R01

Leibovici, D. G., & Smith, S. (2001). Comparing groups of subjects in fMRI studies: A review of the GLM approach.

Leys, C., Ley, C., Klein, O., Bernard, P., & Licata, L. (2013). Detecting outliers: Do not use standard deviation around the mean, use absolute deviation around the median. *Journal of Experimental Social Psychology*, *49*(4), 764–766. https://doi.org/10.1016/j.jesp.2013.03.013

Liu, D., Yan, C., Ren, J., Yao, L., Kiviniemi, V. J., & Zang, Y. (2010). Using coherence to measure regional homogeneity of resting-state fMRI signal. *Frontiers in Systems Neuroscience*, *4*. https://doi.org/10.3389/fnsys.2010.00024

Lotze, M., Erb, M., Flor, H., Huelsmann, E., Godde, B., & Grodd, W. (2000). fMRI Evaluation of Somatotopic Representation in Human Primary Motor Cortex. *NeuroImage*, *11*(5), 473–481. https://doi.org/10.1006/nimg.2000.0556

Maus, B., van Breukelen, G. J. P., Goebel, R., & Berger, M. P. F. (2010). Optimization of Blocked Designs in fMRI Studies. *Psychometrika*, *75*(2), 373–390. https://doi.org/10.1007/s11336-010-9159-3

McDowell, A. R., & Carmichael, D. W. (2019). Optimal repetition time reduction for single subject event-related functional magnetic resonance imaging. *Magnetic Resonance in Medicine*, *81*(3), 1890–1897. https://doi.org/10.1002/mrm.27498

McRobbie, D. W., Moore, E. A., Graves, M. J., & Prince, M. R. (2006). *MRI from Picture to Proton* (2nd ed.). Cambridge University Press. https://doi.org/10.1017/CBO9780511545405

Menon, R. S., Ogawa, S., Tank, D. W., & Uğurbil, K. (1993). 4 Tesla gradient recalled echo characteristics of photic stimulation-induced signal changes in the human primary visual cortex. *Magnetic Resonance in Medicine*, *30*(3), 380–386. https://doi.org/10.1002/mrm.1910300317

Miezin, F. M., Maccotta, L., Ollinger, J. M., Petersen, S. E., & Buckner, R. L. (2000). Characterizing the Hemodynamic Response: Effects of Presentation Rate, Sampling Procedure, and the Possibility of Ordering Brain Activity Based on Relative Timing. *NeuroImage*, *11*(6), 735–759. https://doi.org/10.1006/nimg.2000.0568

Mintzopoulos, D., G. Astrakas, L., Hiroki, M., Khanicheh, A., L. Wald, L., R. Rosen, B., & Aria Tzika, A. (2009). fMRI Using GRAPPA EPI with High Spatial Resolution Improves BOLD Signal Detection at 3T. *The Open Magnetic Resonance Journal*, *2*(1). Retrieved March 18, 2024, from https://benthamopen.com/ABSTRACT/TOMRJ-2-57

Molloy, E. K., Meyerand, M. E., & Birn, R. M. (2014). The influence of spatial resolution and smoothing on the detectability of resting-state and task fMRI. *NeuroImage*, *86*, 221–230. https://doi.org/10.1016/j.neuroimage.2013.09.001

Monti, M. M. (2011). Statistical Analysis of fMRI Time-Series: A Critical Review of the GLM Approach. *Frontiers in Human Neuroscience*, *5*. https://doi.org/10.3389/fnhum.2011.00028

Morante, M., Kopsinis, Y., Chatzichristos, C., Protopapas, A., & Theodoridis, S. (2021). Enhanced design matrix for task-related fMRI data analysis. *NeuroImage*, *245*, 118719. https://doi.org/10.1016/j.neuroimage.2021.118719

Murphy, K., Bodurka, J., & Bandettini, P. A. (2007). How long to scan? The relationship between fMRI temporal signal to noise ratio and necessary scan duration. *NeuroImage*, *34*(2), 565–574. https://doi.org/10.1016/j.neuroimage.2006.09.032

Norris, D. G. (2012). Spin-echo fMRI: The poor relation? *NeuroImage*, *62*(2), 1109–1115. https://doi.org/10.1016/j.neuroimage.2012.01.003

Parkes, L., Fulcher, B., Yücel, M., & Fornito, A. (2018). An evaluation of the efficacy, reliability, and sensitivity of motion correction strategies for resting-state functional MRI. *NeuroImage*, *171*, 415–436. https://doi.org/10.1016/j.neuroimage.2017.12.073

Peirce, J., Gray, J. R., Simpson, S., MacAskill, M., Höchenberger, R., Sogo, H., Kastman, E., & Lindeløv, J. K. (2019). PsychoPy2: Experiments in behavior made easy. *Behavior Research Methods*, *51*(1), 195–203. https://doi.org/10.3758/s13428-018-01193-y

Pimentel, M. A. F., Vilela, P., Sousa, I., & Figueiredo, P. (2011). Localization of the hand motor area by arterial spin labeling and blood oxygen level-dependent functional magnetic resonance imaging. *Human Brain Mapping*, *34*(1), 96–108. https://doi.org/10.1002/hbm.21418

Plewes, D. B., & Kucharczyk, W. (2012). Physics of MRI: A primer. *Journal of Magnetic Resonance Imaging*, *35*(5), 1038–1054. https://doi.org/10.1002/jmri.23642

Poldrack, R. A., Mumford, J., A, & Nichols, T., E. (2011). *Handbook of Functional MRI Data Analysis*. Cambridge University Press.

Poline, J.-B., & Brett, M. (2012). The general linear model and fMRI: Does love last forever? *NeuroImage*, *62*(2), 871–880. https://doi.org/10.1016/j.neuroimage.2012.01.133

Poustchi-Amin, M., Mirowitz, S. A., Brown, J. J., McKinstry, R. C., & Li, T. (2001). Principles and Applications of Echo-planar Imaging: A Review for the General Radiologist. *RadioGraphics*, *21*(3), 767–779. https://doi.org/10.1148/radiographics.21.3.g01ma23767

Power, J. D., Barnes, K. A., Snyder, A. Z., Schlaggar, B. L., & Petersen, S. E. (2012). Spurious but systematic correlations in functional connectivity MRI networks arise from subject motion. *NeuroImage*, *59*(3), 2142–2154. https://doi.org/10.1016/j.neuroimage.2011.10.018

Preibisch, C., Wallenhorst, T., Heidemann, R., Zanella, F. E., & Lanfermann, H. (2008). Comparison of parallel acquisition techniques generalized autocalibrating partially parallel acquisitions (GRAPPA) and modified sensitivity encoding (mSENSE) in functional MRI (fMRI) at 3T. *Journal of Magnetic Resonance Imaging*, *27*(3), 590–598. https://doi.org/10.1002/jmri.21191

Pruessmann, K. P., Weiger, M., Scheidegger, M. B., & Boesiger, P. (1999). SENSE: Sensitivity encoding for fast MRI. *Magnetic Resonance in Medicine*, *42*(5), 952–962. https://doi.org/10.1002/(SICI)1522-2594(199911)42:5<952::AID-MRM16>3.0.CO;2-S

Queensland-Government. (2022). Brain Map: Occipital Lobes. Retrieved July 27, 2024, from https://www.health.qld.gov.au/abios/asp/boccipital

Rangaprakash, D., Wu, G.-R., Marinazzo, D., Hu, X., & Deshpande, G. (2018). Hemodynamic response function (HRF) variability confounds resting-state fMRI functional connectivity. *Magnetic Resonance in Medicine*, *80*(4), 1697–1713. https://doi.org/10.1002/mrm.27146

Rastegarnia, S., St-Laurent, M., DuPre, E., Pinsard, B., & Bellec, P. (2023). Brain decoding of the Human Connectome Project tasks in a dense individual fMRI dataset. *NeuroImage*, *283*, 120395. https://doi.org/10.1016/j.neuroimage.2023.120395

Risk, B. B., Murden, R. J., Wu, J., Nebel, M. B., Venkataraman, A., Zhang, Z., & Qiu, D. (2021). Which multiband factor should you choose for your resting-state fMRI study? *NeuroImage*, *234*, 117965. https://doi.org/10.1016/j.neuroimage.2021.117965

Satterthwaite, T. D., Elliott, M. A., Gerraty, R. T., Ruparel, K., Loughead, J., Calkins, M. E., Eickhoff, S. B., Hakonarson, H., Gur, R. C., Gur, R. E., & Wolf, D. H. (2013). An improved framework for confound regression and filtering for control of motion artifact in the preprocessing of resting-state functional connectivity data. *NeuroImage*, *64*, 240–256. https://doi.org/10.1016/j.neuroimage.2012.08.052

Schmitt, F., Stehling, M. K., & Turner, R. (2012). *Echo-Planar Imaging: Theory, Technique and Application*. Springer Science & Business Media.

Setsompop, K., Gagoski, B. A., Polimeni, J. R., Witzel, T., Wedeen, V. J., & Wald, L. L. (2012). Blipped-controlled aliasing in parallel imaging for simultaneous multislice echo planar imaging with reduced g-factor penalty. *Magnetic Resonance in Medicine*, *67*(5), 1210–1224. https://doi.org/10.1002/mrm.23097

Shukla, D. K., Keehn, B., & Müller, R. A. (2010). Regional homogeneity of fMRI time series in autism spectrum disorders. *Neuroscience Letters*, *476*(1), 46–51. https://doi.org/10.1016/j.neulet.2010.03.080

Singh, M., Sungkarat, W., Jeong, J.-W., & Zhou, Y. (2002). Extraction of temporal information in functional MRI. *IEEE Transactions on Nuclear Science*, *49*(5), 2284–2290. https://doi.org/10.1109/TNS.2002.803774

Sommer, M. A. (2003). The role of the thalamus in motor control. *Current Opinion in Neurobiology*, *13*(6), 663–670. https://doi.org/10.1016/j.conb.2003.10.014

Stroman, P. W. (2016). *Essentials of Functional MRI*. CRC Press.

Tian, L., Ren, J., & Zang, Y. (2012). Regional homogeneity of resting state fMRI signals predicts Stop signal task performance. *NeuroImage*, *60*(1), 539–544. https://doi.org/10.1016/j.neuroimage.2011.11.098

Triantafyllou, C., Hoge, R. D., Krueger, G., Wiggins, C. J., Potthast, A., Wiggins, G. C., & Wald, L. L. (2005). Comparison of physiological noise at 1.5 T, 3 T and 7 T and optimization of fMRI acquisition parameters. *NeuroImage*, *26*(1), 243–250. https://doi.org/10.1016/j.neuroimage.2005.01.007

Turesky, T. K., Olulade, O. A., Luetje, M. M., & Eden, G. F. (2018). An fMRI study of finger tapping in children and adults. *Human Brain Mapping*, *39*(8), 3203–3215. https://doi.org/10.1002/hbm.24070

Turner, B. O., Paul, E. J., Miller, M. B., & Barbey, A. K. (2018). Small sample sizes reduce the replicability of task-based fMRI studies. *Communications Biology*, *1*(1), 1–10. https://doi.org/10.1038/s42003-018-0073-z

Tustison, N. J., Avants, B. B., Cook, P. A., Zheng, Y., Egan, A., Yushkevich, P. A., & Gee, J. C. (2010). N4ITK: Improved N3 Bias Correction. *IEEE Transactions on Medical Imaging*, *29*(6), 1310–1320. https://doi.org/10.1109/TMI.2010.2046908

Tyszka, M. (2024). Jmtyszka/bidskit. Retrieved April 21, 2024, from https://github.com/jmtyszka/bidskit

Uğurbil, K., Xu, J., Auerbach, E. J., Moeller, S., Vu, A. T., Duarte-Carvajalino, J. M., Lenglet, C., Wu, X., Schmitter, S., Van de Moortele, P. F., Strupp, J., Sapiro, G., De Martino, F., Wang, D., Harel, N., Garwood, M., Chen, L., Feinberg, D. A., Smith, S. M., … Yacoub, E. (2013). Pushing spatial and temporal resolution for functional and diffusion MRI in the Human Connectome Project. *NeuroImage*, *80*, 80–104. https://doi.org/10.1016/j.neuroimage.2013.05.012

van der Zwaag, W., Francis, S., Head, K., Peters, A., Gowland, P., Morris, P., & Bowtell, R. (2009). fMRI at 1.5, 3 and 7 T: Characterising BOLD signal changes. *NeuroImage*, *47*(4), 1425–1434. https://doi.org/10.1016/j.neuroimage.2009.05.015

Volz, S., Callaghan, M. F., Josephs, O., & Weiskopf, N. (2019). Maximising BOLD sensitivity through automated EPI protocol optimisation. *NeuroImage*, *189*, 159–170. https://doi.org/10.1016/j.neuroimage.2018.12.052

von Luxburg, U. (2007). A tutorial on spectral clustering. *Statistics and Computing*, *17*(4), 395–416. https://doi.org/10.1007/s11222-007-9033-z

Wall, M. B. (2023). Multiband acquisition sequences for fMRI: Proceed with caution. *Aperture Neuro*, *3*. https://doi.org/10.52294/001c.91292

Wansapura, J. P., Holland, S. K., Dunn, R. S., & Ball Jr., W. S. (1999). NMR relaxation times in the human brain at 3.0 tesla. *Journal of Magnetic Resonance Imaging*, *9*(4), 531–538. https://doi.org/10.1002/(SICI)1522-2586(199904)9:4<531::AID-JMRI4>3.0.CO;2-L

Weibull, A., Gustavsson, H., Mattsson, S., & Svensson, J. (2008). Investigation of spatial resolution, partial volume effects and smoothing in functional MRI using artificial 3D time series. *NeuroImage*, *41*(2), 346–353. https://doi.org/10.1016/j.neuroimage.2008.02.015

Welvaert, M., & Rosseel, Y. (2013). On the Definition of Signal-To-Noise Ratio and Contrast-To-Noise Ratio for fMRI Data. *PLOS ONE*, *8*(11), e77089. https://doi.org/10.1371/journal.pone.0077089

Wilson, S. M., Bautista, A., Yen, M., Lauderdale, S., & Eriksson, D. K. (2017). Validity and reliability of four language mapping paradigms. *NeuroImage: Clinical*, *16*, 399–408. https://doi.org/10.1016/j.nicl.2016.03.015

Witt, S. T., Laird, A. R., & Meyerand, M. E. (2008). Functional neuroimaging correlates of finger-tapping task variations: An ALE meta-analysis. *NeuroImage*, *42*(1), 343–356. https://doi.org/10.1016/j.neuroimage.2008.04.025

Wu, T., Long, X., Zang, Y., Wang, L., Hallett, M., Li, K., & Chan, P. (2009). Regional homogeneity changes in patients with Parkinson’s disease. *Human Brain Mapping*, *30*(5), 1502–1510. https://doi.org/10.1002/hbm.20622

Wüthrich, F., Lefebvre, S., Nadesalingam, N., Bernard, J. A., Mittal, V. A., Shankman, S. A., & Walther, S. (2023). Test–retest reliability of a finger-tapping fMRI task in a healthy population. *European Journal of Neuroscience*, *57*(1), 78–90. https://doi.org/10.1111/ejn.15865

Xu, Z., Lai, J., Zhang, H., Ng, C. H., Zhang, P., Xu, D., & Hu, S. (2019). Regional homogeneity and functional connectivity analysis of resting-state magnetic resonance in patients with bipolar II disorder. *Medicine*, *98*(47), e17962. https://doi.org/10.1097/MD.0000000000017962

Yuan, L.-X., Zhao, N., Wang, X.-Q., Lv, Y.-T., & He, H. (2021). Echo Time Dependency of Local Activity Metrics of Resting-State Functional MRI. *Frontiers in Neuroscience*, *15*. https://doi.org/10.3389/fnins.2021.619412

Yuan, R., Di, X., Kim, E. H., Barik, S., Rypma, B., & Biswal, B. B. (2013). Regional homogeneity of resting-state fMRI contributes to both neurovascular and task activation variations. *Magnetic Resonance Imaging*, *31*(9), 1492–1500. https://doi.org/10.1016/j.mri.2013.07.005

Yun, S. D., & Shah, N. J. (2017). Whole-brain high in-plane resolution fMRI using accelerated EPIK for enhanced characterisation of functional areas at 3T. *PLOS ONE*, *12*(9), e0184759. https://doi.org/10.1371/journal.pone.0184759

Zang, Y., Jiang, T., Lu, Y., He, Y., & Tian, L. (2004). Regional homogeneity approach to fMRI data analysis. *NeuroImage*, *22*(1), 394–400. https://doi.org/10.1016/j.neuroimage.2003.12.030

Zhang, Y., Hu, Q., Liang, J., Hu, Z., Qian, T., Li, K., Zhao, X., & Liang, P. (2023). Shorter TR combined with finer atlas positively modulate topological organization of brain network: A resting state fMRI study. *Network: Computation in Neural Systems*, *34*(3), 174–189. https://doi.org/10.1080/0954898X.2023.2215860

Zou, P., Hutchins, S. B., Dutkiewicz, R. M., Li, C.-S., & Ogg, R. J. (2005). Effects of EPI readout bandwidth on measured activation map and BOLD response in fMRI experiments. *NeuroImage*, *27*(1), 15–25. https://doi.org/10.1016/j.neuroimage.2005.01.004

A Ethics Approval

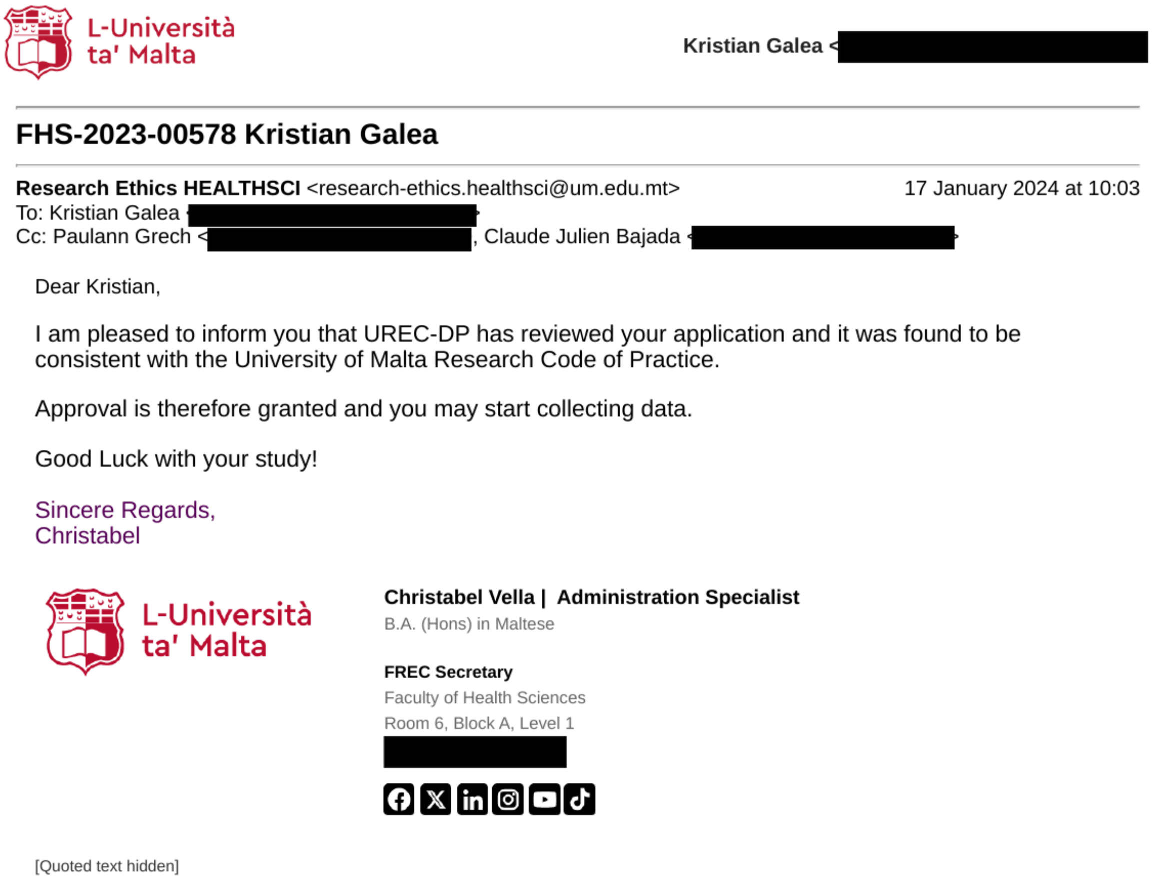

Kristian Galea <[redacted]

FHS-2023-00578 Kristian Galea

Research Ethics HEALTHSCI <research-ethics.healthsci@um.edu.mt> 17 January 2024 at 10:03
To: Kristian Galea [redacted]
Cc: Paulann Grech <[redacted], Claude Julien Bajada [redacted]

Dear Kristian,

I am pleased to inform you that UREC-DP has reviewed your application and it was found to be consistent with the University of Malta Research Code of Practice.

Approval is therefore granted and you may start collecting data.

Good Luck with your study!

Sincere Regards,
Christabel

Christabel Vella | Administration Specialist
B.A. (Hons) in Maltese

FREC Secretary
Faculty of Health Sciences
Room 6, Block A, Level 1
[redacted]

[Quoted text hidden]

Figure A1. Email of acceptance from the University Research Ethics Committee of the University of Malta